

# THE EQUILIBRIUM STRUCTURE OF DARK MATTER HALOS

by

Michael Travis Busha

A dissertation submitted in partial fulfillment  
of the requirements for the degree of  
Doctor of Philosophy  
(Physics)  
in the University of Michigan  
2007

Doctoral Committee:

Professor August E. Evrard, Co-Chair  
Professor Fred C. Adams, Co-Chair  
Professor Anthony M. Block  
Professor Timothy A. McKay  
Assistant Professor Leopoldo A. Pando Zayas

Copyright © Michael Travis Busha 2007  
All Rights Reserved

This dissertation is dedicated to my mother. Without her support and teachings I wouldn't be here.

## ACKNOWLEDGMENTS

I had lots of help completing this dissertation and making my graduate school career successful. First and foremost, I must thank my advisors, Gus Evrard and Fred Adams. Not many graduate students are lucky enough to have advisors as supportive and helpful as Gus and Fred. I also need to thank Risa Wechsler for helping me get started in this field. Additionally, I would like to thank my friends and family, in particular Elizabeth, my parents, and The Cronies, for supporting me all this time. Finally, I need to thank Kimberly Smith for making sure that everything in the department ran smoothly while I was here.

Monetary support for my research was partially provided by NASA, the Foundational Institute, a Regent's Fellowship from the University of Michigan, and a Rackham Predoctoral Fellowship.

# CONTENTS

DEDICATION . . . . .	ii
ACKNOWLEDGMENTS . . . . .	iii
LIST OF FIGURES . . . . .	vii
LIST OF TABLES . . . . .	xii
LIST OF APPENDICES . . . . .	xiii

## CHAPTER

1 Introduction . . . . .	1
2 The Standard Model of Cosmology . . . . .	3
2.1 The Homogeneous Universe . . . . .	4
2.2 The Lumpy Universe . . . . .	10
2.3 The Dark Universe . . . . .	14
2.3.1 Dark Matter . . . . .	15
2.3.2 Dark Energy . . . . .	18
2.3.3 Inflation . . . . .	19
2.4 Large Scale Structure . . . . .	20
2.4.1 Halo Formation . . . . .	21
2.4.2 CDM Halos . . . . .	23
2.5 Cosmological Parameters . . . . .	26
3 Cosmological N-body Simulations . . . . .	28
3.1 N-body Techniques and Algorithms . . . . .	33
3.1.1 Force Softening . . . . .	33

3.1.2	Time Integration . . . . .	35
3.1.3	The Tree Method . . . . .	36
3.1.4	The PM and TreePM methods . . . . .	39
3.2	Parallelization . . . . .	40
3.3	Generating Initial Conditions . . . . .	41
3.4	Finding Dark Matter Halos . . . . .	43
3.4.1	Subhalos . . . . .	45
4	Asymptotic Halo Structure . . . . .	48
4.1	Analytic Descriptions Of Structure Formation . . . . .	50
4.1.1	Collapse of overdense regions . . . . .	50
4.1.2	Criterion for being bound to existing structures . . . . .	51
4.2	Numerical Simulations Of Structure Formation . . . . .	54
4.2.1	Halo Phase-space Structure . . . . .	60
4.2.2	Halo Density Profile . . . . .	61
4.3	Long-Term Ramifications Of Cosmic Acceleration . . . . .	64
4.3.1	Isolation of bound structures . . . . .	64
4.3.2	Asymptotic structure of space-time . . . . .	66
4.3.3	Background radiation fields in an accelerating universe . . . . .	68
4.3.4	Particle annihilation in an accelerating universe . . . . .	69
4.4	Discussion And Conclusions . . . . .	70
5	The Asymptotic Structure of Space-Time . . . . .	74
5.1	Generic Form for the Density Profile. . . . .	75
5.2	Asymptotic Form for the Metric . . . . .	77
5.3	Summary . . . . .	80
6	Asymptotic Halo Mass . . . . .	82
6.1	Simulations and Mass Measures . . . . .	83
6.2	Results . . . . .	85

6.3	Summary	94
7	Small Scale Power and Accretion History	96
7.1	Simulations	99
7.2	Comparisons Of The Dark Matter Distribution	106
7.2.1	Evolution of the Power Spectrum	106
7.2.2	Mass Function	109
7.2.3	Halo Correspondence	111
7.2.4	Sub-Truncation Scale Halos In WDM	112
7.3	Comparison Of Halo Properties	115
7.3.1	Mass Accretion Histories	115
7.3.2	Halo Substructure	124
7.3.3	Density Profile	129
7.4	Conclusions	134
8	Conclusions	137
APPENDICES		145

# LIST OF FIGURES

Figure

2.1	The evolution of the scale factor, $a$ , for universes with various components. . . . .	9
3.1	The dark matter density field from the Millennium Simulation, a $10^{10}$ particle N-Body simulation, the largest to date. <i>Image Credit:</i> Springel et al. (2005) . . . . .	31
3.2	The dark matter distribution around a Milky Way-sized halo with $M_{200} = 1.8 \times 10^{12} M_{\odot}$ and over 10,000 identified subhalos. The image size is $800 \times 600 h^{-1} \text{kpc}$ . <i>Image Credit:</i> Diemand et al. (2007). . . . .	32
3.3	<i>Top Panel:</i> The decomposition of a 2-dimensional domain into squares for the construction of a force tree. <i>Bottom Panel:</i> How the tree in the top panel is split during parallelization. The left shows the space filling Peano-Hilbert curve with the o's along the curve representing the locations where the curve is cut for decomposition purposes. The boxes on the right show the tree information stored on two specific processors. <i>Image Credit:</i> Springel (2005). . . . .	38
3.4	Examples of Peano-Hilbert curves of various degrees in two and three dimensions. <i>Image Credit:</i> Springel (2005) . . . . .	42
4.1	Evolution of structure in a $\Lambda$ -dominated universe. . . . .	57
4.2	Gravitational sphere of influence of a cosmological object as a function of the mass enclosed within the sphere of influence at $a=1$ . . . . .	58



4.3	Radial velocity relative to the cluster center as a function of distance for particles in the largest halo at the epochs indicated. . . . .	59
4.4	The asymptotic form for the density distribution of dark matter halos.	63
5.1	The dimensionless functions $\alpha(\xi)$ and $\beta(\xi)$ appearing in the asymptotic form of the space-time metric of equation 5.8 . . . . .	79
6.1	The distribution of dark matter radial velocities as a function of dis- tance from the halo center. . . . .	87
6.2	Comparison of mass and radial scales for the progenitors of the 400 most massive halos identified at the end of the computation. . . . .	90
6.3	The asymptotic form of the density distribution for dark matter halos.	93
7.1	The input power spectra for the $\Lambda$ CDM(solid line) and WDM (dashed line) simulations. . . . .	101
7.2	The density fields of comoving slices of the cosmic web at $a = 0.3, 1, 3,$ and 100 (columns, left to right) of a $\Lambda$ CDM(top) and WDM (bottom) cosmologies from our small volume simulations. . . . .	103
7.3	The density field around a large halo at $a = 0.3, 1, 3,$ and 100 (columns, left to right) from our small volume simulations. . . . .	104
7.4	<i>Left:</i> Rare ( $2\sigma$ ) perturbation amplitude as a function of mass at $a = 1$ for the $\Lambda$ CDM(solid line) and WDM (dashed line) models. The verti- cal lines show the mass scales for 100 particles at the two resolutions. <i>Right:</i> Characteristic collapsed mass as a function of scale factor for the $\Lambda$ CDM(solid line) and WDM (dashed line) cosmologies. The solid horizontal lines show the mass scales for 100 particles at the two res- olutions. . . . .	105
7.5	The evolution of the power spectrum for halos in CDM (solid lines) and WDM (dashed lines) cosmologies. . . . .	108

7.6	The mass function for the CDM and WDM cosmologies (dark and light curves) at $a = 1$ and 100 for our larger volume simulations. . . . .	110
7.7	A comparison of the $M_{200}$ values for corresponding halos in the $\Lambda$ CDM and WDM runs at $a = 100$ . . . . .	113
7.8	The accretion history for three individual halos in the full run (solid curves) and their corresponding halos in the truncated run (dotted curves). . . . .	117
7.9	<i>Top Panel:</i> Average MAHs for CDM (diamonds) and WDM halos (plus symbols) from our large volume simulations. The halos are selected from the mass ranges $M_{200} = (1 - 4) \times 10^{13}$ , $(0.5 - 1.3) \times 10^{14}$ , and $> 4 \times 10^{14} h^{-1} \text{Mpc}$ . The curves are offset in $a$ by a factor of 2 (intermediate mass range) and 4 (low mass range) to make them easier to distinguish, but the short vertical lines represent $a = 1$ for all mass ranges. The dotted curves are fits to equations (7.8) for the CDM halos and the solid and dashed curves are fits to equation (7.9) for the CDM and WDM cosmologies. <i>Bottom Panel:</i> The mass growth rates, $d \ln(M_{200})/d \ln(a)$ , of the halos and plotted above and their fits to equation (7.9). Curves are offset in both the horizontal and vertical directions to make them more distinguishable. . . . .	119
7.10	Comparison of the formation epochs defined by W02 (equation 7.8) and our generalization (equation 7.9). . . . .	121

7.11	<i>Top Panels:</i> The dependence of halo's formation epoch ( $a_c$ in equation [7.9]) on mass. The left panel shows halos from the CDM run, and the right halos from the WDM cosmology. Dots represent halos from the large box run, and crosses are from the small box run. The solid and dashed curves show the trend of $a_c$ mass for the CDM and WDM cosmologies, and the vertical dotted line is $M_c$ . <i>Bottom Panel:</i> Same as the top panel, but now plotting the behavior of $\gamma$ , the amplification factor of equation (7.9), as a function of mass. . . . .	123
7.12	Residuals of average MAHs to various fits. . . . .	125
7.13	The evolution of the average number of subhalos in host halos of various masses. . . . .	128
7.14	<i>Top Panel:</i> Average density profiles times $r^2$ for all bound material in halos at $a = 100$ from our smaller volume runs. Halos selected according to the mass ranges $M_{200} = (2 - 4) \times 10^{13}$ (light line), $(0.6 - 1.3) \times 10^{14}$ (medium line), and $> 4 \times 10^{14} h^{-1} M_\odot$ (dark line), with the solid and dashed lines representing CDM and WDM halos. The profiles have been offset from each other to make them easier to see. <i>Middle Panel:</i> Residuals of NFW fits to the above six profiles. <i>Bottom Panel:</i> Residuals of truncated Hernquist fits (equation [7.11]) to the above six profiles. . . . .	130
7.15	The concentration ( $c_{200} = r_{200}/r_s$ ) as a function of mass for CDM and WDM halos at $a = 100$ . . . . .	133
7.16	The $a = 100$ concentrations as a function of formation epoch, $a_c$ from equation (7.9) for CDM and WDM halos. . . . .	134
A.1	This plot shows the overdensity required for the collapse of future structures as a function of the parameter $w$ appearing in the equation of state for quintessence models. . . . .	147

A.2	The maximum distance that a light signal can propagate between the present epoch and temporal infinity for an accelerating universe described by equation of state parameter $w$ . . . . .	148
C.1	<i>Left Panel:</i> The fraction of mass in a collapsed structure of a given mass as a function of mass for a number of WDM simulations with varying degrees of mass particle resolution ( $M_{particle} = 6.20 \times 10^8 - 3.97 \times 10^{10} h^{-1} M_{\odot}$ ) and simulated volume ( $50 - 200 h^{-1} \text{Mpc}$ ). The vertical dotted line represents the truncation scale, $M_c$ . <i>Right Panel:</i> The same mass fractions, now plotted mass in units of number of particles. . . . .	154
D.1	The radii in a halo enclosing a given number of particles as a function of time. . . . .	158

# LIST OF TABLES

## Table

4.1	Time Scales and Scale Factors . . . . .	72
7.1	Simulation parameters: . . . . .	100
7.2	Mass Function Parameters: . . . . .	110
7.3	RMS residuals of MAH fits: . . . . .	124
7.4	MAH Parameters: . . . . .	124

# LIST OF APPENDICES

## Appendix

A Quintessence . . . . .	145
B Dimensional Analysis . . . . .	150
C Mass Function . . . . .	153
D Stability of Halos . . . . .	156

## CHAPTER 1

# Introduction

The field of cosmology has recently reached a critical point. While the framework for a standard model of our universe has been in place for some time, recent experiments have measured many of the fundamental parameters of this model to percent level accuracy. Additionally, our theoretical understanding of astrophysical processes (such as galaxy formation) is beginning to link these processes with the larger structure of the universe. We have now entered an era of precision cosmology that has elevated it to the level of a “mature” field of science. In particular, we now know that the energy content of the universe is roughly 5% ordinary baryonic matter and 25% of a mysterious substance called dark matter that is collisionless and interacts through the gravitational and (most likely, for reasons of particle production) weak forces. The remaining 70% of the energy budget exists in an even more mysterious form known as dark energy whose defining property is that it is driving the universe into an epoch of accelerated expansion. While particle theory has produced a handful of reasonable possibilities for the dark matter, the community is at a loss to convincingly explain the dark energy, whose properties remain highly unconstrained.

In addition to knowing the constituents of the universe, we understand a substantial amount about how the universe evolves and structures form. During the early universe, tiny density perturbations (probably created by an inflationary epoch) are amplified by gravitational interactions once the epoch of matter domination begins. Once these perturbations reach a critical size they will collapse, forming virialized

objects known as dark matter halos. These early halos continue to grow through the accretion of diffuse matter and mergers with other halos. Once a halo is massive enough, accreted gas will be able to cool and collapse, forming stars, galaxies, and galaxy clusters inside the halo. While this general framework has recently become solidified, there are a number of details that remain unclear. This thesis will attempt to aid our understanding of this process by exploring the equilibrium structure of dark matter halos and the physical processes important for setting this structure. The work presented here is computational in nature and uses a suite of N-body simulations to examine both the large- and small-scale distribution of dark matter in the far future of the universe, and attempts to understand how this distribution came about.

This thesis is organized as follows. In chapters 2 and 3 I will give an overview of the current state of cosmology and cosmic structure followed by a discussion of cosmological N-body simulations, the simulations used for the studies in the following chapters. Chapters 4 - 7 present much of my research, which has been published under the references Busha et al. (2003), Adams et al. (2003), Busha et al. (2005), and Busha et al. (2007). Finally, I conclude in chapter 8, summarizing the main results from the previous chapters and discussing how this work fits into the broader context of community efforts.



## CHAPTER 2

# The Standard Model of Cosmology

The contemporary standard model of cosmology begins with the hot big bang paradigm. This paradigm assumes that the universe began in an initially hot, dense state, with energies comparable to the Planck scale,  $\sim 10^{19}\text{GeV}$ . No assumptions are made about the universe in this extreme state, where all of conventional physics breaks down. However, the universe has expanded and cooled since then, a process that is ultimately responsible for creating the stars and galaxies we observe today. This fantastic idea is supported by a suite of observations, known as the three pillars of the big bang. The first hint of this model came with the work of Hubble (1929), who measured a correlation between the radial velocities and distances of nearby galaxies. His measurements showed that, on average, all galaxies are receding away from us at a rate proportional to their distance, i.e., that the universe is expanding. This was a revolutionary conclusion since conventional wisdom at the time was that we lived in a static universe. While his measured expansion rate was several times larger than that of modern measurements (there were systematic errors in his distance measurements), this discovery was of such importance that the Hubble parameter,  $H$ , is named after him.

The second pillar is the presence of the cosmic microwave background (CMB). Gamow (1948) and Alpher & Herman (1948) realized that residual photons from the early hot, dense phase of the universe should have cooled to a few degrees above absolute zero in a blackbody spectrum. This radiation was first measured by Penzias

& Wilson (1965). Finally, in the 90's, the COBE satellite was able to accurately measure the spectrum as a near perfect blackbody with temperature  $2.735 \pm 0.06\text{K}$  (Mather et al., 1990). Continuous improvements of CMB measurements (de Bernardis et al., 2000; Spergel et al., 2003, 2006) have refined our knowledge of the universe, providing us with a wealth of information its geometry and contents.

Finally, because the universe has been cooling from a hot dense state of unbound quarks and other sub-atomic particles, we can understand the mechanisms responsible for forming the first elements in the universe. Big bang nucleosynthesis calculations predict that the universe should be dominated by light elements and predicts the relative abundances, hydrogen, helium, deuterium, and lithium, among others (Wagoner et al., 1967; Copi et al., 1994), which depend on the cosmic baryon to photon ratio. Recent observations of these abundances (O'Meara et al., 2001; Olive & Skillman, 2004) yield a ratio remarkably consistent with that from CMB measurements.

Using these observations, the big bang paradigm works with Einstein's theory of general relativity to predict the evolution of the universe as a whole. This chapter will present a number of aspects of this paradigm, including the evolution of the universe, dark matter, and large scale structure.

## 2.1 The Homogeneous Universe

While the standard model of cosmology resides within the big bang paradigm, it requires two additional assumptions: isotropy and homogeneity of the universe. Isotropy is the assumption that there are no preferred directions in the universe (everything looks the same, on large enough scales, every direction we look), while homogeneity assumes that there are no special places in the universe (on large enough scales, every region of space looks just like every other). Using these two assumptions, it is possible to solve Einstein's equations of general relativity, yielding a unique description for the expansion history of the universe that depends on only a handful of

cosmological parameters. Using this solution, it is possible to derive the evolution of both the universe as a whole and, if one includes the standard suite of fluid equations, of small density fluctuations in the universe that eventually form stars and galaxies. In this section we describe the expansion of the universe, while section 2.2 covers the evolution of density inhomogeneities.

We begin with Einstein's Equation,

$$R_{\mu\nu} - \frac{1}{2}Rg_{\mu\nu} + \Lambda g_{\mu\nu} = 8\pi GT_{\mu\nu}, \quad (2.1)$$

where  $g_{\mu\nu}$  is the metric tensor describing the geometry of the universe,  $R_{\mu\nu}$  and  $R$  are the Ricci tensor and scalar (both determined by the metric),  $G$  is Newton's Gravitational constant,  $T_{\mu\nu}$  is the stress-energy tensor (determined by the constituents of the universe), and  $\Lambda$  is the famous cosmological constant (see a text such as Carroll, 2004 for further discussion of these terms). The presence of  $\Lambda$  was originally postulated to keep the universe in a steady state before the observations of Hubble (1929) showed that the universe is expanding. Upon this discovery, the constant was thrown out, but has recently been re-introduced as an explanation of the observed accelerated expansion of the universe. If we treat the large-scale universe as a homogeneous fluid, the stress-energy tensor is determined entirely by the density,  $\rho$ , and pressure,  $p$  of the fluid,

$$T_{\mu\nu} = \begin{pmatrix} \rho & 0 & 0 & 0 \\ 0 & p & 0 & 0 \\ 0 & 0 & p & 0 \\ 0 & 0 & 0 & p \end{pmatrix}. \quad (2.2)$$

Now, all that's left to define is the metric, which can be determined using the assumptions of cosmological homogeneity and isotropy. The Robertson-Walker (RW) metric is the maximally symmetric metric satisfying these conditions. It is based on

a space-time interval of the form

$$ds^2 = -dt^2 + a^2(t) \left( \frac{dr^2}{1 - kr^2} + r^2 d\theta^2 + r^2 \sin^2 \theta \phi^2 \right), \quad (2.3)$$

where  $a(t)$  is the scale factor that determines the size of the universe and  $k$  is the curvature term and can be equal to -1, 0, or 1, depending on the geometry of the universe. As a side note, I should mention that it is sometimes conventional to change the sign of equation (2.3), making  $dt^2$  positive and  $a^2$  negative. This thesis, however, will use the above convention, consistent with Carroll (2004). The interval  $ds$  lets us immediately construct our metric:

$$g_{\mu\nu} = \begin{pmatrix} -1 & 0 & 0 & 0 \\ 0 & \frac{a(t)}{(1-kr^2)} & 0 & 0 \\ 0 & 0 & a(t)r & 0 \\ 0 & 0 & 0 & a(t)r\sin\theta \end{pmatrix}. \quad (2.4)$$

The metric is a modification of a static, flat space-time. A curvature term,  $k$ , is introduced in the 1-1 component, and all spatial components are multiplied by an evolving scale factor,  $a(t)$ . Using these relations, we can now solve Einstein's Equation.

The 0-0 component of equation (2.1) reduces to the famous Friedman equation:

$$\left( \frac{\dot{a}}{a} \right)^2 + \frac{k}{a^2} = \frac{8\pi G}{3} \rho + \frac{\Lambda}{3}. \quad (2.5)$$

This equation relates the expansion of the universe,  $\dot{a}$ , to the energy density and curvature. The other diagonal components of Einstein's equations can be combined for a constraint on the second time derivative of the scale factor,

$$2\frac{\ddot{a}}{a} + \left( \frac{\dot{a}}{a} \right)^2 + \frac{k}{a^2} = -8\pi G p + \Lambda. \quad (2.6)$$

This equation can be re-written in a slightly more useful form that depends only on the second derivative of the scale factor by using equation (2.5), yielding

$$\frac{\ddot{a}}{a} = -\frac{4\pi G}{3} (\rho + 3p) + \frac{\Lambda}{3}. \quad (2.7)$$

Here we see that the second derivative of the scale factor has no direct dependence on the geometry of the universe but does depend on both the energy density and pressure of the matter content.

One final piece of information needed to understand the evolution of  $a$  is the evolution of  $\rho$  with time. This is given through the fluid equation. Assuming conservation of energy on cosmological scales, consider the first law of thermodynamics for an adiabatic system,  $\dot{E} + P\dot{V} = 0$ . In a cosmological setting,  $\dot{V} = 3V\dot{a}/a$  and  $\dot{E} = \partial_t(\rho V) = \rho\dot{V} + V\dot{\rho}$ . This gives us the relation

$$\dot{\rho} + 3\frac{\dot{a}}{a}(\rho + P) = 0. \quad (2.8)$$

This equation tells us that the evolution of  $\rho$  with the scale factor depends ratio of  $\rho$  and  $P$ . In particular, we see that for collisionless matter ( $P = 0$ ) we get the relation  $\rho \propto a^{-3}$ . On the other hand, the constant,  $\Lambda$ , behaves like as a substance with  $\rho = -P$ . Once assumptions are made about  $\rho$  and  $P$  for all constituents of the universe, equations (2.5), (2.7) and (2.8) describe the full evolution of the scale factor,  $a$ . For the epochs this thesis is concerned with, the universe will be dominated by collisionless dark matter and a cosmological constant.

There are also a number of notational conventions that need to be addressed. Because the ratio appears so frequently, it is also convenient to define the Hubble parameter,  $H$ , as

$$H = \frac{\dot{a}}{a} = 100h\text{km/s/Mpc}. \quad (2.9)$$

This describes the rate of expansion of the universe. The parameter  $h$  is used as a convenient dimensionless version of  $H$ . Additionally, as a consequence of the growth of the scale factor,  $a$ , light emitted from a distant object will be stretched, or redshifted, before it reaches us. Consequently, while  $a$  can be used to define the age of the universe, the redshift,  $z$ , is frequently used instead as a more directly observable

quantity. The redshift is related to the expansion factor through

$$\frac{1}{z+1} = \frac{a}{a_0}. \quad (2.10)$$

The redshift,  $z$  is defined relative to some observation time,  $a_0$ , typically taken to be the value of the expansion factor today. Note that  $z$  is both a measure of time and distance, such that  $z = 0$  represents both the current epoch and the immediate vicinity. Also,  $a(\text{today})$  is typically normalized to 1. The normalization is arbitrary, but is allowed since  $a$  is a dimensionless parameter.

It is worth pointing out a special solution of equation (2.5). For a universe with no cosmological constant, the energy density required to create a flat universe ( $k = 0$ ) is known as the critical density and is given by

$$\rho_{crit} = \frac{3H^2}{8\pi G}. \quad (2.11)$$

It is customary to measure the density of components of the universe relative to this critical density,

$$\Omega_x = \frac{\rho_x}{\rho_{crit}} \quad (2.12)$$

where  $x$  is typically  $m$  (matter),  $r$  (radiation),  $\Lambda$  (the dark energy), or some other constituent of the universe. This parameter determines the fate of a matter-dominated universe. A universe with  $\Omega_{total} = 1$  is known as a flat universe. Such a universe will expand forever, but will slow down as it does so. The gravitational attraction of matter is just strong enough to counteract the expansion and  $\dot{a}$  asymptotes to zero as  $a \rightarrow \infty$ . If  $\Omega_{total} < 1$ , the universe is negatively curved ( $k = -1$ ) and the gravity is unable to counteract the expansion, causing the universe to grow to infinite size and reach a steady rate of expansion. A negatively curved universe has  $k = +1$  and  $\Omega_{total} > 1$ . Here, there is ample matter in the universe to slow and reverse the expansion, eventually causing a re-collapse with  $a \rightarrow 0$  at some non-zero time. The presence of  $\Lambda$  changes these fates, and in particular a universe with  $\Omega_{total} = 1$  will expand forever if  $\Lambda > 0$ .

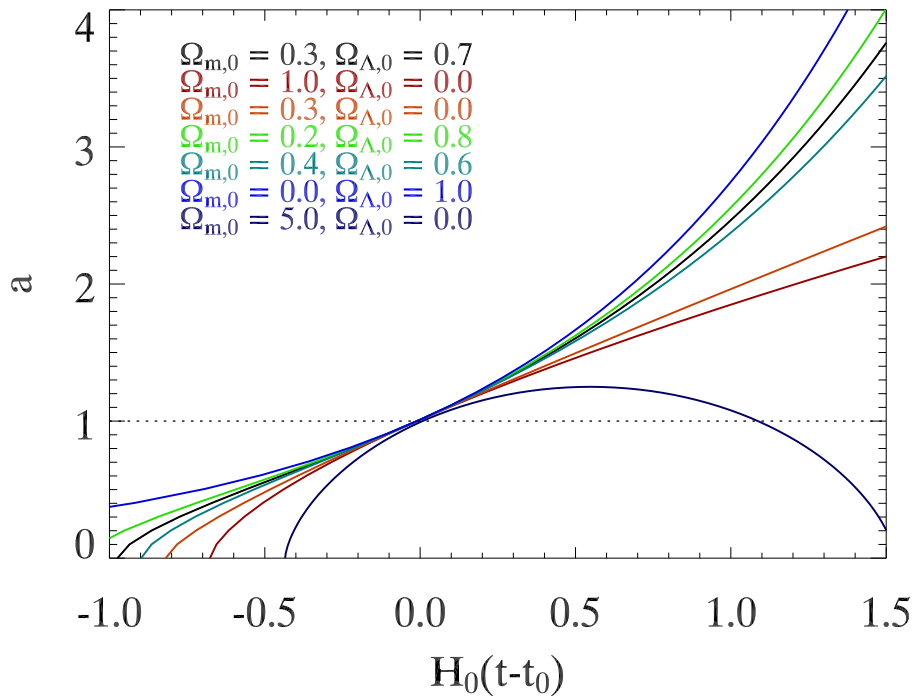


**Figure 2.1.** The evolution of the scale factor,  $a$ , for universes with various components. The dotted line,  $a = 1$ , represents the present epoch. All matter components are pressureless. The  $\Lambda$ -only universe was calculated using the constraint that the age of the universe was the same as in the  $\Omega_m = 0.3, \Omega_\Lambda = 0.7$  universe.

Figure 2.1 shows a series of solutions for the expansion of the universe from solving equation 2.5. Different colors represent universes with different matter and dark energy content. The black represents the concordance model universe, with  $\Omega_m = 0.3$  and  $\Omega_\Lambda = 0.7$ . The light and dark green lines show slight variations but retain  $\Omega_m + \Omega_\Lambda = 1$ . The red line represents the classic Einstein-deSitter universe with  $\Omega_m = 1$ . The orange and violet lines show open and closed universes, respectively. Finally, the dark blue line shows a  $\Lambda$ -only universe. The solution for such a universe, as discussed in section 2.3.2, is exponential expansion, which can never have  $a \rightarrow 0$ , so this solution was obtained under the constraint that the age of the universe be 13.5 Gyr with  $H_0 = 70\text{km/s/Mpc}$ , the same as the age of a concordance-model universe.

## 2.2 The Lumpy Universe

While the cosmological principle assumes that the large scale universe is homogeneous, we know from the presence of clusters, galaxies, stars, planets, and even ourselves, that homogeneity must break down on all but the largest scales. When combined with equations from classical mechanics, the Friedman equations give us the ability to predict much of the early evolution of inhomogeneities. They do not, however, provide us with a mechanism for generating the initial perturbations. The early perturbations can be measured through tiny anisotropies in the CMB, which correspond to small scale density fluctuations at the time the CMB was generated, roughly 300,000 years after the big bang, and can be accurately measured with the COBE and WMAP satellites. Characterizing these inhomogeneities allows us to reproduce the power spectrum of density perturbations at that time, giving us the ability generate initial conditions for numerical simulations (discussed in chapter 3) that statistically replicate our universe. One possible method for generating these perturbations, inflation, is discussed in section 2.3.3. Once the perturbations have been generated they grow through gravitational amplification, eventually becoming halos, galaxies, stars, and even planets.

As a quick note, the following discussion assumes that the matter content of the universe consists only of collisionless (pressureless), non-relativistic cold dark matter (CDM, which will be discussed more thoroughly in the next section). The inclusion of some sort of baryonic (collisional) matter adds complications that typically serve to retard the perturbation growth at early epochs, such as when the universe was hot enough that photons and ions were coupled. However, observations indicate that dark matter dominates over baryonic matter at all epochs. Additionally, once the universe cools enough for the photons and baryons to decouple the discussion becomes appropriate for the baryonic component as well. See Hu & Sugiyama (1996) for a complete discussion of the linear growth of the coupled photon-baryon-dark



matter system.

Limiting our discussion to weak perturbations (the kind present at recombination), we can use a Newtonian description. Consider a patch of space surrounding a spherical perturbation. This region will be described by the equations

$$\frac{\partial \rho}{\partial t} + \nabla \cdot (\mathbf{u}\rho) = 0 \quad (2.13)$$

$$\frac{\partial \mathbf{u}}{\partial t} + (\mathbf{u} \cdot \nabla) \mathbf{u} = -\nabla \phi \quad (2.14)$$

$$\nabla^2 \phi = 4\pi G \rho \quad (2.15)$$

where equations (2.13), (2.14) and (2.15) are the continuity equation, Euler's equation, and Poisson's equation, respectively (Peebles, 1980). Here,  $\mathbf{u}$  is the velocity of a fluid element, and  $\phi$  is the gravitational potential. The above equations assume that we are working in the proper, physical coordinate system. In order to continue our analysis, we will convert these equations into comoving coordinates,

$$\mathbf{r} = a(t)\mathbf{x}, \quad (2.16)$$

where  $r$  represents the physical (proper) position and  $a$  is the expansion factor. The comoving coordinate,  $x$ , is just the physical location with the effects from the expansion of the universe removed, i.e., a coordinate system that grows with the universe. We can also relate the physical velocity,  $\mathbf{u}$ , to a peculiar velocity,  $\mathbf{v}$ , using

$$\mathbf{u} = \dot{\mathbf{r}} = \dot{a}\mathbf{x} + a\dot{\mathbf{x}} = \dot{a}\mathbf{x} + \mathbf{v}. \quad (2.17)$$

In this system,  $\mathbf{v}$  is the velocity relative to the background universe, which ignores motion induced by the Hubble expansion.

In order to convert equations (2.13), (2.14), and (2.15) to a comoving system we must transform both the coordinates and the derivatives, which act on a specific coordinate system. The derivatives are transformed by

$$\left(\frac{\partial}{\partial t}\right)_r = \left(\frac{\partial}{\partial t}\right)_x - H(\mathbf{x} \cdot \nabla_{\mathbf{x}}) \quad (2.18)$$

$$\nabla_{\mathbf{r}} = a^{-1}\nabla_{\mathbf{x}}. \quad (2.19)$$

Here, the subscripts refer to the coordinate system. Finally, instead of considering actual densities, we will consider a field of dimensionless density perturbations,  $\delta(\mathbf{x}, t)$ , such that

$$\delta(\mathbf{x}, t) = \frac{\rho(\mathbf{x}, t) - \bar{\rho}(t)}{\bar{\rho}(t)}. \quad (2.20)$$

Here  $\bar{\rho}$  is the mean matter density of the universe. This is a more useful notation because it deals directly with the growth of inhomogeneities relative to the background mass distribution, which is itself evolving with  $a$ . Using the identities from equations (2.16 - 2.20), we can transform equations (2.13), (2.14), and (2.15) to their comoving forms:

$$\frac{\partial \delta}{\partial t} + \frac{1}{a} \nabla_{\mathbf{x}} \cdot (1 + \delta) \mathbf{v} = 0 \quad (2.21)$$

$$\frac{\partial \mathbf{v}}{\partial t} + \mathbf{v} \frac{\dot{a}}{a} + \frac{1}{a} (\mathbf{v} \cdot \nabla_{\mathbf{x}}) \mathbf{v} = -\frac{1}{a} \nabla_{\mathbf{x}} \tilde{\phi} \quad (2.22)$$

$$\frac{1}{a^2} \nabla_x \tilde{\phi} = 4\pi G \bar{\rho} \delta \quad (2.23)$$

$$\tilde{\phi} = \phi + \frac{1}{2} a \ddot{a} r^2. \quad (2.24)$$

Using these equations, we can derive an analytic solution describing the growth of perturbations. We restrict ourselves to linear perturbations, where  $\delta \ll 1$  and  $(\mathbf{v}t/d)^2 \ll \delta$ . The former condition requires that the size of the perturbations is small. In the latter condition,  $d$  and  $t$  represent the characteristic size and expansion time of a perturbation, which makes sure that the expansion cannot act as a form of pressure support.

In order to study the growth of inhomogeneities, we will consider the perturbations in Fourier space,  $\delta_{\mathbf{k}} = \frac{1}{V} \int dV \delta(\mathbf{x}, t) e^{-i\mathbf{k} \cdot \mathbf{x}}$ . Transforming equations (2.21) and (2.22) into Fourier space gives us

$$\frac{d\delta_{\mathbf{k}}}{dt} + \frac{i}{a} \mathbf{k} \cdot \mathbf{v}_{\mathbf{k}} + \frac{1}{a} \sum_{\mathbf{k}'} i \delta_{\mathbf{k}'} (\mathbf{k} \cdot \mathbf{v}_{\mathbf{k}-\mathbf{k}'}) = 0 \quad (2.25)$$

$$\frac{d\mathbf{v}_{\mathbf{k}}}{dt} + H \mathbf{v}_{\mathbf{k}} + \frac{i}{a} \sum_{\mathbf{k}'} [\mathbf{v}_{\mathbf{k}'} \cdot (\mathbf{k} - \mathbf{k}')] \mathbf{v}_{\mathbf{k}-\mathbf{k}'} = -\frac{i\mathbf{k}}{a} \tilde{\phi}_{\mathbf{k}} \quad (2.26)$$

$$\tilde{\phi}_l = -4\pi G \bar{\rho} a^2 \frac{\delta_{\mathbf{k}}}{|\mathbf{k}|}, \quad (2.27)$$

where  $\mathbf{v}_{\mathbf{k}}$  is the Fourier transforms of  $\mathbf{v}$ . Our restriction to the linear regime lets us ignore the mode coupling terms — the sums over  $\mathbf{k}'$  in equations (2.25) and (2.26). This has the benefit of making each mode independent of all other modes, allowing us to consider perturbations of a specific  $\mathbf{k}$ . Combining these equations gives us a differential equation describing the evolution of a density perturbation in the linear regime:

$$\ddot{\delta}_{\mathbf{k}} + 2H(t)\dot{\delta}_{\mathbf{k}} - 4\pi G\bar{\rho}(t)\delta_{\mathbf{k}} = 0. \quad (2.28)$$

This equation is similar to a damped harmonic oscillator. The  $4\pi G\bar{\rho}(t)$  terms acts as the “restoring” force, although gravity acts in the opposite direction and attempts to make an overdense region more overdense. The  $2H$  term is a linear damping force — the Hubble expansion attempting to washout the overdensity. These competing terms create two solutions to equation (2.28), one for growing modes and another for decaying modes. However, in order to solve equation (2.28) for perturbation evolution, you must understand the evolution of the Hubble parameter, which is set by the cosmological parameters  $\Omega_m$  and  $\Omega_\Lambda$ .

As an example, consider an Einstein-deSitter universe with  $\Omega_m = 1$  at all times. Equation (2.5) can be solved, yielding  $a \propto t^{2/3}$  and  $H = (3/2t)^2$ . Plugging this into equation (2.28), we find two power-law solutions,

$$\delta_k = A_k t^{2/3} + B_k t^{-1}. \quad (2.29)$$

As expected, there is both a growing and a decaying mode. Because the initial perturbations were small when formed, and the scale factor has grown by many orders of magnitude since then, the decaying mode can be ignored as a small correction. Doing this, we see that, in an Einstein-deSitter universe, perturbations grow like  $\delta_k \propto a$ . In order to generalize the solutions of equation (2.28) to an arbitrary cosmology, it is customary to introduce the linear growth function,  $D$ , such that  $\delta_k(t) = D(t)\delta_k(t_0)$ . In general,  $D$  must be solved through numerical integration.

While equation (2.28) is useful for tracking the evolution of an individual perturbation, one thing that still has yet to be specified is the initial distribution of perturbations. This is something that must be measured and results in the addition of several new cosmological parameters. The perturbation distribution is characterized by the input power spectrum,

$$P(k) = \langle |\delta_k|^2 \rangle. \quad (2.30)$$

The initial power spectrum generated from inflation is predicted to nearly be a power law,  $P(k) \propto k^n$ , and can be measured almost directly from the CMB. This introduces two additional parameters needed to characterize the cosmology — the spectral index,  $n$ , and the amplitude of perturbations,  $\sigma_8$ . Measurements of the spectral index puts it close to the scale-free value,  $n = 1$  (Spergel et al., 2006). Physical processes during the earliest times (in particular during the radiation-dominated epoch) will cause this power law to break. The details of this process are beyond the scope of this dissertation, but the exact evolution of the power spectrum during these epochs can be found in Seljak & Zaldarriaga (1996).

Using these conventions, we can describe the growth of inhomogeneities in the cosmic density field through the linear regime. These results break down when perturbations enter the non-linear regime,  $\delta \sim 1$ . Unfortunately, most cosmic structures (i.e., galaxies and clusters) have  $\delta \gg 1$ . Consequently, we must resort to numerical methods, such as N-body simulations, to study this regime. These simulations are discussed in chapter 3.

## 2.3 The Dark Universe

In order to complete the Big Bang model and understand how it applies to our universe, the components of our universe and a method for generating initial density perturbations must be specified. In this section we focus on the concepts of dark matter, dark energy, and inflation which complete this paradigm.

### 2.3.1 Dark Matter

Dark Matter is a form non-baryonic matter that does not interact electromagnetically, making it collisionless and incapable of forming stars and galaxies, or even of being directly observed by ordinary telescopes. While regions of high dark matter density do exist, it is virtually impossible for dark matter to form extremely dense objects, such as planets, because the lack of electromagnetic interactions make it difficult for a collection of dark matter particles to dissipate energy and angular momentum in the same way that baryons do.

Because we cannot see dark matter directly, we must study it by understanding the effects it has on galaxies and other objects we regularly study. The presence of dark matter was first hinted at by Zwicky (1937), who noted that, if a reasonable mass to light ratio was assumed, the total mass in nearby galaxy clusters was much too small to keep the galaxies gravitationally bound to each other. There had to be some additional invisible matter present if the systems were in equilibrium and not just chance juxtaposition of galaxies passing by each other. This idea of missing mass was further strengthened with the work of Rubin et al. (1985) who measured the rotation curves of many galaxies. If mass traced the luminous part of galaxies, such rotation curves should fall off at large radii. This work, however, discovered that rotation curves were flat out to regions where the luminosity was very low, indicating that a substantial amount of mass in a galaxy was non-luminous.

While these results indicated that there was indeed a “missing matter” problem, they allowed for the possibility that this matter was baryonic. However, measurements of element abundances from big bang nucleosynthesis constrain the abundance of baryonic matter to be only a few percent of the universal critical density. This was in contradiction with both the theoretical expectation that  $\Omega_m = 1$ , and cluster surveys which were converging towards  $\Omega_m = 0.3$ . In either scenario, the balance of the missing mass must be non-baryonic. While we still have yet to directly detect

the presence of dark matter, recent lensing observations and the now famous “Bullet Cluster” (Clowe et al., 2006) provide almost irrefutable evidence for the presence of non-baryonic dark matter. The bullet cluster is a system of two galaxy clusters undergoing a major merger, with one cluster having just passed through the center of the other. Weak lensing measurements of the mass distribution reveals two mass peaks. First, there is a weak peak near the center of the merging systems coincident with a strong x-ray signal, revealing the presence of a large amount of collisional gas that is being shock heated. A second, stronger peak, is more advanced, and is coincident with the collisionless galaxies of the penetrating cluster that are unable to lose energy through heating and therefore pass freely through the cluster. This mass peak is much too strong to be accounted for by the stars, requiring some additional collisionless component that dominates the system gravitationally — the non-baryonic dark matter. Particle theorists have postulated a number of reasonable candidates for this matter, candidates that may be observable in the next generation particle accelerators that are currently under construction.

**Classes of Dark Matter** Because chapter 7 of this thesis will consider the effects of the dark matter properties on cosmic structure, it is necessary to discuss the different classes of dark matter, in particular Cold, Hot, and Warm Dark Matter (CDM, HDM, WDM). As discussed above, a host of observations relying on different physics points to the presence of a collisionless, non-baryonic component of the universe that dominates over baryonic matter. While the exact nature of this particle (or particles) remains unknown, we have many important constraints on its properties. Aside from the knowledge that dark matter interacts primarily through the gravitational force (although most theories also require a weak interaction for particle production purposes), we also have an upper limit on the dark matter velocity dispersion, which in turn puts a lower limit on the mass for most conventional dark matter candidates.

When theories of dark matter were first being postulated, candidates fell broadly into two main categories: Cold and Hot Dark Matter. HDM consists of low-mass particles that were relativistic at the time of decoupling from radiation, resulting in a large intrinsic velocity dispersion. These high dispersions wash out density perturbations at scales below the free streaming length (which can be converted to a mass scale using the universal background density). Although the exact cutoff point in the power spectrum is model dependent, this scale is typically around a cluster mass,  $M \sim 10^{14} h^{-1} M_{\odot}$ . HDM models were initially popular because the neutrino was known to be an abundant weakly-interacting particle that probably had a mass that was small but potentially large enough for neutrinos to be dominant over the baryon population. Current measurements, however, put the total contribution of neutrinos to the mass budget of the universe at about the 0.1% level.

CDM particles, on the other hand, have much higher masses, making them non-relativistic when they decoupled from radiation. This gives them a low intrinsic velocity dispersion that will not wash out inhomogeneities, allowing perturbations to persist down to earth-mass scales and below. Typical CDM candidates are the lightest supersymmetric particles predicted from particle theory, such as the gravitino. While we have yet to observe any of these particles directly, the next-generation particle accelerators that will be coming online in a few years are expected to produce them, and much of the particle physics community believes that they will be found. Intermediate models, such as Warm Dark Matter (WDM), are also possible. Here, density perturbations are washed out on a modest galaxy or galaxy group scale. For completeness, I should also note that it is possible to postulate low mass CDM particles such as axions. See Kolb & Turner (1990) for a further discussion.

As we will discuss in section 2.4 and chapter 7, the presence or absence of low mass density perturbations has a profound effect on process of structure formation. It is primarily through studying these effects that we have been able to rule-out the HDM

and WDM scenarios. The CDM paradigm has been firmly established as correct model for our universe.

### 2.3.2 Dark Energy

In addition to the unexpected dark matter, a more inexplicable component of the universe is dark energy (which, in spite of its name, has nothing to do with dark matter). Because of the strictly attractive nature of gravity, one expects the expansion of the universe to be decelerating. However, measurements of the expansion history of the universe from distant supernovae indicate that the expansion is actually *accelerating* (Garnavich et al., 1998; Perlmutter et al., 1999). As seen in equation 2.7, this can be caused by a cosmological constant or some other form of exotic energy with  $\rho > -p/3$  (as noted above,  $\Lambda$  is effectively a uniformly distributed substance with  $\rho = -p$ ). This acts as a substance that is gravitationally repulsively. In addition to acceleration measurements, the presence of such dark energy is supported by CMB and large scale structure measurements. CMB measurements, with minimum priors, put a tight constraint  $\Omega_{total}$  for the universe that is tantalizingly close to unity. When combined with large-scale structure measurements, however, the total matter content of the universe sits somewhere around 30%, which requires dark energy to make up roughly 70% of the total mass/energy budget of the universe. While the universe seems to have the theoretically-desirable critical density, stars and other familiar object make up only a few percent of the universe. Some unknown form of matter makes up roughly a third of the universe. The bulk of the energy in the universe, however, is in some substance of a truly unknown form. While the scientific community is currently at a loss to explain this substance (particle physicists have come up with a plethora of models), observations are improving and it is becoming possible to rule out more and more models of dark energy. Indeed, it is beginning to look more and more likely that the dark energy is caused by the simplest of all



models, a cosmological constant.

Equation 2.7 tells us about the acceleration or deceleration, and fate, of the universe. In the absence of a cosmological constant, the expansion of the universe will decelerate as long as  $\rho > -p/3$ , eventually leading to collapse if the density is high enough. Expansion will accelerate, however, for  $\rho < -p/3$ . The cosmological constant, with  $\rho = -p$ , induces an epoch of exponential, or deSitter expansion. During this phase, the universe grows very rapidly, with

$$a \propto e^{t\sqrt{\frac{\Lambda}{3}}}. \quad (2.31)$$

Because  $\dot{\rho}_\Lambda = 0$  and  $\dot{\rho}_X < 0$  for matter and radiation, any universe with a non-zero cosmological constant will enter this phase, which, as discussed later in this thesis, has substantial ramifications for the future of large-scale structure.

### 2.3.3 Inflation

While section 2.2 discussed the evolution of density perturbations, we have yet to address the origin of these perturbations. The exact method for their generation is still unknown, but the most popular explanation is to assume that the universe went through an early phase of deSitter expansion known as inflation.

Like the big bang itself, inflation is a paradigm that serves to simultaneously solve several problems. Originally postulated by Guth (1981), it addressed three distinct problems: 1.) Why do we not observe any magnetic monopoles? Theories predict that, as the early universe cooled enough to break symmetries, monopoles should have been produced in great numbers and be regularly observed today. However, we have yet to see one. 2.) Why is the universe so close to flat? Current measurements that put  $\Omega_{total} = 1.06 \pm 0.04$  (Tegmark et al., 2004). The Friedman equations, however, dictate that  $|\Omega_{total} - 1| = |k|/\dot{a}^2$ , causing the universe to become less flat as it decelerates. In order to achieve the level of flatness we see today, we must have  $|\Omega_{total} - 1| < \mathcal{O}(10^{-16})$  during the time of nucleosynthesis, making  $\Omega_{total}$  an extremely

fine-tuned parameter. 3.) Why does the CMB have a constant temperature? In the standard big bang paradigm, the CMB is made up of several causally disconnected regions, so there is no reason for two points on opposite ends of the sky to have similar temperatures as observed.

A phase of early deSitter expansion, where the scale factor increases by  $\gtrsim 60$   $e$ -foldings, solves all of these problems. Monopoles can still be created, but they get diluted by the rapid expansion. The accelerated expansion both drives the universe towards flatness and pushes previously causally connected regions to distances that are larger than the Hubble radius at the epoch when inflation ends and the universe resumes its decelerating expansion.

An added benefit of inflation is that it acts as a natural method for perturbation generation. Picturing inflation as being caused by some scalar field,  $\phi$ , quantum uncertainties in the exact value of  $\phi$  causes inflation to behave slightly differently at different regions of space. Effectively, this magnifies quantum-scale uncertainties to become tiny variations in the energy distribution of the matter in an otherwise homogeneous universe to the point where they become macroscopic density perturbations. This produces a distribution of inhomogeneities that are free to continue their growth through gravitational amplification.

## 2.4 Large Scale Structure

The most recently virialized objects in the universe, massive dark matter halos that are host to galaxies and galaxy clusters, make up the large scale structure of the universe. While the study of large scale structure is a broad, active area of research, in this section I will focus how structure is formed in different dark matter scenarios and the inner structure of these halos.

### 2.4.1 Halo Formation

As discussed in section 2.3.1, an intrinsic velocity dispersion serves to wash out density perturbations at cluster-mass and lower scales in HDM cosmologies. The first structures to collapse are high-mass objects that form almost through a monolithic-like collapse process. Instead of collapsing spherically, these massive perturbations tend to go non-linear along a single axis first, resulting in a large “Zel’dovich-pancake” (Zel’Dovich, 1970). The baryons inside such an object will be able to cool through collisions, causing the pancake to break-up into galaxy sized clumps through a process known as “top-down” structure formation. Here, larger structures form first and are older than smaller objects. Simulations show that, in order to reproduce the observed local galaxy distribution, such a collapse and fragment must have occurred rather recently (White et al., 1983). This produces a large number of galaxies at the present epoch, but a very sparse number mainly high mass objects at higher redshifts. On the contrary, galaxies have been observed out to  $z \sim 6$ , while clusters are observed only out to  $z \sim 1.5$  (Mullis et al., 2005; Berger et al., 2006)

In contrast, the small perturbations in CDM cosmologies cause structure to form from the bottom-up, through what is known as hierarchical structure formation. Because the initial perturbation spectrum is mode-independent and very nearly scale-free, small and large perturbations will coexist in the same spatial region. In particular, long-wavelength perturbations creating large, generally overdense regions, will amplify high  $k$  perturbations sitting on this larger mode. These amplified perturbations will go non-linear and collapse first, creating extremely low-mass objects that will form larger structures by merging with each other and accreting from the surroundings (Davis et al., 1985; Diemand et al., 2005; Gao et al., 2005). The resulting distribution of galaxies closely matches what we observe — more massive clusters are relatively young objects, while galaxies and their halos are present out to high redshift.

One additional consequence of the hierarchical process is presence of substructure. While tidal stripping and other disruption processes will have an important effect, when smaller halos merge with larger objects their tightly bound cores frequently survive and orbit as a small halo inside a larger one. Indeed, this abundance of substructure is readily observed in large halos in simulations, as well as in observations of the dwarf galaxies in our local group.

While the CDM paradigm has been very successful in explaining the galaxy distribution, it still has some shortcomings such as the so-called missing substructure problem for smaller halos. First noted by Moore et al. (1999a), galaxy-sized halos in simulations have an order of magnitude more substructure than measured in our local group. One of the first proposed solutions to this problem was the warm dark matter model, a hybrid CDM/HDM cosmology. Here, the mass/velocity dispersion of the dark matter particle is tuned such that perturbations below a specified mass scale are washed out, suppressing the formation of the smallest objects but still allowing hierarchical formation starting with dwarf-galaxy sized objects. Such models, however, are heavily constrained by observations of the Ly- $\alpha$  forest. Here, the absorption spectra of distant quasars are measured as the light passes through neutral hydrogen in the intergalactic medium, effectively tracing the dark matter distribution at  $z \sim 2 - 4$ . The most recent results constrain the mass of the dark matter particles to be  $> 13\text{keV}$  at the 95% confidence level, creating a free streaming length of roughly 4 kpc (Seljak et al., 2006), well below the resolution limit of the simulations presented here. The community is slowly coming to the consensus that the missing substructure problem is solved by so-called “dark-dark halos,” small halos that, for various reasons, are unable to form stars or keep much of their gas, making them invisible to most forms of observation except lensing surveys (Shaviv & Dekel, 2003). Even though the WDM cosmologies discussed in chapter 7 have been confidently ruled out, we present them as a method to study the importance of mass accretion in setting

the inner structure of a dark matter halo.

### 2.4.2 CDM Halos

While I have spent much time discussing the growth of density perturbations and formation of dark matter halos, I have spent little time actually discussing what the halos themselves look like. The first simulation to form a halo in a cosmological simulation was Peebles (1970). This simulation used 300 particles in an attempt to model the Coma cluster (which, by comparison, has roughly 800 galaxies). This crude simulation resulted in a virialized structure with a density profile steeper than the isothermal model,  $\rho \propto r^{-2}$  expected for a system of collisional gas. As computing power increased, halos were resolved with more and more particles and the community began to converge towards a “universal” halo density profile. First proposed by Navarro et al. (1996a), this profile has the form

$$\rho_{NFW} = \frac{4\rho_s}{r/r_s(1+r/r_s)^2}. \quad (2.32)$$

This can be thought of as either a 1 or 2 parameter fit:  $r_s$  is the scale radius, while  $\rho_s$  is the density at that radius. The profile is characterized by an inner density cusp of  $\rho \propto r^{-1}$  and outer slope  $\rho \propto r^{-3}$ . The scale radius,  $r_s$ , is where the profile has the isothermal slope of  $r^{-2}$ . Frequently, the scale factor is re-parameterized as the halo concentration,

$$c_{200} = r_{200}/r_s, \quad (2.33)$$

where  $r_{200}$  is a proxy for the virialized radius of the halo (see section 3.4 and chapter 6). The higher the concentration, the higher the mean interior density of the halo. This parameterization is often used because of an argument that the concentration should correlate to the halo formation epoch. The core of the halo should form through a period of early accretion. The central density should thereby reflect the background density of the universe at this epoch, while the outer regions will be accreted later. In

this way, a higher concentration (core density) should correspond an earlier formation time because of the higher universal background density at earlier epochs.

While the NFW profile has remained the standard halo density profile since its initial introduction, there have been a number of conflicts regarding the exact value of the inner slope. Measurements of steeper slopes at the inner radii by Moore et al. (1999b) and Fukushige & Makino (2001) prompted the introduction of a profile of the form

$$\rho_M = \frac{2\rho_M}{(r/r_M)^{1.5}[1 + (r/r_M)^{1.5}]} \quad (2.34)$$

This profile agrees with the NFW profile at large radii, but has a steeper inner cusp of  $r^{-1.5}$ . The difficulty in measuring the inner slope correctly lies in how finely we can resolve the inner regions of the numerical halo without having to worry about relaxation effects (see the chapter 3 and appendix D for a discussion of these effects). At the present, it looks like at the innermost resolved radii from the most highly resolved simulations (typically  $\sim 1\%$  of  $r_{200}$ ) that the inner slope is in the range  $0.9 - 1.2$  (Navarro et al., 2004; Diemand et al., 2007), but the slope at these radii appears to be getting shallower and it is hard to tell if the slope will actually converge when higher and higher resolution is used.

The primary reason that the exact value of the inner slope has achieved so much attention is that this is the only scale that can be reliably compared to observations. While the few X-ray studies of galaxy clusters that accurately map the density profile out to large radii generally agree with the NFW form (David et al., 2001), much more work has been done measuring the rotation curves of low surface brightness (LSB) galaxies. These galaxies are generally considered to be more dark matter dominated than their brighter counterparts, making them the best laboratory for measuring the dark matter density profile. This is typically done through rotation curves which, unfortunately, can only be measured out to  $\sim 5\%$  of  $r_{200}$ , giving us a very small region of overlap. These studies indicate that in this region the density profile seems

to be constant with radius (Salucci & Burkert, 2000; de Blok et al., 2001; Gentile et al., 2004), in contradiction with simulations. While there have been a number of proposed solutions to this problem, such as the idea that the triaxiality of halos at the innermost radii can create orbits that trace a cored density profile when projected to two dimensions (Hayashi & Navarro, 2006), it is important to remember that this inner region is the region most affected by presence of baryons, including stellar populations and active galactic nuclei, which we have yet to be able to simulate accurately. It is very likely that this contradiction is simply the result of simulations failing to account for the relevant physics in this regime.

While much progress has been made in quantifying the dark matter density profile, studies into the origin of this profile have been met with limited success. Numerous toy models have been introduced to explain the concentration distribution (Navarro et al., 1996a; Eke et al., 2001), but they all lack a strong physical motivation. There have also been a number of studies attempting to connect the real space distribution with velocity information. Taylor & Navarro (2001) noted that phase space profile ( $\rho/\sigma^3$ ) follows a featureless power law. A number of studies have reproduced this result (Ascasibar et al., 2004; Rasia et al., 2004), but none have been able to present a physical motivation for the slope or explain why it should be a featureless power-law. Motivated by the models connecting the distribution function, anisotropy, and density in Binney & Tremaine (1987), work by Dehnen & McLaughlin (2005) showed that, assuming a power-law  $\rho/\sigma^3$  profile, families of density profiles resembling NFW could be derived if one assumed information about the velocity anisotropy through the Jeans equation. Similarly, Hansen & Stadel (2006) showed that the density profile and isotropy parameters are tightly coupled in a power law relation. However, instead of explaining the origin of the density profile, these studies have just reduced it to equivalent problems. Further discussion of theories of the origin of this profile and the processes relevant in setting halo structure, as well as my work examining the

effect that accretion history has on halo structure, appears in chapter 7.

## 2.5 Cosmological Parameters

While equations (2.5) and (2.7) work well to describe the evolution of the universe, they are not complete in the sense that, in order to solve for the evolution of  $a$ , it is necessary to specify a number of parameters whose values can only be determined through observations. While the exact number of parameters needed to sufficiently describe our universe is still a point of debate, several parameters are universally agreed upon. First, we must specify  $\Omega_{m,0}$  and  $\Omega_{\Lambda,0}$ , the energy densities of matter and dark energy at some specific time. These parameters combine to give the total energy content and curvature,  $k$ , of the universe (radiation will also contribute to the total energy density, but at an extremely small level that is can be ignored if we are not concerned with the very early universe). In addition to knowing the amount of dark energy, we must also characterize its equation of state,  $w = P/\rho$ , where  $w = -1$  for a cosmological constant. We must also specify  $H_0$ , the value of the Hubble parameter at that epoch. These parameters are sufficient to solve the Friedman equations and describe the expansion of the homogeneous universe. However, they are insufficient for describing the growth of structure, and a few more must be introduced. At minimum, two parameters are needed to characterize the perturbation spectrum, the spectral index,  $n$ , and the amplitude of perturbations,  $\sigma_8$ .

As eluded to above, there have been a number of recent observations that have put stringent bounds on a number of these parameters. In particular, combined measurements of the CMB and cluster surveys have but a very tight constraint on the total energy density of our universe,  $\Omega_{tot} = 1.058_{-0.041}^{+0.039}$  (Tegmark et al., 2004). Many cosmologists consider this constraint strong enough to impose the prior  $k = 0$  when analyzing observational data. When measurements of the recession speeds of distant supernovae are added, a concordance model begins to emerge with all measurements



agreeing that the universe has  $h = 0.72 \pm 0.08$ ,  $\Omega_m = 0.266^{+0.026}_{-0.036}$ , and  $\Omega_\Lambda = 0.758^{+0.035}_{-0.058}$  (Spergel et al., 2006). Constraints on the dark energy equation of state are much less precise, but they do appear to be zeroing in on the cosmological constant value,  $w = -1$ , to 10%-20% accuracy (Riess et al., 2004; Angulo et al., 2005). Experiments to determine the constituents and properties of the universe have come a long way in the past 80 years since Hubble first postulated the expansion of the universe and no evidence for dark energy had been observed. These same experiment also puts tight constraints on the spectral index,  $n = 0.961 \pm 0.017$ .

For reasons of convention, the normalization of the power spectrum,  $\sigma_8$ , is measured by the average size of a linearly extrapolated density perturbation in a sphere with radius 8Mpc. The 8Mpc scale was originally selected because early results indicated that  $\sigma_8 = 1$ . This parameter is probably best measured through galaxy surveys, and is one of the most poorly constrained cosmological parameters, primarily because it has such strong degeneracies with a number of other parameters. Recent observations from a variety of studies using the CMB and lensing surveys measure  $\sigma_8 = 0.7 - 0.9$  (van den Bosch et al., 2005; Van Waerbeke et al., 2005; Spergel et al., 2006).

Knowing the components of the universe, it is now possible to determine its long-term fate. As discussed above, even though our universe has  $\Omega_m < 1$ , the presence of the dark energy closes the universe so  $k = 0$ . The equation of the state of the dark energy, which has recently become the dominant component, however, has caused the universe to enter a phase of exponential expansion. Assuming that the dark energy comes from a cosmological constant, the universe will grow to infinite size, isolating all structures. We must admit, however, that the nature of the dark energy is extremely uncertain, and it is possible that it consists of some even more exotic substance that could decay into an entirely new form of energy with  $\rho > -p/3$ , potentially changing the universal fate.

## CHAPTER 3

# Cosmological N-body Simulations

In this chapter I discuss cosmological N-body simulations, the primary tool used for the research presented in this thesis. As mentioned in the previous chapter, we are only able to analytically solve the equations of evolution for weak, non-linear density perturbations. As cosmic inhomogeneities grow, they eventually collapse through a highly non-linear process that is characterized by the continual accretion of mass and hierarchical merging of objects in a CDM-dominated universe. These non-linear structures are the objects that we directly observe in surveys. In order to understand the growth of cosmic structure during these processes, it has been necessary to resort to computer simulations. Such simulations can be used to both bridge the gap between theoretical predictions to observations and to study cosmological objects under idealized conditions that we will never be able to observe. While a number of techniques have been developed to solve this problem, this chapter will only discuss the techniques utilized in the dark matter-only simulations presented in this thesis, which were run using the code Gadget (Springel et al., 2001b; Springel, 2005). For a more complete description of N-body simulations, including the implementation of gas dynamics, see the reviews of Hockney & Eastwood (1981) and Bertschinger (1998).

The idea behind a N-body simulation is to map a continuous density field,  $\rho(\mathbf{x})$ , to a discrete set,  $m_i\delta(\mathbf{x} - \mathbf{x}_i)$ , that is treated as a distribution of interacting point-particles. Force interactions between the point particles can be calculated directly

through Newtonian methods. At their most basic, cosmological N-body simulations consider only gravitational interactions and calculate the force on each particle due to all other simulation particles,

$$F_i = \sum_{j \neq i} \frac{Gm_i m_j}{r_{ij}^2}. \quad (3.1)$$

While essentially correct, this is a highly inefficient algorithm since the number of force calculations for a set of  $n$  gravitationally interacting particles scales as  $\mathcal{O}(n^2)$ . Because it is not feasible to scale such computations to large numbers of particles (with the possible exception of special purpose hardware such as GRAPE, Okumura et al., 1993) it has been necessary to develop both faster algorithms and parallel techniques. The idea behind the more advanced algorithms has been to use direct force summation for nearby particles, but to determine the force from distant collections of particles using a multipole expansion of the potential (Binney & Tremaine, 1987),

$$\Phi(r, \theta, \phi) = -4\pi G \sum_{l,m} \frac{Y_l^m(\theta, \phi)}{2l+1} \left[ \frac{1}{r^{l+1}} \int_0^r \rho_{lm}(a) a^{(l+2)} da + r^l \int_r^\infty \rho_{lm}(a) \frac{da}{a^{l-1}} \right]. \quad (3.2)$$

This is analogous to the multipole expansion from electrodynamics (Jackson, 1999). As with the electrostatic expansion, the monopole term ( $l = 0$ ) approximates the potential assuming that all mass in the collection is located at the center of mass. The lack of anything analogous to a negative charge, however, requires that all higher  $l$  terms give smaller contributions, and in particular ensures that the dipole term gives no contribution. Using the monopole (and potentially quadrupole) approximation for distant particle collections therefore gives good accuracy at substantially reduced computational cost.

N-body simulations have a long history, first being employed in a very creative way by Holmberg (1941). He noted that the intensity of light also decreased like  $1/r^2$  and used a setup of 37 light bulbs and photometers to calculate the dynamics of two interacting nebulae. This was, of course, before powerful computers were invented. Computer simulations were first applied to a cosmological setting by Peebles (1970).

This work used a simulation of 300 particles to show that gravitational interactions alone could be responsible for generating a galaxy distribution similar to that of the Coma cluster.

While the first simulations traced the evolution of hundreds of particles, current simulations have pushed the number to the  $10^{10}$  level, allowing us to accurately resolve both the large distribution of halos and their inner structure. Examples of the large and small-scale density fields from high resolution simulations can be seen in Figures 3.1 and 3.2. Figure 3.1 shows the  $z = 0$  output of the Millennium simulation, a  $500h^{-1}\text{Mpc}$  simulations involving  $10^{10}$  dark matter particles Springel et al. (2005). Such a large volume was needed in order to resolve the progenitors to high redshift quasars, rare objects that form out of many- $\sigma$  perturbations of the density field with  $z = 6$  masses around  $\sim 10^{12}h^{-1}M_{\odot}$  and comoving space density  $\sim 10^{-9}h^3\text{Mpc}^{-3}$ . Figure 3.2, on the other hand, shows a simulation that tracked the evolution of a single, Milky Way sized halo with as much resolution as possible. The high resolution was needed to trace the evolution of substructure so that estimates of the dark matter annihilation rates in our galaxy can be made (Diemand et al., 2007). Here, a single halo with about 10,000 subhalos is simulated with more than  $2 \times 10^8$  particles. These two simulations represent two very different ways to use modern techniques to explore the dynamical ranges made available by very large N-body simulations. The simulations for this thesis will concentrate more on an intermediate range, resolving halos with  $10^3 - 10^6$  particles in boxes of moderate size ( $50 - 250h^{-1}\text{Mpc}$ ). Using such simulations we will be able to study many of the structural properties of the more common massive also with  $z = 0$  masses  $\sim 10^{14}h^{-1}M_{\odot}$ .

As an additional note, I would also like to point out that cosmological N-body simulations differ from many other types of astrophysical N-body simulations in their use of periodic boundary conditions in an attempt to simulate an infinite universe (or

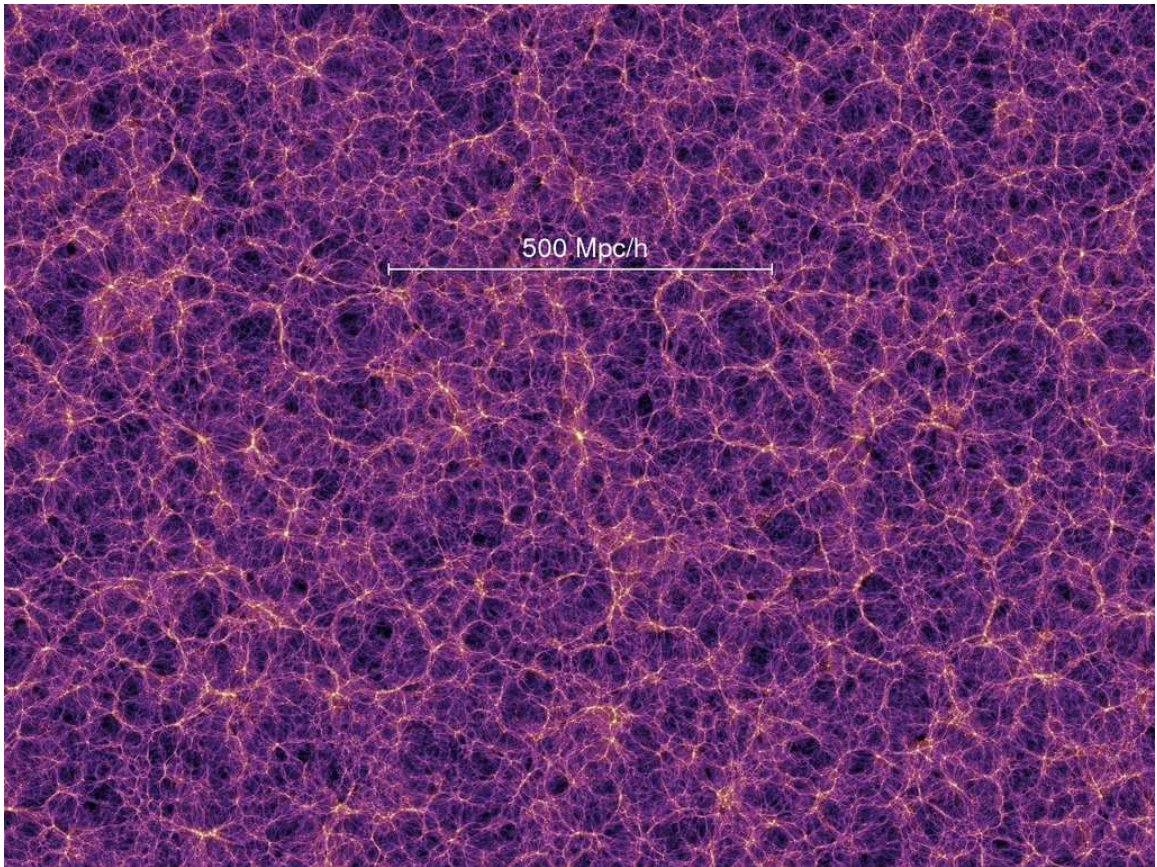


**Figure 3.1.** The dark matter density field from the Millennium Simulation, a  $10^{10}$  particle N-Body simulation, the largest to date. *Image Credit:* Springel et al. (2005)





**Figure 3.2.** The dark matter distribution around a Milky Way-sized halo with  $M_{200} = 1.8 \times 10^{12} M_{\odot}$  and over 10,000 identified subhalos. The image size is  $800 \times 600 h^{-1} \text{kpc}$ . *Image Credit:* Diemand et al. (2007).

at least one that is many times larger than the computational volume). While this is a standard process for many types of simulations, the cosmological context does create some additional complications. In particular, using the standard method of generating initial conditions discussed here, if the simulation box size is too small, perturbations of the scale of the box or larger are ignored, causing the simulation to model a slightly different power spectrum than intended. It is possible for this to affect the mass function at the few percent level (Bagla & Ray, 2005). In practice, the simulation volume should always have box length  $l \gtrsim 40 h^{-1}\text{Mpc}$  when simulating a region to  $z = 0$ . However, new methods of generating initial conditions are being developed that have the potential to correct this problem. Such methods are beyond the scope of this thesis, and the reader should see Pen (1997) and Sirko (2005) for a discussion.

### 3.1 N-body Techniques and Algorithms

In this section we discuss many aspects of the algorithms used in Gadget to speed up and increase the accuracy of force calculations. In particular, we will address force softening, time integration, and the Tree and PM methods for avoiding costly  $1/r^2$  calculations when computing the forces acting on particles.

#### 3.1.1 Force Softening

The first complication that needs to be addressed when implementing a N-body simulation is the effect that the discreteness has on a particle distribution. Because we model the density field as point-particles, it is possible for hard collisions to occur when two particles pass extremely close to each other, an encounter that results in unreasonably large forces and transfers of energy. Such a process is known as numerical relaxation and will artificially eject particles out of high density regions. The time-scale for the relaxation of such a system is given by Binney & Tremaine

(1987),

$$t_{relax} = t_{cross} \frac{N}{8 \ln(R/b_{min})}. \quad (3.3)$$

Here,  $t_{cross}$  and  $R$  are the crossing time and size of the system, while  $b_{min} = GM/v^2$  is the gravitational radius of the system. This can be combatted rather inefficiently by increasing the mass resolution, since  $t_{relax} \propto N$ . A better solution is to use a softened potential, such as the spline potential (Monaghan & Lattanzio, 1985; Springel et al., 2001b) to determine the forces on particle  $i$ :

$$\Phi_i = -G \sum_j m_j g(|\mathbf{x}_j - \mathbf{x}_i|) \quad (3.4)$$

$$g(r) = -\frac{1}{\epsilon} \begin{cases} \frac{16}{3} \left(\frac{r}{\epsilon}\right)^2 - \frac{48}{5} \left(\frac{r}{\epsilon}\right)^4 + \frac{32}{5} \left(\frac{r}{\epsilon}\right)^5 - \frac{14}{5} & 0 \leq \left(\frac{r}{\epsilon}\right) < \frac{1}{2} \\ \frac{\epsilon}{15r} + \frac{32}{3} \left(\frac{r}{\epsilon}\right)^2 - 16 \left(\frac{r}{\epsilon}\right)^3 + \frac{48}{5} \left(\frac{r}{\epsilon}\right)^4 & \\ -\frac{32}{15} \left(\frac{r}{\epsilon}\right)^4 - \frac{32}{15} \left(\frac{r}{\epsilon}\right)^5 - \frac{16}{5} & \frac{1}{2} \leq \left(\frac{r}{\epsilon}\right) < 1 \\ -\frac{\epsilon}{r} & \left(\frac{r}{\epsilon}\right) \geq 1 \end{cases}$$

Here,  $\epsilon$  is a softening length that prevents hard encounters whenever  $|\mathbf{x}_i - \mathbf{x}_j| < \epsilon$  but does not affect the potential at larger distances. While particles can still pass infinitely close to each other, the gravitational potential cannot arbitrarily large. The consequence of this modification is that you cannot trust the simulation results at scales below the softening length (Power et al., 2003). While there is no universal “best” value for  $\epsilon$ , the softening does set a gravitational acceleration threshold above which the simulation will not be resolved. Overdense regions should be converged as long as they obey the constraint

$$a(r) = GM(r)/r^2 \lesssim a_\epsilon = V_{200}^2/\epsilon, \quad (3.5)$$

where  $V_{200}$  is the gravitational velocity of the halo. At higher densities, the softening will cause structures to be somewhat washed-out. The softening length cannot be arbitrarily lowered beyond the mass resolution for two particles in a binary orbit, however, and can be best set using the minimum number of particles with which you want to resolve a single halo.



### 3.1.2 Time Integration

When simulating cosmological scales, it is standard to use Newtonian dynamics in a comoving reference. Particle positions are determined by calculating the Newtonian forces acting on the distribution and advancing the particles by some timestep,  $\Delta t$ . Newton's laws in comoving coordinates are given by

$$\frac{d\mathbf{x}}{dt} = \frac{1}{a}\mathbf{v} \quad (3.6)$$

$$\frac{d\mathbf{v}}{dt} + H\mathbf{v} = \mathbf{g} \quad (3.7)$$

$$\nabla \cdot \mathbf{g} = -4\pi G a [\rho(\mathbf{x}, t) - \bar{\rho}(t)]. \quad (3.8)$$

In this frame, nuances like the Hubble drag are automatically accounted for. Cosmological information, such as  $\Omega$ , is used to determine the evolution of the scale factor,  $a$ , independently of the particle dynamics.

In order to accurately integrate equations (3.6) - (3.8) Gadget uses a symplectic leapfrog integrator known as the *kick-drift-kick* (KDK) scheme. This scheme preserves the Hamiltonian of the system. Noting that the Hamiltonian can be divided into kinetic and potential contributions, we define the *kick* and *drift* operations to update each part of the Hamiltonian separately (Quinn et al., 1997):

$$D_t(\Delta t) : \begin{cases} \mathbf{p}_i \mapsto \mathbf{p}_i \\ \mathbf{x}_i \mapsto \mathbf{x}_i + \frac{\mathbf{p}_i}{m_i} \int_t^{t+\Delta t} \frac{dt}{a^2} \end{cases} \quad (3.9)$$

$$K_t(\Delta t) : \begin{cases} \mathbf{x}_i \mapsto \mathbf{x}_i \\ \mathbf{p}_i \mapsto \mathbf{p}_i + \mathbf{f}_i \int_t^{t+\Delta t} \frac{dt}{a} \end{cases} \quad (3.10)$$

where the force acting on particle  $i$  is given by  $\mathbf{f}_i = -\sum_j m_i m_j \frac{\partial \phi(\mathbf{x}_{ij})}{\partial \mathbf{x}_i}$ . Whenever a particle is kicked, the full potential of the particle must be calculated while this information is not necessary for a drift. The actual time integration is done using a Runge-Kutta method. When advancing a particle by a time step  $\Delta t$  we advance the position and momentum of the particle through the KDK scheme using the time

evolution operator

$$U(\Delta t) = K \left( \frac{\Delta t}{2} \right) D(\Delta t) K \left( \frac{\Delta t}{2} \right). \quad (3.11)$$

For such an integration scheme, errors in the Hamiltonian will typically grow like  $\mathcal{O}(\Delta t^2)$  (Saha & Tremaine, 1992) and tests of integrating circular orbits show a surprisingly higher degree of stability than a similar DKD (or a non-symmetric KD or DK) scheme.

Because local densities for particles at any given time in a cosmological simulations particles will vary widely, computations can be substantially sped by the use of adaptive time-steps (Duncan et al., 1998). The size of a drift time step is set by  $\Delta t_i \propto 1/\sqrt{|\mathbf{a}_i|}$ , where  $\mathbf{a}_i$  is the acceleration of particle  $i$  at the preceding time step. In this way, particles in higher density regions (where trajectories will be much more chaotic) are integrated more accurately than those in lower density regions. This works well with the KDK scheme because kicks for particles with larger timesteps will be done simultaneously with the particles having shorter timesteps, minimizing the number of times the full potential field needs to be calculated. This is not the case for the DKD scheme.

### 3.1.3 The Tree Method

The tree algorithm is a method for speeding up the force calculation by using a direct summation for neighboring particles and opting for a multipole expansion when determining the force contribution from more distant regions. Particles are arranged into hierarchical cells by subdividing space into cubes and storing the total mass content and center of mass (i.e., the information needed for a monopole approximation) for each cube. As an example of this process, consider the 2-dimensional representation in the top-right of figure 3.3. Space is first divided into 4 equal squares which we now refer to as cells. The total mass and center of mass of all particles in each cell is stored in a tree and the cells are then subdivided into 4 new cells and so on until the

smallest cells contains only a single particle (of course, for a 3 dimensional tree each subdivision creates 8 new cells). Now, when calculating the force on a particle, you “walk” the tree instead of looping through all other particles. After picking a particle and specifying an opening criteria, consider with the topmost cell. If the cell satisfies the opening criteria (which the top-most cell, containing all particles, always will) the cell is “opened” and you apply this criteria to each of the new, smaller cells. Once you reach a cell that fails the opening criteria, you calculate that cells contribution to the potential of particle  $i$  using the monopole expansion,

$$\phi_{i,cell} = \frac{GM_{cell}m_i}{r_{i,cell}} \quad (3.12)$$

In principle, you can achieve higher accuracy for a more stringent opening criteria by storing higher moments of the gravitational field, but in practice there is no improvement in speed.

The opening criteria is determined by specifying the parameter  $\alpha$  such that a cell is open whenever

$$\frac{GM}{r^2} \left(\frac{l}{r}\right)^2 > \alpha|\mathbf{a}| \quad (3.13)$$

Here,  $l$  is the side length of the cell being considered,  $r$  the distance from the particle to the center of mass of the cell,  $M$  the mass inside the cell, and  $\mathbf{a}$  the acceleration of the particle at the last timestep. The form of this criteria is motivated by geometry. The magnitude of the acceleration,  $|\mathbf{a}|$  is dimensionally equivalent to  $GM_{cell}/r_{i,cell}^2$ , which we can think of as the contribution of the cell to the particles acceleration. Using this substitution and the small angle approximation, equation 3.13 can be reduced to

$$\sqrt{\alpha} < \frac{l}{r} \approx \theta \quad (3.14)$$

where  $\theta$  is subtended angle between the particle and the sides of the cell. Thus,  $\alpha$  is equivalent to specifying a critical angle, above which a cell will be opened. Using this scheme, massive cells at short distances are preferentially opened and  $\alpha$  can be tuned

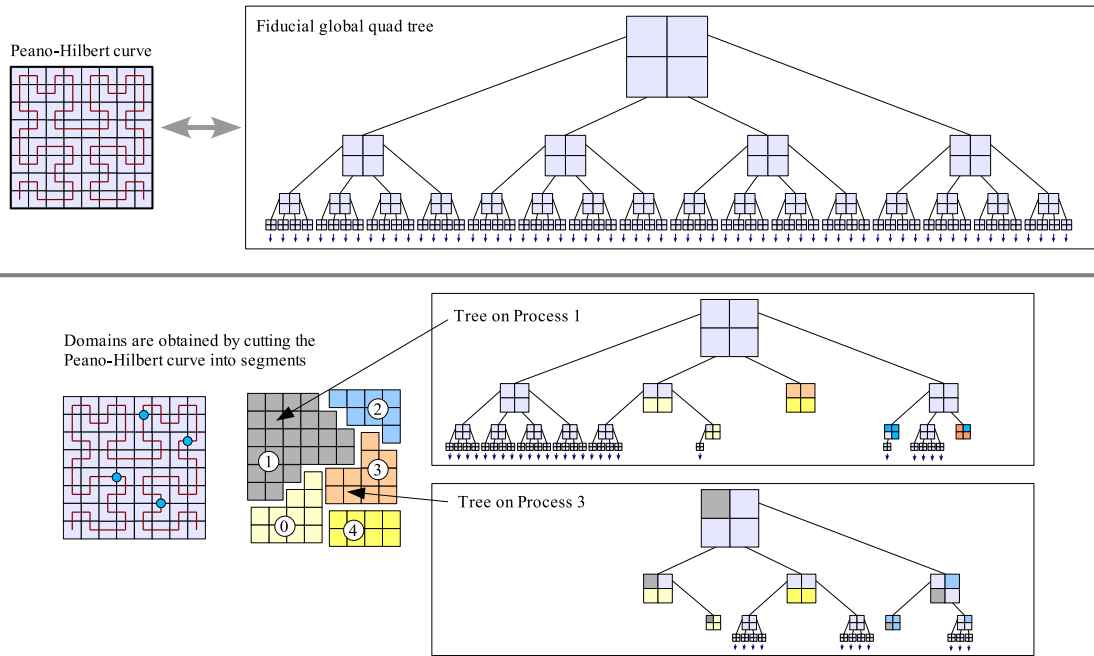


**Figure 3.3.** *Top Panel:* The decomposition of a 2-dimensional domain into squares for the construction of a force tree. *Bottom Panel:* How the tree in the top panel is split during parallelization. The left shows the space filling Peano-Hilbert curve with the o's along the curve representing the locations where the curve is cut for decomposition purposes. The boxes on the right show the tree information stored on two specific processors. *Image Credit:* Springel (2005).

to give an optimal speed/accuracy ratio. Because a  $1/r^2$  computation is not done for every pair of particles in this scheme, the tree algorithm scales like  $\mathcal{O}(N \log N)$ . As discussed in section 3.2, this force-tree is also extremely conducive to parallelization because each processor will not need to store the entire force tree.

### 3.1.4 The PM and TreePM methods

An alternative method for force computation is the Particle-Mesh (PM) method. In this method, computations are done in Fourier space, utilizing the very efficient parallel FFT codes that are publicly available. First, the density field is projected onto a grid, giving us the density field at a set of discrete points,  $\rho(\mathbf{x}_{i,j,k})$ . The discrete Fourier Transform of this field,  $\rho_{\mathbf{k}}$ , is then calculated, which can be used to easily solve for the Fourier transform of the potential,

$$\phi_{\mathbf{k}} = -4\pi G a^2 \frac{\rho_{\mathbf{k}}}{|\mathbf{k}|^2}. \quad (3.15)$$

An Inverse Fourier Transform is then calculated to return  $\phi(\mathbf{x})$  on a grid, which can be interpolated to give the potential for every simulation particle. This method has several advantages — it is very fast and the nature of the Fourier Transform automatically assumes periodic boundary conditions, something that is much more difficult to implement with a tree method. However, the accuracy of the potential is limited by the size of the grid used, which is in turn limited by the mean interparticle spacing. While the tree method is adaptive in that it does more  $1/r^2$  calculations for highly clustered particles, the PM method does the same calculation for every particle, regardless of whether the particle is in a void or a cluster.

In order to utilize both the adaptability of the tree and speed of the PM methods, GADGET-2 employs a hybrid Tree-PM approach by splitting  $\phi_{\mathbf{k}}$  into long and short-range components,  $\phi_{\mathbf{k}} = \phi_{\mathbf{k}}^{\text{long}} + \phi_{\mathbf{k}}^{\text{short}}$ . The long range contribution is calculated using the PM method, typically using a grid with resolution 4 times the interparticle spacing. The short range contribution, on the other hand, is calculated using a tree

walk. Splitting the potential this way, we are able to rapidly calculate the long range contribution using the PM method but the use of the tree method for shorter ranges, giving a substantial improvement in accuracy by allowing deep tree-walks for particles in highly clustered regions. Other hybridizations of PM and direct summation methods are possible, such as the P<sup>3</sup>M method. See the review of Bertschinger (1998) for further details.

### 3.2 Parallelization

While the algorithms discussed above substantially speed the computation, simulations still scale roughly as  $\mathcal{O}(N \log N)$ , and something must still be done to continue pushing to higher and higher  $N$ . The amount of memory in a computer still places an additional limit simulation size. At any given time during the simulation at least the output data, consisting of the positions and velocities of each particle as well as index identifying the particle, must be stored in memory. This adds up to 32 bytes of data per particle. For a  $10^{10}$  particle simulation, that translates to 298 Gigabytes *just to read in the data*. Even the more modest simulations presented here, with  $256^3$  particles, use roughly half a gigabyte of memory to store all data, leaving little room for additional calculations (such as the density fields, trees, particle accelerations, ...). On today's computers that have 1 – 2 gigabytes of addressable memory per processor (although 4 – 8 gigs is becoming more common thanks to 64-bit processors), this places a heavy constraint. Not only does parallel computing allow simulations to run faster by performing multiple calculations simultaneously, for the most advanced simulations parallelization is needed to be able to run the simulation at all.

Because N-body simulations consist of particles distributed in real space, parallelization can be done in a relatively straightforward manner. Space is divided into  $N_p$  domains where  $N_p$  is equal the number of available processors. The computational volume is thus decomposed and each processor then works on one (or more)

of the domains, communicating with other processors only when it needs to transfer tree or density grid information. The primary bottleneck in this process occurs when one processor needs to communicate with another. In order to minimize the number of necessary communications, GADGET does the domain decomposition using a Peano-Hilbert space filling curve. If a  $d$ -dimensional cubic region is divided into  $2^{md}$  sub-cubes, a Peano-Hilbert curve of degree  $m$  will pass through every sub-cube with the remarkable property that, if the curve is cut at any point, the cubes are divided into regions with a relatively low area/volume ratio. Examples of Peano-Hilbert curves in 2 and 3 dimensions are shown in Figure 3.4.

To do the domain decomposition, all particles are matched to a point along a curve with degree  $m$ , creating an ordered series of cubes of length  $1/2^m$  times the simulation box length. The actual decomposition is then done by cutting the curve into  $N_p$  segments such that each segment contains roughly an equal number of particles. The particles on each segment are then mapped to a specific processor. Such a scheme allows the domain decomposition to match up with the specific leaves of the force-tree calculated earlier, as demonstrated in the bottom right of Figure 3.3. Each processor stores the full tree for all particles residing in its computational domain as well as the top-most level of the trees for particles on all other processors. This is demonstrated schematically in the bottom left Figure 3.3. In this way, during the tree-walk for a particular particle, much of the information concerning distant particle distributions is readily accessible without communicating with other processors.

### 3.3 Generating Initial Conditions

Initial conditions for cosmological N-body simulations are generated using an input power spectrum and the Zel'dovich approximation. We begin with a primordial power-law power spectrum,  $P_{prim}(k)$ , the kind expected to be generated by inflation. In the pre-recombination epoch (the first  $\sim 300,000$  years), photons have an

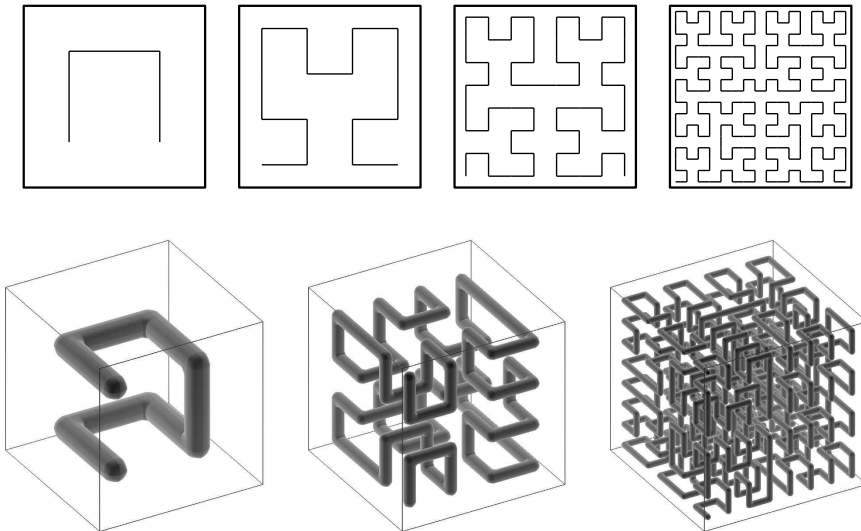


**Figure 3.4.** Examples of Peano-Hilbert curves of various degrees in two and three dimensions. *Image Credit:* Springel (2005)

extremely short mean free path due to the ionization of the baryons. This causes a coupling of photons, dark matter, and baryons that will alter the power spectrum. After recombination, photons and baryons become uncoupled, and perturbations are allowed to grow as discussed in section 2.2. The “processed” power spectrum after recombination can then be given by

$$P(k) = Ak^n |T(k)|^2. \quad (3.16)$$

Here,  $Ak^n = P_{prim}(k)$ , the primordial power spectrum (frequently measured from the CMB,  $A = \sigma_8 \Omega_m^{0.6}$ ), and  $T(k)$  is the transfer function. This function contains information on a wealth of relevant physical processes that affect the growth of inhomogeneities through recombination on both sub and super-horizon scales during the radiation and matter dominated epochs. The full transfer function is highly complex and depends very sensitively on the cosmology. It is generally calculated using one of a number of publicly available codes, the most popular of which is CMBFAST (Seljak & Zaldarriaga, 1996).

Once the power spectrum has been evolved to the starting redshift of the simu-



lation, the Zel'dovich approximation is used to generate a particle distribution with the desired spectrum (Zel'Dovich, 1970; Doroshkevich et al., 1980). First, an initial particle distribution with a constant potential is generated. This can either be a regular grid, or a random glass distribution. A glass is generated by laying down particles with a uniform random distribution and using this as the initial condition for an N-body simulation run with the sign of  $G$ , the gravitational constant, reversed (so that gravity repels instead of attracts) until the particles reach a stable configuration. Now, we make the assumption that once a particle is given an initial displacement, determined by some time-independent displacement field  $\mathbf{f}(\mathbf{x})$ , it will continue to evolve (during the era of linear perturbations) in the same direction, similar to the effects of the Hubble flow. This displacement field dictates the distribution of the perturbation field,

$$\delta(\mathbf{x}) = -D(a)\nabla \cdot \mathbf{f}(\mathbf{x}). \quad (3.17)$$

Since the expectation value for  $\delta_k$  is given by the power spectrum, the displacement field,  $\mathbf{f}(\mathbf{x})$ , can be readily calculated from equation (3.17) by working in Fourier space. Once the initial displacement field has been calculated, the actual position and velocity displacement are then given by  $\mathbf{f}(\mathbf{x})$  and the growth function,  $D(t)$ ,

$$\mathbf{x}(t) = \mathbf{x}_0 + D(t)\mathbf{f}(\mathbf{x}_0) \quad (3.18)$$

$$\mathbf{v}(t) = a(t)\frac{dD(t)}{dt}\mathbf{f}(\mathbf{x}_0) \quad (3.19)$$

where  $\mathbf{x}_0$  represents the unperturbed particle position. Once these displacements have been made, the particle distribution for the starting redshift of the simulation has been calculated and the simulation is ready to begin.

### 3.4 Finding Dark Matter Halos

Since this dissertation concentrates on the properties of dark matter halos it is necessary to discuss the algorithm for extracting halos from a simulation. This process

of groupfinding is less of a science and more of an art. Indeed, because of continuous mass accretion, even the question of exactly how one defines a halo and its boundary is more subtle than it first appears. Two standard methods have emerged as methods for identifying and defining halos, friends-of-friends (FOF) and spherical overdensity (SO).

The FOF, or percolation, method works by identifying particles close to each other in real space. Starting with a single particle and a linking length,  $l$ , it is grouped with all particles that have separation  $r < l$ , i.e., the “neighbors” or “friends” of this particle. This procedure is repeated on all of the friends, which are in turn added to the original group until all other simulation particles have  $r > l$  for every member of the group. This collection of particles is known as the FOF halo. The center of the halo is then typically chosen to coincide with the particle in the group with the highest binding energy. The linking length,  $l$ , is usually set to be some parameter  $b$  times the mean interparticle spacing. Using this definition,  $b$  selects particles within a non-isodensity contour with threshold independent of the simulation mass resolution. In this thesis, we normally take  $b = 0.15$  (which selects objects with mean density roughly  $296\bar{\rho} = 89\rho_{crit}$  at  $a = 1$  in a concordance model universe), although larger values of 0.164 and 0.2 are also common. The selection of  $b$  is important because a value that is too low will exclude many gravitationally bound objects, while a value that is too large will regularly connect distinct halos with kinematically distinct populations.

The SO method, in contrast, requires that halo boundaries be spherical and works by identifying peaks in the density field. First the density field is smoothed and the largest peak identified. Working outward, the closest particles are added until the mean spherical overdensity of the object drops below some threshold value, typically  $200\rho_{crit}$ ,  $180\bar{\rho}$ , or  $\Delta(z)\rho_{crit}$ , where  $\Delta$  is a value that depends on the redshift motivated by the spherical collapse model (Eke et al., 1996). This method, however, also has

difficulty in dealing with mergers, in particular the question of do you allow halos to overlap (i.e., can a particle exist in more than one halo)? Unfortunately, there is no standard convention and no particularly well motivated method for dealing with these issues. In practice, with the exception of merging halos, both the FOF and SO groupfinders are robust enough that they pick out nearly identical halo distributions.

Along with multiple methods for finding halos, there are also a number of mass conventions. Starting with the FOF method, the natural mass value is  $M_{FOF}$ , the mass of all particles in the FOF group. Using either method, spherical overdensity values, such as  $M_{200}$ , the mass of a spherical object with overdensity  $200\rho_{crit}$  can be calculated. For the SO group finder, this number naturally falls out of the groupfinding process. For the FOF groupfinder, however, one must do some post-processing and measure the spherical overdensity around the center of the FOF halo. As mentioned above, there are a number of different overdensity conventions for defining the mass of a halo, such as  $M_{200}$ ,  $M_{vir}$  (defined by the threshold  $\Delta(z)\rho_{crit}$ ) and  $M_{180,b}$ . For this thesis we primarily use  $M_{200}$ . See chapter 6 for a more through discussion of these mass definitions.

### 3.4.1 Subhalos

As noted in section 2.3.1, halo growth in a CDM universe is characterized by hierarchical accretion. When a small halo merges with a larger halo, the accreted halo is disrupted by tidal forces and close encounters with the core of the host halo, but is typically not destroyed entirely. The stripping processes are proficient at removing the more loosely-bound outer particles of the accreted halo but generally leave the tightly bound core in tact. This remnant then orbits the main halo as a highly correlated lump of particles with high density and low velocity dispersion and is known as a subhalo.

While finding dark matter halos is a somewhat artful process, locating their sub-

halos is even more so. The community has yet to reach a consensus with regards to standard methods or procedures, and a whole host of algorithms, range from a hierarchical FOF to density-peak finding within a larger halo, have been developed. The algorithm used in this work is known as SUBFIND (Springel et al., 2001a). The routine locates a FOF halo and finds groups of bound material surrounding a density peak within the halo. The algorithm proceeds as follows. First, a local density estimate is made for every FOF particle in the halo. Working in order of decreasing density, we consider the  $N_{ngb}$  particles closest to particle  $i$ . If particle  $j$ , one of the surrounding particles, has a higher local density than  $i$  does,  $i$  is added to  $j$ 's group. If there are no higher-density particles around  $i$ , then  $i$  itself is considered to be a new subgroup (in this way the algorithm works so that  $j$  will necessarily be a part of a group if  $j$  has a higher density than  $i$ ). If there are two or more particles with higher densities than the two particles with the highest densities,  $j$  and  $k$ , are considered. If  $j$  and  $k$  are in the same group,  $i$  is added to that group. If they are in different groups, a new group is created by joining the groups containing  $j$  and  $k$  and adding particle  $i$ , which we now call a saddle point. The two original groups, however, are not removed.

At this point, the algorithm has generated a list of subgroups by looking for peaks and saddle points in the density field. In order for these to be considered subhalo we now account for energy considerations. The potential energy for all particles in the subgroup is calculated, and any particle with a higher kinetic energy (relative to the center of mass velocity of the subgroup) is removed from the group. The process is then iterated until every particle in the subgroup is bound, and the resulting distribution is considered to be a subhalo.

When dealing with saddle points, some extra care is taken. If two groups were joined, the two smaller (unjoined) groups are considered first, and only if one of those groups becomes entirely unbound do we consider the union of the groups. In particular, this is necessary because SUBFIND treats the background host halo no

differently from any of the subhalos. If the binding criteria of the smaller halos was not considered first, the algorithm would tend to identify only a single halo — that of the material bound to the FOF group. In this way it is actually possible to have a full hierarchy or structure — subhalos can have their own subhalos and so on.

It is also important to note that in some situations, such as the far future, the FOF algorithm will include unbound material. When `SUBFIND` is run on such a halo it makes sure that each identified subhalo is bound, but there is no guarantee that each subhalo is genuinely bound to the host halo and is not itself a distinct halo. It is therefore necessary to check all subhalos identified by `SUBFIND` to make sure that they are bound to the host halo in such situations.

## CHAPTER 4

# Asymptotic Halo Structure

As discussed in the introductory chapters, the past several years have witnessed an impressive solidification of our estimates for the basic cosmological parameters. In this newly consolidated cosmological model, the most unexpected property is the large (apparent) energy density in the form of dark vacuum energy. The substantial value of  $\Omega_{v,0} = 0.7$  produces a correspondingly large effect on past cosmological evolution. In particular, the age of the universe is somewhat longer than in a flat cosmology with no vacuum energy and more consistent with other age indicators (e.g., Carroll et al., 1992). But, by far, the most striking consequence of this vacuum energy lies in our cosmological future.

If the universe is already starting to accelerate, as indicated by the observationally implied value  $\Omega_{v,0} = 0.7$ , then structure formation is virtually finished. In the relatively near future, the universe will approach a state of exponential expansion and growing cosmological perturbations will freeze out on all scales. Existing structures will grow isolated. In the face of such desolation, we would like to know more quantitatively the conditions required for the formation (collapse) of future cosmological structures and the conditions required for small bodies to remain bound to existing structures. We would also like to know the asymptotic form of the existing cosmological structures, in particular the dark matter halos. By answering these questions, we can determine how much structure formation remains to occur in the future of our universe.

Given the relatively well constrained parameters of our universe, the future evolution of cosmological structure can now be predicted with some confidence for a variety of dark energy models. Indeed, several recent papers have begun to explore this issue. Possible future effects of vacuum energy density were outlined in a recent review of our cosmic future (Adams & Laughlin, 1997, hereafter AL97). As the universe accelerates, currently visible galaxies are redshifted out of view and will become inaccessible to future astronomers (Loeb, 2002). Simulations of future structure formation have been done for the case of a cosmological constant with a focus on our local portion of the universe (Nagamine & Loeb, 2003). Similar issues have been explored semi-analytically, including basic effects of quintessence (Chiueh & He, 2002; Gudmundsson & Björnsson, 2002). A comprehensive list of papers related to the future evolution of the universe is compiled in Cirkovic (2003).

In this chapter, we consider the future evolution of structure formation with a constant density of dark vacuum energy. We extend previous work by deriving analytic estimates for the conditions required for the collapse of structures, and by analyzing the results from a suite of numerical simulations of future structure formation. The future evolution of cosmic structure can be viewed in two related ways. The traditional approach considers whether or not a given region of the universe with overdensity  $\delta_0 \equiv (\rho - \langle \rho \rangle) / \langle \rho \rangle$  will collapse. Given the strong suppression of future structure formation, however, relatively little will happen in terms of new formation. A related question is to ask whether or not test bodies will remain bound to existing structures. This issue operates on a wide range of spatial and mass scales: Will the local group remain bound to the Virgo cluster? Will a satellite dwarf galaxy remain bound to the Milky Way? What bodies would remain bound to an isolated star in the face of accelerated expansion? This chapter develops both approaches — analytically in §4.1 and numerically in §4.2 — and elucidates the relationship between them. Our numerical simulations also show that the density profiles of dark matter

halos approach a nearly universal form. Every dark matter halo grows asymptotically isolated and becomes the center of its own island universe; each of these regions of space-time then approaches a universal geometry. In §4.3, we determine the sphere of influence of existing structures and find the future time at which they grow cosmologically isolated. Next, we consider the implications of cosmic acceleration for the background radiation fields, suppression of particle annihilation, and the long term geometry of space-time. Because the equation of state of the dark vacuum energy is not completely determined, we generalize these results (in Appendix A) to consider dark energy that varies with time (equivalently, the scale factor).

## 4.1 Analytic Descriptions Of Structure Formation

Before performing detailed numerical simulations of future structure formation, it is useful to develop simple analytical estimates. Such results have been developed previously to account for past structure formation in an accelerating universe (see especially Lokas & Hoffman, 2001). While most past work has emphasized the evolution of structure up to the present epoch, we focus here on its evolution into the future. Throughout this treatment, we assume a spatially flat universe, which at the present epoch has  $\Omega_{m,0} = 0.3$  and  $\Omega_{v,0} = 0.7$  ( $\Omega_{m,0} + \Omega_{v,0} = 1$ ). In the future, the values of  $\Omega_m$  and  $\Omega_v$  vary, but their sum continues to equal unity.

### 4.1.1 Collapse of overdense regions

The evolution of a given region of the universe is described by an energy equation. For a spherical patch of physical size  $r$ , this energy equation can be written in the form

$$\frac{1}{2}\dot{r}^2 - \frac{GM}{r} - \frac{1}{2}H^2r^2\Omega_{v,0} = E, \quad (4.1)$$

where the energy  $E$  is given by

$$E = \frac{1}{2}H_0^2r_0^2\left[1 - \Omega_{m,0}(1 + \delta_0) - \Omega_{v,0}\right]. \quad (4.2)$$



This set of equations implicitly assumes that  $\dot{r} = H_0 r_0$ , i.e., that the particles are traveling along with the unperturbed Hubble flow at the present epoch. Later in this section, we generalize this analysis to consider the case in which particles have already slowed down relative to the Hubble flow due to the past action of gravity.

If we define the dimensionless variable  $\xi \equiv r/r_0$  and the dimensionless time  $\tau \equiv H_0 t$ , then the energy equation can be rewritten in the simpler form

$$\left(\frac{d\xi}{d\tau}\right)^2 = 1 + \Omega_{m,0}\left(\frac{1}{\xi} - 1\right)(1 + \delta_0) + \Omega_{v,0}(\xi^2 - 1). \quad (4.3)$$

If a cosmological structure is slated to collapse in the future, then the effective velocity (the time derivative of  $\xi$ ) must change sign, which requires the right hand side of the above equation to vanish. This requirement results in a cubic equation of the form

$$\xi^3 + \left[\frac{1}{\Omega_{v,0}} - 1 - \frac{\Omega_{m,0}}{\Omega_{v,0}}(1 + \delta_0)\right]\xi + \frac{\Omega_{m,0}}{\Omega_{v,0}}(1 + \delta_0) = 0. \quad (4.4)$$

For a given (flat) cosmology (a given value of  $\Omega_{m,0}$ , which in turn specifies  $\Omega_{v,0} = 1 - \Omega_{m,0}$ ), and a given overdensity  $\delta_0$ , the cubic has three real roots if the following constraint is satisfied:

$$\left[\frac{\Omega_{m,0}}{\Omega_{v,0}}(1 + \delta_0)\right]^2 < \frac{4}{27}\left[1 + \frac{\Omega_{m,0}}{\Omega_{v,0}}(1 + \delta_0) - \frac{1}{\Omega_{v,0}}\right]^3. \quad (4.5)$$

The minimum overdensity  $\delta_0$  occurs when the above constraint is saturated (i.e., at equality). For a given value of  $\Omega_{m,0}$ , the vacuum energy density  $\Omega_{v,0} = 1 - \Omega_{m,0}$  is specified, and the equation has a given root. For the currently favored cosmological model with  $\Omega_{m,0} = 0.3$ , the root occurs for  $\delta_0 = 17.6$ .

#### 4.1.2 Criterion for being bound to existing structures

A related issue is to ask whether a small mass or test particle will be bound to currently existing cosmological structures. To carry out this calculation, we consider an existing object of mass  $M_{\text{obj}}$ , which could be (the dark matter halo encompassing) a galaxy or a cluster of galaxies. We then ask whether test particles — much smaller

structures exterior to the system — will be bound to  $M_{\text{obj}}$  or not. The test particles start with a radial distance  $r_0$  at the present epoch. For simplicity, we assume that the distance  $r_0$  is much larger than the size of the collapsed object so that the potential of a point mass provides a good approximation.

The calculation is analogous to that of the previous section, with the mass of the potentially collapsing system replaced by the mass  $M_{\text{obj}}$  of the pre-existing structure. The energy equation can again be written in non-dimensional form

$$\left(\frac{d\xi}{d\tau}\right)^2 = 1 + (\Omega_{\text{m},0} + \beta) \left[\frac{1}{\xi} - 1\right] + \Omega_{\text{v},0}(\xi^2 - 1), \quad (4.6)$$

where we have defined

$$\beta \equiv \frac{2GM_{\text{obj}}}{H_0^2 r_0^3}. \quad (4.7)$$

The parameter  $\beta$  thus measures the effective “strength” of the galaxy or cluster. The requirement that equation (4.6) have a turnaround point leads, as before, to a cubic constraint, which now takes the form

$$\Omega_{\text{v},0}\xi^3 - \beta\xi + (\Omega_{\text{m},0} + \beta) = 0, \quad (4.8)$$

which in turn requires

$$\beta^3 \geq \frac{27}{4}(\Omega_{\text{m},0} + \beta)^2 \Omega_{\text{v},0}. \quad (4.9)$$

The minimum value of the strength parameter occurs when the equality is saturated and we denote the corresponding value of  $\beta$  by  $\beta^*$ . Solving equation (4.9), we find the value  $\beta^* \approx 5.3$ . We can thus determine the condition that must be met in order for a test body to remain bound to an object of mass  $M_{\text{obj}}$ , i.e.,

$$2GM_{\text{obj}} \geq \beta^* H_0^2 r_0^3. \quad (4.10)$$

Inserting numerical values and scaling the result, we thus obtain the following criterion

$$\frac{M_{\text{obj}}}{10^{12} M_{\odot}} > 3 h_{70}^2 \left(\frac{r_0}{1 \text{ Mpc}}\right)^3, \quad (4.11)$$

where we have defined  $h_{70} \equiv H_0/(70 \text{ km s}^{-1} \text{ Mpc}^{-1})$ .

As an immediate application of the above result (equation [4.11]), we can determine whether or not the Milky Way (Local Group) will remain bound to the Virgo cluster in our cosmological future. The mass of Virgo is estimated to be  $M_{\text{Virgo}} = 5 \times 10^{13} - 10^{14} M_{\odot}$  and its current distance from the Milky Way is about  $r_0 = 16 \text{ Mpc}$  (e.g., Jacoby et al., 1992). The requirement specified by equation (4.11) is not met — the mass falls short by a factor of 100 — so that the Milky Way is not destined to be bound to Virgo. This result is verified by numerical simulations (see §4.1 and Nagamine & Loeb, 2003).

Equation (4.11) thus defines an effective sphere of influence for any given astronomical object — when considered as isolated in a background universe dominated by a cosmological constant. For our Milky Way galaxy, this sphere has radius  $r_0 \approx 0.7 \text{ Mpc}$ . For an isolated star (i.e., a free-floating star not associated with a galaxy), with typical stellar mass  $M_* = 0.5 M_{\odot}$ , the sphere of influence has size  $r_0 \approx 55 \text{ pc}$ . This size scale suggests that isolated binary star systems can remain safely bound. Although isolated pairs of galaxies can also remain gravitational bound, they live much closer to the brink of instability.

The above analysis finds the sphere of gravitational influence for test bodies that are moving along with the Hubble flow at the present epoch. However, due to the past evolution of the universe, bodies that are now outside galaxies (or clusters) can be slowed down relative to the Hubble flow due to the action of gravity in the past. In particular, the particles simulated in N-body simulations can be slowed down relative to the Hubble flow. To include this effect in the analysis, we modify equation (4.6) to take the new form

$$\left(\frac{d\xi}{d\tau}\right)^2 = A + (\Omega_{\text{m},0} + \beta)\left(\frac{1}{\xi} - 1\right) + \Omega_{\text{v},0}(\xi^2 - 1), \quad (4.12)$$

where the constant  $A$  represents the fact that the test particles have been slowed down relative to the Hubble flow (and rest of the quantities are the same as in equation

[4.6]). The value  $A = 1$  corresponds to particles moving with the Hubble flow, so that particles that have been slowed will have  $A < 1$ . The case  $A = 0$  provides a benchmark, where test bodies have zero velocity (are turning around) at the present epoch.

The requirement that equation (4.12) have a turnaround solution implies a modified form of equation (4.9), namely,

$$(\beta + 1 - A)^3 \geq \frac{27}{4} \Omega_{v,0} (\Omega_{m,0} + \beta)^2. \quad (4.13)$$

By solving the above cubic for a given  $A$  when the inequality is saturated, we find the root  $\beta^*(A)$  that can be used to define the sphere of influence of a given cluster or galaxy according to equation (4.10). For the benchmark case,  $A = 0$ , the root  $\beta^* \approx 1.1$ , and hence the effective sphere of influence is larger than the previous case by a factor of 1.7.

In the following section, we compare these analytic predictions to the results of numerical simulations. If we insert test bodies at the present epoch — at rest with respect to the Hubble flow — then the sphere of gravitational influence of existing structures is described accurately by equation (4.11). In addition, although mass particles that begin at rest (with respect to the Hubble flow) in the distant past are slowed down and have values  $A < 1$  at the present epoch, the prediction of equation (4.11) works respectably well (see the following section).

## 4.2 Numerical Simulations Of Structure Formation

To evaluate the analytic results of the previous section, particularly equation (4.11) defining the gravitational sphere for influence for an object of mass  $M$ , we have run a series of numerical simulations of the evolution of structure in a  $\Lambda$ -dominated universe into the future. All simulations were run using the GADGET code (Springel et al., 2001b)<sup>1</sup> on a parallel computer cluster at Michigan’s Center for Advanced

---

<sup>1</sup><http://www.MPA-Garching.MPG.DE/gadget/>

Computing. A flat  $\Lambda$ CDM model is assumed, with matter density  $\Omega_{m,0} = 0.3$ , power spectrum normalization  $\sigma_8 = 1.0$ , and  $h = 0.7$ , where the Hubble parameter  $H_0 = 100h \text{ km s}^{-1} \text{ Mpc}^{-1}$ . The simulations followed the evolution of a  $256.48 h^{-1} \text{ Mpc}$  region with  $128^3$  dark matter particles of mass  $6.70 \times 10^{11} h^{-1} M_\odot$ , starting from  $a = 0.0458$  ( $z = 20.8$ ), through the present, and forward to  $a = 100$ . A gravitational force softening of  $200h^{-1} \text{ kpc}$  (in physical units) was used throughout the computation.

In addition to the simulation described above, which was evolved to  $a=100$ , we performed a similar simulation that evolved the  $a = 1$  configuration forward with an added set of initially stationary test particles. In this run, 96 particles were placed in a spherically symmetric fashion around the centers of 19 dark matter halos. In each case, they were placed at rest on one of 12 concentric spheres centered at the most bound position of the selected group. This simulation was also evolved to  $a = 100$ .

The top two panels of Figure 4.1 show structure in a fixed comoving region  $128 h^{-1} \text{ Mpc}$  wide by  $25 h^{-1} \text{ Mpc}$  deep at (a) the present epoch and (b)  $a = 100$ . The large-scale pattern of the cosmic web is well established by  $a = 1$  and evolves little thereafter (as emphasized by Nagamine & Loeb, 2003). Clusters of fixed physical size shrink as  $1/a$  in the comoving frame, so the halo population effectively condenses into a sea of “droplets” embedded in the frozen linear modes that define the filaments, walls, and voids that characterize the cosmic structure today.

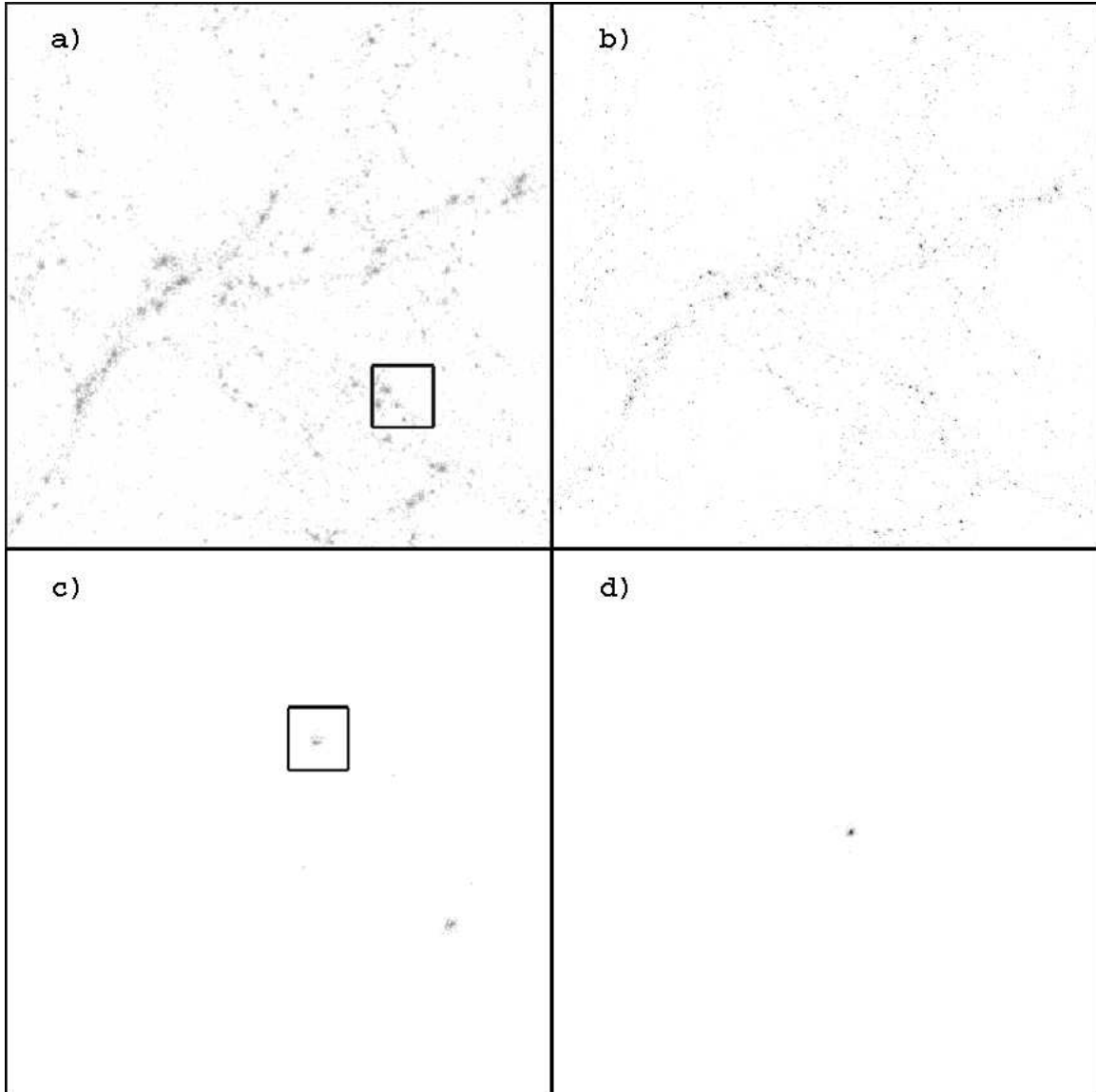
Panels (c) and (d) change perspective by showing how the physical region of panel (a) appears at  $a = 11$  and  $a = 100$ , respectively. The physical separation between bound structures grows exponentially in time during the deSitter expansion phase of the dark energy dominated era. The future is increasingly lonely.

Figure 4.1 depicts the structure of the universe in terms of co-moving coordinates and physical coordinates. In both cases, however, these points of view are those of an omniscient observer. Any real observer must look back in time and will see distant galaxies as they appeared before they left the observer-dependent event horizon. As

a result, cosmic structure will continue to appear clumpy on large scales. No galaxy will actually disappear completely, but rather will continue to redshift, much like if it were falling into a black hole. The time scale for this redshift effect is the e-folding time for the expansion (about 17 Gyr – see §4.3). Strictly speaking, future observers would still be able to see the Virgo cluster, although it would grow fainter and more redshifted. Our own bound region thus becomes isolated in the sense that one could not actually go to “nearby” regions such as Virgo, but we would still be able to “see” such regions because of the look-back effect. Notice, however, that the redshift effect is rather severe: Optical photons will be redshifted to become larger than the radius of Earth, e.g., in “only” about 30 e-foldings of the cosmic scale factor (about 500 Gyr from now).

To compute the size of a bound halo — its gravitational sphere of influence defined in the previous section — we identify the smallest radius at which the local mean radial velocity is significantly larger than zero. We measure such sizes using two different tracers: the simulation particles themselves or the test particles of the second simulation. Since the latter are embedded at rest at  $a = 1$ , their future evolution should better follow, within the limits provided by a monopole description of gravity, the prediction of equation (4.11) which assumes a pure, spherical Hubble flow.

Measurements of the gravitational sphere of influence are shown in Figure 4.2. Note that the relevant mass is the mass within the sphere of influence at the present epoch; this is typically a factor of 2–3 larger than  $M_{200}$ . The relation between this mass and its sphere of influence for test particles placed in the simulation at rest at  $a = 0$ , shown as stars, is in excellent agreement with the predictions of equation (4.11), shown as the lower line in the figure. Values for the simulation particles, shown as open squares, are slightly larger (by about 10%) because radial infall in the weakly non-linear regime reduces the kinetic energy associated with Hubble flow. These sizes are bounded from above by the modified relation, equation (4.12), with  $A = 0$ , shown



**Figure 4.1.** Evolution of structure in a  $\Lambda$ -dominated universe. Panels a) and b) show snapshots of a comoving region of the universe  $128 h^{-1}$  Mpc on a side and  $25 h^{-1}$  Mpc thick today ( $a = 1$ ) and at cosmic age 91.5 Gyr in the future ( $a = 100$ ), respectively. Panels c) and d) show regions of the same *physical* size as that shown in panel a) at epochs  $a = 11$  and  $a = 100$ , respectively. The box in panel a) locates the region shown in b), and the box in panel c) locates the region shown in d).

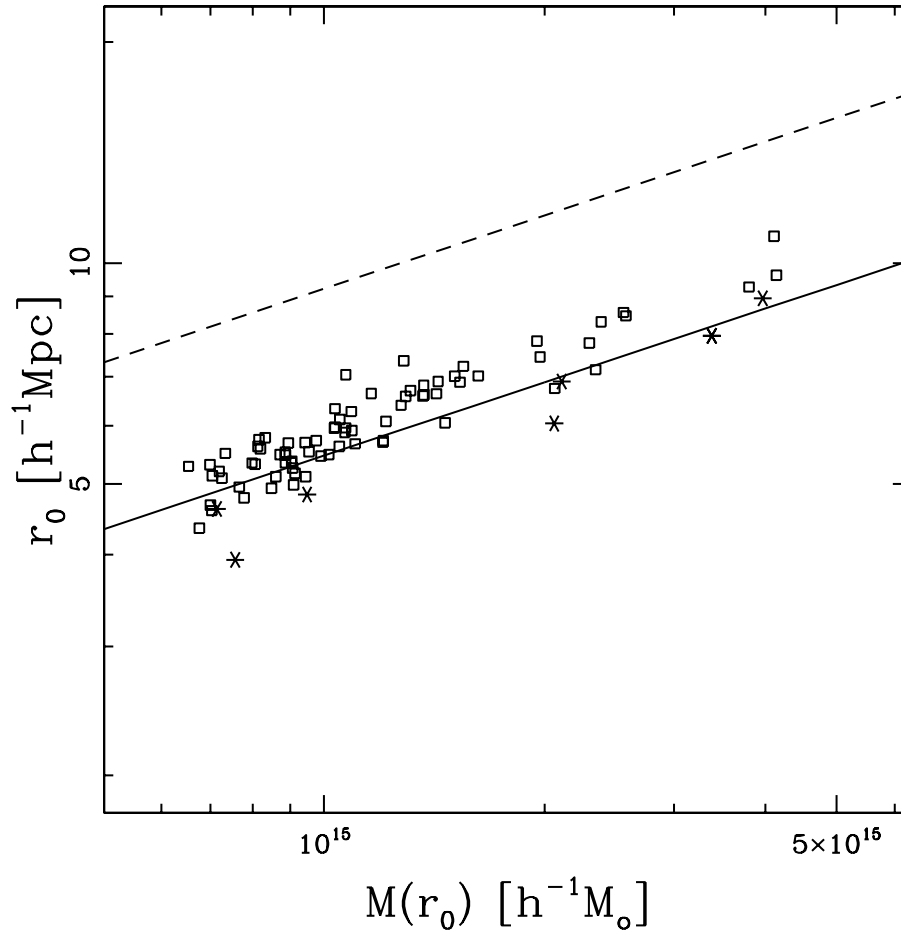


**Figure 4.2.** Gravitational sphere of influence of a cosmological object as a function of the mass enclosed within the sphere of influence at  $a=1$ . The lower solid line marks the analytic prediction for objects starting at rest with respect to the Hubble flow (equation [4.11]); the upper dashed line marks the analytic prediction for objects that are at rest relative to the cluster at the present epoch (i.e., objects that are marginally separated from the Hubble flow — see equation [4.12]). These analytic predictions are compared with simulations, both for cluster particles (open squares) and for the test particles placed in the simulation at rest (stars).



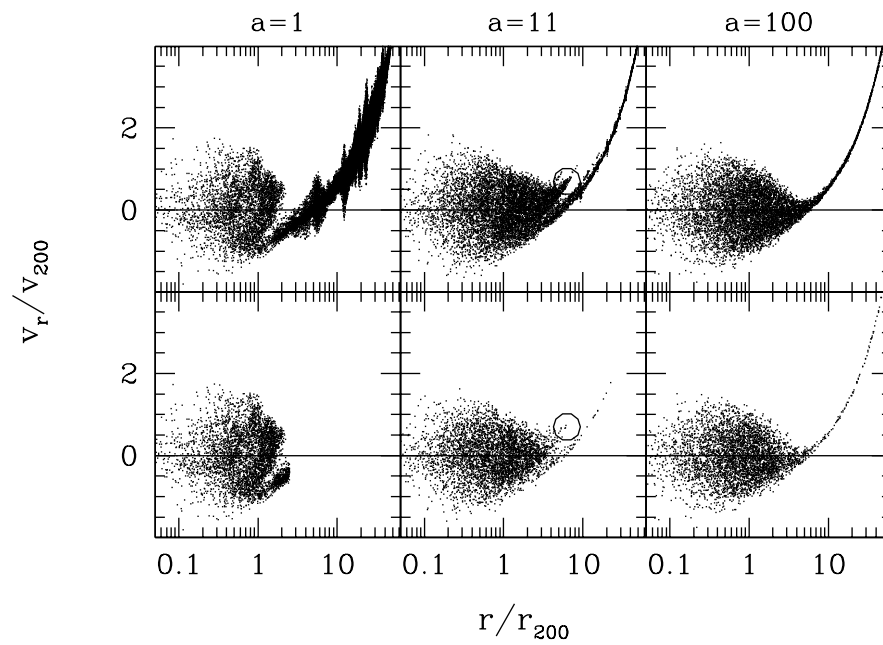


**Figure 4.3.** Radial velocity relative to the cluster center as a function of distance for particles in the largest halo at the epochs indicated. The upper panel shows all matter while the lower panel shows only those particles that lie within  $2.5r_{200}$  at  $a = 1$ .

as the upper dashed line in the figure.

#### 4.2.1 Halo Phase-space Structure

In the far future, the character of halos' radial phase-space structure is markedly different from that of today. The upper row of Figure 4.3 shows the radial velocity pattern of the most massive halo at  $a = 1$ , 11 and 100. The halo identified at present remains the most massive at all future times. At each epoch, lengths are expressed in units of  $r_{200}$ , the radius within which the mean enclosed density is 200 times the critical value. Physical velocities are expressed in units of  $v_{200} = \sqrt{GM_{200}/r_{200}}$ , where  $M_{200}$  is the mass within  $r_{200}$ . The halo's physical size grows from  $M_{200} = 1.08 \times 10^{15} h^{-1} M_{\odot}$  at  $a = 1$  to  $2.35 \times 10^{15} h^{-1} M_{\odot}$  at  $a = 11$ , and remains nearly constant thereafter.

At  $a = 1$ , positive velocity particles at radii  $r/r_{200} \sim 1-2$  represents material that has penetrated the halo core and is streaming outward to large radii. This “processed” material mixes at these radii with a fresh stream infalling at  $v_r \simeq -v_{200}$ . The stream extends outward through a zero-velocity surface at  $r \simeq 5r_{200}$ , and asymptotically approaches the Hubble flow at large radii. The present-epoch interior phase structure displays a lumpy morphology, evidence of recent merger activity that has not yet dynamically relaxed. The infall pattern shows spikes of enhanced dispersion, the signatures of neighboring halos. Those within the gravitational sphere of influence are destined to merge with the central halo.

By  $a = 11$ , phase mixing has smoothed the interior structure considerably, but the remains of a recent merger can be seen in a small tail of outflow centered at  $r/r_{200} \sim 6$  (circled in the panel). The infall regime is much quieter, with only a few collapsed structures evident in the tail of Hubble flow. At  $a = 100$ , the interior phase structure is extremely homogeneous and the infall regime is essentially silent; no collapsed structures perturb the flow within  $50r_{200}$ .

The lower panels of Figure 4.3 show how the non-linear material of the present cluster evolves into the future. Only those particles lying within  $2.5r_{200}$  at  $a = 1$  are shown. This radius is chosen to encompass all the “processed” halo material at the present epoch. Although this boundary extends beyond most common choices for the “virial radius” of a halo (Evrard et al., 1996; Eke et al., 1996; White, 2001), it is evident that some material currently within this radius is destined for future escape. A thin tail forms of material lifted off the halo, representing 0.8 and 2.6 percent (at  $a = 11$  and 100, respectively) of the mass within  $2.5r_{200}$  at  $a = 1$ . Note that the merger system at  $a = 11$  circled in the upper panel is not as strongly evident in the lower panel, indicating that it lies beyond  $2.5r_{200}$  at the present epoch.

The simple, smooth phase structure at late times suggests a long-term equilibrium. In the next subsection, we address the question of the eventual shape of the radial mass profiles of halos.

#### 4.2.2 Halo Density Profile

Numerical studies have revealed that the non-linear density structure of halos formed through gravitational clustering takes on a common form. The first such studies (Navarro et al., 1996a,b) showed that this density profile can be written in the form

$$\rho(r) = \frac{4\rho_s}{r/r_s[1 + (r/r_s)]^2}, \quad (4.14)$$

where  $r_s$  is a characteristic radius where the logarithmic slope of the density profile is isothermal:  $d\ln\rho/d\ln r = -2$ . The ratio  $r_{200}/r_s$  defines the concentration parameter  $c$ . Note we have chosen the convention  $\rho_s = \rho(r_s)$ ; in this case the inner density can be directly related to the concentration of an NFW profile via

$$\rho_s = \frac{1}{4}\delta_c\rho_c = \frac{\Delta}{12} \frac{c^3}{\ln(1+c) - c/(1+c)} \rho_c. \quad (4.15)$$

Previous fits to this density profile have been limited to radii  $r \lesssim r_{200}$  and epochs  $a \leq 1$ . We present here an extension of this form to larger radii and future epochs.

Figure 4.4 shows radial density profiles derived from stacking the 50 most massive halos at each epoch displayed. Solid lines in the figure show binned profiles for five epochs from  $a = 1 - 100$ , while dashed lines show fits to the form

$$\rho(r) = \frac{A\rho_s}{r/r_s[1 + (r/r_s)^p]^{3/2}}[1 + r/r_\infty]^{1+3p/2}. \quad (4.16)$$

Here  $r_s$  is a scale radius similar to the that of equation (4.14),  $r_\infty$  is an asymptotic radius,  $p$  is a free parameter and  $A = 2^{3p/2}/[1 + r_s/r_\infty]^{1+3p/2}$ . We find that values  $p = 1.8$ ,  $r_s = 0.50$  and  $r_\infty = 4.7r_{200}a^{6/(3p+2)}$  provide fits that are accurate to  $\langle(\delta\rho/\rho)^2\rangle^{1/2} \sim 35\%$  over the full range of radii and epochs examined. The scaling of  $r_\infty$  with expansion factor ensures that the profile approaches the mean mass density of the universe as  $r \rightarrow \infty$ .

The profile of equation (4.16) is steeper than the NFW form at radii beyond  $r_{200}$ . As  $r_\infty \rightarrow \infty$ , the logarithmic slope of the profile well beyond  $r_{200}$  approaches 3.7 (shown by the dot-dashed curve in Figure 4.4), steeper than the slope of 3 from the NFW case. This difference in slope keeps the enclosed mass from being logarithmic divergent, as implied by a formal extrapolation of the NFW form (compare equation [4.14] with [4.16]).

In fact, the mass of a halo in the far future will be simpler to define than it is today. At present, radial infall and incomplete dynamical relaxation make the choice of the “edge” of a cluster somewhat arbitrary (White, 2001; Evrard & Gioia, 2002). In the relatively near future, however, halos evolve toward an equilibrium configuration that is bounded by an increasingly sharp zero-velocity surface (Figure 4.3). Ultimately, a meaningful and unique definition of mass emerges, namely, all of the matter lying interior to this well-defined zero-velocity surface. In addition, as shown by Figure 4.4, the density profile attains a well-defined form.

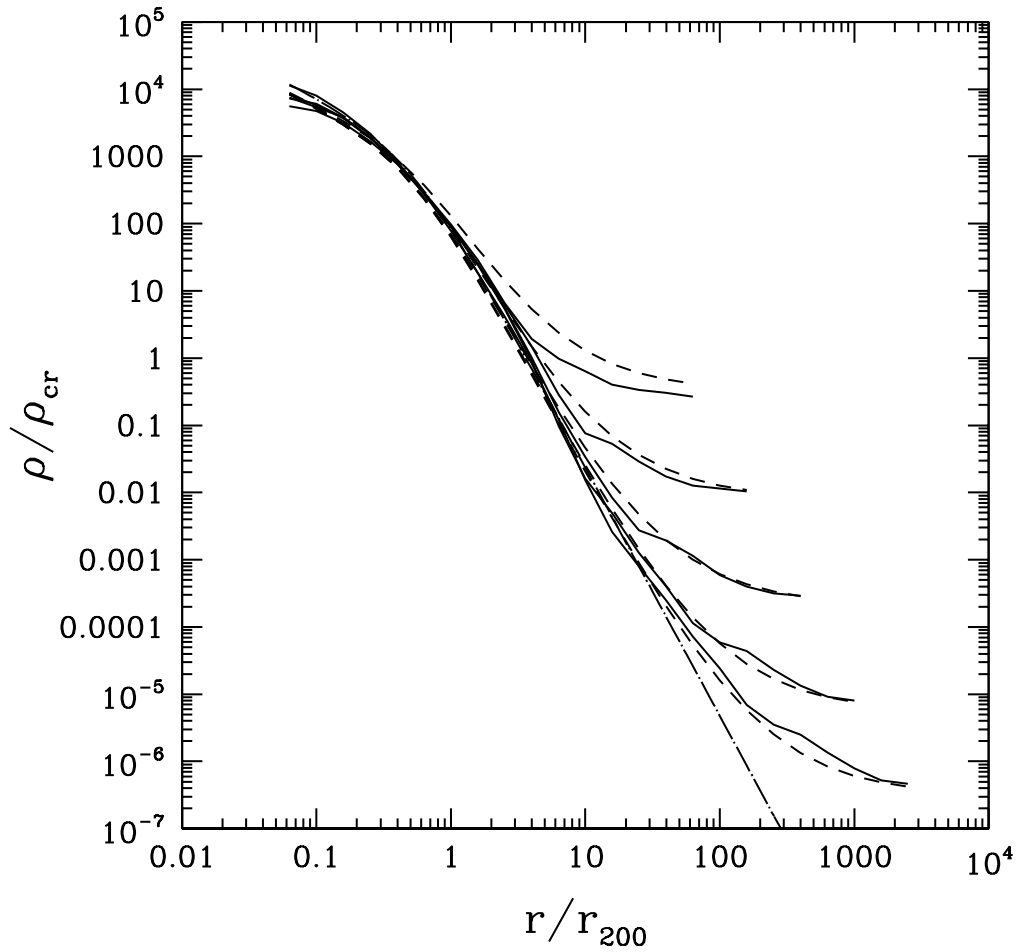


**Figure 4.4.** The asymptotic form for the density distribution of dark matter halos. The solid curves show the (nearly) universal form for dark matter halos, for a variety of epochs (from top to bottom,  $a = 1, 3.38, 11.4, 38.6,$  and  $100$ ). Starting just after the present time, the dark matter halo profiles show essentially the same form, only the outer boundary is stretched to match onto the ever-lower density of the background universe. The dashed curves show the fit to the numerical results, equation (4.16), evaluated at each epoch with the parameters given in the text. The dot-dashed curve shows the asymptotic form of the density profile in the limit  $t \rightarrow \infty$ .

### 4.3 Long-Term Ramifications Of Cosmic Acceleration

The considerations of the previous sections outline the requirements necessary for future structure formation and the criteria for test bodies to remain bound to existing astronomical structures. With these results in place, we can fill out the picture of the future evolution of our cosmos. In particular, we can determine the time scales for various bound structures to grow isolated, the corresponding effects on the background radiation fields in the universe, and the freezing out of particle annihilation processes.

#### 4.3.1 Isolation of bound structures

Because our universe contains a dark vacuum component, it has a well-defined horizon scale. For unbound objects living in this accelerating universe, the next issue is thus to determine when the objects leave the horizon. The background universe can be described by its line element, which can be written in advanced time coordinates in the form

$$ds^2 = -[1 - \chi^2 r^2] dv^2 + 2dvdr + r^2 d\Omega^2. \quad (4.17)$$

This line element ignores the curvature due to gravitationally-condensed structures (see the following subsection). The parameter  $\chi$  is related to the magnitude of the cosmological constant and is defined by the relation (in natural units)

$$\chi = \left(\frac{2\pi^3}{45}\right)^{1/2} \frac{\Lambda^2}{M_{\text{pl}}}, \quad (4.18)$$

where  $\Lambda$  is the effective temperature scale of the cosmological vacuum energy ( $\Lambda \approx 0.003 \text{ eV} \approx 35 \text{ K}$  for the presently suspected cosmological constant). In such a universe, the horizon distance  $r_H$  is given by

$$r_H = \chi^{-1} = \frac{c}{H_0} \frac{2}{\pi} \left(\frac{15}{\Omega_{\text{v},0}}\right)^{1/2} \approx 12,600 \text{ Mpc}, \quad (4.19)$$

where the second equality assumes the standard values  $\Omega_{\text{m},0} = 0.3$  and  $\Omega_{\text{v},0} = 0.7$ . This horizon distance  $r_H$  is not the same as the particle horizon, but rather is essen-

tially the Hubble radius. This distance scale  $r_H$  provides an effective “boundary for microphysics” within the much larger space-time of the universe (for further discussion of horizons, see Kolb & Turner, 1990; Ellis & Rothman, 1993).

For a flat universe with both matter and vacuum components, the scale factor  $a(t)$  increases according to the function (e.g., Loeb, 2002)

$$a(t) = \left( \frac{\Omega_{m,0}}{1 - \Omega_{m,0}} \right)^{1/3} \left\{ \sinh \left[ \frac{3}{2} \sqrt{1 - \Omega_{m,0}} H_0 t \right] \right\}^{2/3}. \quad (4.20)$$

At later times, the scale factor approaches the simpler asymptotic form

$$a_{\text{asym}}(t) = \left( \frac{\Omega_{m,0}}{4\Omega_{v,0}} \right)^{1/3} \exp[\sqrt{\Omega_{v,0}} H_0 t]. \quad (4.21)$$

One can see immediately that the e-folding time scale of the future universe is  $\tau_e = \Omega_{v,0}^{-1/2} H_0^{-1} \approx 17$  Gyr. Furthermore, the scale factor  $a(t)$  approaches this asymptotic form on an even shorter time scale. If the full expression (equation [4.20]) is written as the asymptotic form (equation [4.21]) plus correction terms, those correction terms decay with a time scale  $\tau = (3H_0\sqrt{\Omega_{v,0}})^{-1} = \tau_e/3 \approx 5.6$  Gyr. This time scale — somewhat longer than the age of the solar system and appreciably younger than the current age of the universe — is a direct manifestation of the cosmological constant problem.

Given that any extant cosmic structure has a sphere of influence (equation [4.11]) and that the universe has a fixed horizon size  $r_H$ , every structure will become isolated when the radius of its sphere of influence is stretched beyond the horizon, i.e., when  $a(t)r_0 > r_H$ . For a structure of mass  $M_{\text{obj}}$ , isolation occurs at a time  $t_{\text{iso}}$  given by

$$t_{\text{iso}} = \frac{2}{3} \tau_e \sinh^{-1} \left\{ \left[ \frac{4\beta^* (15)^{3/2}}{\pi^3} \frac{c^3 \tau_e}{GM_{\text{obj}} \Omega_{m,0}} \right]^{1/2} \right\}. \quad (4.22)$$

As a result, for vast majority of cosmological time, the cosmos will be divided into “island universes” in the sense that bound clusters of galaxies will retain their sizes (a few to several Mpc) while the distance between clusters grows exponentially (see also Chiueh & He (2002)). Given typical cluster sizes and separations, we predict that

clusters will grow isolated in about 120 Gyr. For the particular values appropriate for the nearby Virgo cluster, equation (4.22) implies an isolation time of 132 Gyr (this time is the age of the universe at the time of isolation; since the universe is already about 14 Gyr old, this event will occur 118 Gyr from now). Structures with lower mass have smaller spheres of gravitational influence and require longer times to grow isolated. Our local group, with an estimated mass of  $M_{LG} \approx (2.3 \pm 0.6) \times 10^{12} M_{\odot}$  (van den Bergh, 1999), will be isolated at cosmic age  $t = 175$  Gyr. As another example, a star that is not gravitationally bound to a larger structure (e.g., one that has been scattered out of a galaxy) requires somewhat longer to become isolated — about 336 Gyr. For comparison, the lifetimes of the smallest, longest-lived stars are measured in tens of trillions of years (Laughlin et al., 1997; hereafter LBA97), about one hundred times longer than the isolation time for galaxy clusters. For most of eternity, and indeed for most of the Stelliferous Era, clusters will be alone. Inside the galaxies, the expansion has essentially no effect, and star formation and stellar evolution continue for trillions of years (AL97). When viewed on the large scale, however, these clusters will behave like point sources, pumping radiation into an ever-expanding void.

### 4.3.2 Asymptotic structure of space-time

In the long term, existing cosmic structures will remain bound, but will grow isolated. These structures will be embedded within an accelerating universe with a constant horizon scale (equation 4.19). This process effectively divides the present-day universe into many smaller regions of space-time. These “island universes” display properties of a universal nature.

Every given “island universe” will approach a fixed overdensity. The energy density contained within the horizon scale is equivalent to a mass  $M_H$  given by

$$M_H = \frac{4\pi}{3} \rho_{V(t \rightarrow \infty)} r_H^3 = \frac{\Omega_{v,0}}{2GH_0} \left(\frac{2c}{\pi}\right)^3 \left(\frac{15}{\Omega_{v,0}}\right)^{3/2} \approx 8 \times 10^{23} M_{\odot}. \quad (4.23)$$



Since the mass contained within any given isolated cluster will be constant, the overdensity approaches a constant value. For our particular environment, the local group will remain bound with its mass of about  $M_{LG} = 2.3 \times 10^{12} M_{\odot}$ . The mass in our local region is thus destined to be a minor perturbation on the cosmos itself, even within our local island universe. For cosmic ages older than 175 Gyr, the mass contribution to the universe contained within the local group is given by  $\delta_{\infty} = M_{LG}/M_H \approx 3 \times 10^{-12}$ , only 3 parts per trillion.

Our numerical simulations indicate that cosmic structures, from galaxies to clusters, tend to develop universal forms for their density profiles. As a result, every island universe will attain the same general form for its space-time. In particular, since the density profile attains the universal form described by equation (4.16), the line element  $ds^2$  for the space-time within the horizon distance  $r_H$  also attains a universal form. If we take the center of the coordinate system to be the center of the cluster and assume that the mass distribution is spherically symmetric, the line element can be written in the form

$$ds^2 = -\left(1 - A(r) - \chi^2 r^2\right) dt^2 + \left(1 - B(r) - \chi^2 r^2\right)^{-1} dr^2 + r^2 d\Omega^2, \quad (4.24)$$

where  $A(r)$  and  $B(r)$  depend on the mass distribution (see, e.g., Misner et al., 1973). This form for the line element is that of a mass distribution embedded in deSitter space (see also Bardeen, 1981; Mallett, 1985; Chiueh & He, 2002). As a result, there exists an outer horizon at  $r = \chi^{-1}$ . We provide a more detailed specification of the metric in chapter 5.

The outer horizon supports the emission of radiation through the Gibbons/Hawking mechanism (Gibbons & Hawking, 1977). As a result, the universe will be filled with a nearly thermal bath of radiation with characteristic wavelength  $\lambda \sim r_H \sim \chi^{-1} \sim 12,600$  Mpc and characteristic temperature  $T \sim \chi \sim \Lambda^2/M_{\text{pl}} \sim 10^{-33}$  eV  $\sim 10^{-29}$  K.

This bath of radiation will become the dominant background radiation field at late times (after about one trillion years – see the following section).

### 4.3.3 Background radiation fields in an accelerating universe

As the universe expands, all radiation fields are redshifted to longer wavelengths. An important milestone is reached when the typical wavelength of a given radiation field grows longer than the cosmological horizon scale defined by equation (4.19). After this crossing, the photons are larger than the largest “box” that the universe has to contain them. For later times, it no longer makes sense to describe the photons in terms of a distribution function. Inside the horizon, in the limit  $\lambda \gg r_H$ , the background photons will appear as “slowly” varying electric fields rather than as particles of light. The dominant background radiation field will be that produced by the horizon itself through the Gibbons/Hawking mechanism (Gibbons & Hawking, 1977; see also §4.3.2, Fulling, 1977; Birrell & Davies, 1982).

Given the scale factor of the universe and the present day wavelength of a radiation field, it is straightforward to find the time at which the photons are stretched beyond the horizon scale, i.e., when  $\lambda a(t) > r_H$ . For the cosmic background radiation, the present day wavelength (at the peak of the distribution) is about  $\lambda_0 = 0.1$  cm and the photons cross the horizon at a time of 1120 Gyr.

The cosmic background photons are stretched beyond the horizon well before the stars stop shining. Star formation and stellar evolution will continue until the universe is tens of trillions of years old (AL97, LBA97). Suppose that stars continue to shine for 10 trillion years. By this late epoch, most of the remaining stars will be red dwarfs that emit light with a characteristic wavelength of  $\lambda = 1 \mu\text{m} = 10^{-4}$  cm. If this red light is emitted up to a time  $t_*$  ( $\approx 10^{12}$  yr) and observed at a later time  $t$ , its observed wavelength is given by

$$\lambda_{\text{obs}} = \lambda_{\text{emit}} \frac{a_{\text{obs}}}{a_{\text{emit}}} = \lambda_{\text{emit}} \exp \left[ (t - t_*) / \tau_e \right], \quad (4.25)$$

where  $\tau_e = 17$  Gyr is the e-folding time of the future universe. Starlight leaves the horizon when  $\lambda_{\text{obs}} > r_H$ . Using this criterion in conjunction with equations (4.19) and (4.20), we find that starlight is redshifted out of the horizon over a time interval of only  $\Delta t = (t - t_*) = 1260$  Gyr. Stellar evolution times — for the smallest stars — are much longer than the cosmological expansion times, so that photons are rapidly stretched beyond the horizon. Specifically, this stretching time is a small fraction of the Stelliferous Era, the time over which the universe will contain substantial numbers of hydrogen burning stars, i.e.,  $\Delta t/t_* \approx 10^{-2}$ .

When the temperature of cosmic background radiation cools below the temperature of the Gibbons/Hawking radiation associated with the cosmological event horizon, the universe reaches an important milestone (Gott, 1996). After this time, instead of continuing to cool, the universe maintains a background temperature  $T \sim 10^{-29}$  K. Dyson (1979) argued that an intelligent civilization could last forever by operating at ever lower temperatures to conserve its finite energy resources. If the universe approaches a fixed temperature, however, this strategy becomes impossible (Krauss & Starkman, 2000; Gott, 1996) and such civilizations cannot have an infinite number of thoughts.

#### 4.3.4 Particle annihilation in an accelerating universe

For material between galaxies — particles that are not bound to large structures — future evolution can continue through particle annihilation. The number density  $n$  of a given particle species is given by the evolution equation

$$\frac{dn}{dt} + 3Hn = -\langle\sigma v\rangle n^2, \quad (4.26)$$

where  $\langle\sigma v\rangle$  is the appropriate average of the interaction cross section and the relative velocity (see, e.g., Kolb & Turner, 1990; see also Čirković & Samurović, 2001). For an accelerating universe with a cosmological constant, the solution to equation (4.26)

can be found and written in terms of the scale factor, i.e.,

$$n(a) = n_0 a^{-3} \left\{ 1 + \frac{2\Gamma}{3\Omega_{m,0}} \left[ 1 - \sqrt{\Omega_{v,0} + \Omega_{m,0} a^{-3}} \right] \right\}^{-1}, \quad (4.27)$$

where  $n_0$  is the particle density at the present epoch and where we have defined  $\Gamma \equiv \langle \sigma v \rangle n_0 / H_0$ . The leading factor ( $a^{-3}$ ) represents the dilution of the number density due to cosmic expansion, whereas the second factor in brackets incorporates the effects of continued particle annihilation. In an accelerating universe, annihilation is highly suppressed. For example, in the asymptotic limit  $t \rightarrow \infty$ ,  $a \rightarrow \infty$ , this factor becomes  $\mathcal{F} = 1 + 2\Gamma(1 - \sqrt{\Omega_{v,0}})/3\Omega_{m,0} \approx 1 + 0.0048 [\langle \sigma v \rangle / \text{barn} \cdot c]$ . For electron-positron annihilation, for example, the maximum correction term is less than a percent. For annihilation of cold dark matter particles (thought to be the dominant matter contribution), the interaction cross sections are typically thought to lie in the range  $\sigma \sim 10^{-12} - 10^{-14}$  barn (e.g., Kolb & Turner, 1990) and the speed  $v/c \sim 10^{-3}$ . As a result, the already small correction term (0.0048) is suppressed by an additional 16 orders of magnitude. This enormous suppression is driven by the relentless expansion of an accelerating universe.

When the number density grows so diffuse that the universe contains less than one particle per horizon volume, then individual particles are effectively isolated. The condition for such isolation can be written in the form

$$a(t) > \left( \frac{4\pi}{3} n_0 \right)^{1/3} r_H, \quad (4.28)$$

where the scale factor  $a$  is given by equation (4.20) and the horizon scale is given by equation (4.19). Adopting a present day number density of  $n_0 = 10^{-6} \text{ cm}^{-3}$  results in a particle isolation time scale of about 1060 Gyr.

## 4.4 Discussion And Conclusions

This chapter explores the future evolution of a universe dominated by dark vacuum energy. Analytic estimates are compared to results of numerical simulations that

follow the evolution of future structures in such an accelerating universe.

For a universe with cosmological constant  $\Omega_{v,0} = 0.7$ , only those regions with present-day overdensities  $\delta_0 > 17.6$  will remain gravitationally bound, in agreement with earlier estimates (Lokas & Hoffman, 2001; Nagamine & Loeb, 2003). We generalize this result to include quintessence models with constant forms for the equation of state (Appendix A). We have also derived the condition required for test bodies to remain bound to existing structures (see equation [4.11]) and verified its validity with numerical simulations (to within  $\sim 10\%$ ; see Figure 4.2). Any collapsed object — from a star to galaxy cluster — has a finite sphere of gravitational influence in an accelerating universe, with radius  $r_0 \approx 1 \text{ Mpc } (M_{\text{obj}}/10^{12}M_{\odot})^{1/3}$ . For quintessence models, we have derived an analogous result for the sphere of gravitational influence (see Appendix A and equation [A.7]).

From a co-moving perspective, the large-scale appearance of the future universe is little changed from that of today. Matter in the cosmic web drains efficiently into collapsed halos that shrink in comoving coordinates. The halos are essentially frozen in place while their contrast relative to the mean background grows with time. In physical coordinates, the view is rather different. The vast majority of the galaxies now visible are pulled out of the immediate horizon of any given bound structure (a cluster or group). In the long term, only the cluster or group itself remains within the effective horizon scale of  $r_H = 12,600 \text{ Mpc}$ .

The long-term structure of space-time consists of a flat metric dimpled with isolated clusters that approach a fixed mass profile. We find that halo density profiles approach a form similar to, but steeper at large radii than, the NFW profile (equation [4.16]). It is important to emphasize that every halo grows isolated in the long term, i.e., every gravitationally bound mass concentration ultimately becomes the only structure within its own island universe. In each such local region, the halo density takes the form shown in Figure 4.4 and the line element of the space-time

metric takes the form given by equation (4.24). Although the halo mass varies from region to region, the form of the metric – and hence the geometry of space-time – is nearly universal. In all cases, the halo mass in any region provides only a minor contribution to the overall mass/energy budget, with  $M_{\text{obj}}/M_H \sim 10^{-11}$ .

**Table 4.1.** Time Scales and Scale Factors

<i>Event</i>	<i>Time</i> $\tau$ (Gyr)	$a(\tau)$
Time scale for scale factor to approach exponential form	5.6	–
Inverse Hubble constant $H_0^{-1}$	14	–
e-folding time of the future universe $(H_0\sqrt{\Omega_{v,0}})^{-1}$	17	–
Current age of the universe	13.7	1
Virgo Cluster leaves our horizon	132	1000
The Local Group grows isolated	180	$2 \times 10^4$
Exiled stars become isolated	336	$2 \times 10^8$
Individual particles grow isolated	1060	$6 \times 10^{26}$
CMB photons stretch beyond the horizon	1120	$2 \times 10^{28}$
Optical photons stretch beyond the horizon	1260	$10^{32}$
Lifetime of longest-lived stars	17,000	$10^{434}$
End of the Stelliferous Era	100,000	$10^{2554}$

As the universe continues to expand, and accelerate, cosmic radiation fields are redshifted to increasingly long wavelengths. After about one trillion years, the cosmic background radiation (leftover from the big bang) is stretched beyond the horizon and the dominant radiation background is that emitted by the horizon itself through a Hawking-like mechanism. Many of the results of this investigation can be summarized in terms of the relevant time scales, which are listed in Table 4.1. To emphasize the mismatch between the various time scales, the table also lists the scale factor for each relevant epoch. For example, individual stars grow isolated in 336 Gyr ( $a = 2 \times 10^8$ ), but the longest-lived stars burn hydrogen for 17,000 Gyr (when  $a = 10^{434}$ ).

With the analysis complete, many of the time scales and length scales of the future universe can be understood in simpler terms. A dimensional analysis – presented in

Appendix B – shows that the most important time scale is given by the asymptotic form for the Hubble parameter  $H_\infty = \sqrt{\Omega_{v,0}} H_0 \approx 59 \text{ km s}^{-1} \text{ Mpc}^{-1}$ . The accelerated expansion itself completely dominates the evolution of the universe as a whole, so that all of the time scales are determined by  $H_\infty^{-1} \approx 17 \text{ Gyr}$  and logarithmic multiplying factors (see Appendix B). By comparison, time scales for stellar evolution ( $10^{13} - 10^{14}$  yr; AL97, LBA97) and dynamical relaxation of galaxies ( $10^{20}$  yr; BT87) are much longer.

## CHAPTER 5

# The Asymptotic Structure of Space-Time

An additional implication of the newly consolidated cosmological model and studies of the previous chapter is that the large scale space-time of the universe is known and its corresponding metric can be specified. In the absence of structure formation, the universe is homogeneous and isotropic, and the space-time would be described by the maximally symmetric Robertson-Walker metric (Kolb & Turner, 1990). Since the universe does contain gravitationally collapsed structures, however, the metric that describes space-time is one step more complicated — it must include the contribution from the structures.

As discussed in chapter 4, because of the dark energy the the universe will approach a state of exponential expansion and growing cosmological perturbations will freeze out on all scales in the near future. Existing structures will grow isolated and their future evolution can be predicted with a high degree of confidence. In addition to chapter 4, several recent papers have begun to explore the possible future effects of vacuum energy density (Adams & Laughlin, 1997; Loeb, 2002; Nagamine & Loeb, 2003; Gudmundsson & Björnsson, 2002; Chiueh & He, 2002), and demonstrate that the universe will indeed break up into a collection of “island universes”, each containing one gravitational bound structure.

In this chapter, we further analyze the simulation described in section 4.2 to study the structure of our  $a = 100$  halos. These numerical experiments show that each gravitationally bound halo structure grows isolated and that its density profile



always approaches the same general form. After specifying the form of this density profile, we construct the metric for each isolated patch of space-time. Each island universe attains the same geometry and we find the universal form for the metric that describes these patches of space-time.

In the long term, existing cosmic structures remain bound but grow isolated, as illustrated by the lower right panel of Figure 4.1, which represents region space with physical size  $128h^{-1}\text{Mpc}$  at  $a = 100$  centered on a massive halo. In contrast, the upper left panel shows the same region at  $a = 1$ . A large cluster such as this will become effectively isolated in about 120 Gyr, whereas a smaller structure (like our Local Group) will grow isolated in about 180 Gyr. These structures will be embedded within an accelerating universe with a constant horizon scale, where the horizon distance  $r_H$  is given by

$$r_H = \chi^{-1} = \frac{c}{H_0} \frac{2}{\pi} \left( \frac{15}{\Omega_{v,0}} \right)^{1/2} \approx 12,600 \text{ Mpc}. \quad (5.1)$$

This horizon distance  $r_H$  is not the same as the particle horizon, but rather is essentially the Hubble radius. The distance scale  $r_H$  provides an effective “boundary for microphysics” within the much larger space-time of the universe (Kolb & Turner, 1990). The acceleration of the universe effectively divides our present-day space-time into many smaller “island universes”. For this discussion, we consider the center of each dark matter halo to lie at the center of its own island universe. As we show next, these dark matter halos develop density profiles with a universal form in both time and mass (for our chosen cosmology).

## 5.1 Generic Form for the Density Profile.

Numerical simulations indicate that cosmic structures, from galaxies to clusters, tend to develop the same basic form for the density profiles of their dark matter halos (Navarro et al., 1996b). As a result, every island universe will attain the same geometry for its space-time. In order to estimate the geometry of these space-times,

we must first estimate the (nearly universal) form for the density profile of the dark matter halos.

Using the results from our numerical simulations, we have constructed a composite dark matter halo from the 50 largest halos produced by one realization of the simulation. These 50 halos are normalized so that the mean interior density has the same value at the spatial scale  $r_{200}$  (the radius at which the enclosed density is 200 times the critical density). With this normalization, the individual dark matter halos show relatively little dispersion in properties such as their radial density profile (about 35 percent) and hence the composite average is well defined. The profiles are close to being spherically symmetric (this point is discussed in Busha et al., 2003; Jing & Suto, 2002) so we consider density distributions that depend only on radius. The composite profiles are shown in Figure 4.4 for varying cosmological epochs, starting from the present (top curve) and extending to  $a = 100$  (bottom curve). Notice how the density profiles display the same characteristic form over a wide range of epochs, with each subsequent profile being a stretched version of the previous one. This fact that dark matter halos tend to approach a universal form has been noted earlier (Navarro et al., 1996b), although the previous composite profiles were more limited in spatial extent and did not match smoothly onto the background universe.

The density profile at every cosmological epoch can be fit with a spherical density profile of the form

$$\rho(r) = \frac{\rho_0}{r/r_S [1 + (r/r_S)^p]^{3/2}} [1 + r/r_\infty]^{1+3p/2}. \quad (5.2)$$

This profile describes the basic radial dependence of dark matter halos in the inner regions and matches smoothly onto the background density of the universe at large radii. Using the parameters  $r_S = 0.50 r_{200}$  and  $p = 1.8$ , the above functional form provides a good fit to the numerically determined density profiles for all epochs. In order to match the profile onto the background density of the universe, the remaining parameter  $r_\infty$  must scale according to  $r_\infty = r_{\infty(0)} a^{6/(3p+2)}$ , where the present-day

value  $r_{\infty(0)} = 4.7 r_{200}$ . The resulting fits to the density profiles are shown as the dashed curves in Figure 4.4. This relatively simple function (equation [5.2]) applies over a factor of 10 in halo mass scale, and fits the numerically calculated density profiles over nearly 5 decades in radial scale, 11 decades in density, and a factor of 100 in the scale factor  $a$ . Over this range, the RMS departure of the fitted functions (equation [5.2]) from the composite averages is 0.13 in  $\log_{10} \rho$  (which corresponds to differences of  $\sim 35\%$  in  $\rho$ ).

## 5.2 Asymptotic Form for the Metric

Using the specified form (equation [5.2]) for the density profile, we can now determine the line element  $ds^2$  for the space-time within the horizon distance  $r_H$  (Misner et al., 1973). The center of the coordinate system is taken to be at the center of the cluster (or galaxy) and the mass distribution is assumed to be spherically symmetric. We begin by writing the line element in the form

$$ds^2 = -\left(1 - A(r) - \chi^2 r^2\right) dt^2 + \left(1 - B(r) - \chi^2 r^2\right)^{-1} dr^2 + r^2 d\Omega^2, \quad (5.3)$$

where we have explicitly separated out the contribution due to the cosmological constant, which is set by the parameter  $\chi^2 \equiv (2\pi^3/45)^{1/2} \Lambda^2 / M_{\text{pl}}$  (where the energy scale  $\Lambda \approx 0.0003$  eV for  $\Omega_{\text{v},0} = 0.7$ ). In an “empty” universe containing only vacuum energy, the line element would have the above form with  $A = 0 = B$ . Because of the vacuum contribution, the metric contains an outer horizon at  $r_H = \chi^{-1}$ . This outer horizon supports the emission of radiation through a Hawking-like mechanism (Birrell & Davies, 1982) and hence the future universe will be filled with a nearly thermal bath of radiation with temperature  $T \sim \chi \sim 10^{-33}$  eV and characteristic wavelength  $\lambda \sim r_H \sim 12,600$  Mpc. This radiation will become the dominant background radiation field after about one trillion years. The functions  $A(r)$  and  $B(r)$  take into account additional curvature due to the mass distribution, which has a density profile given by equation [5.2].

If we adopt units in which  $c = 1$  (and hence  $G = M_{\text{pl}}^{-2}$ ), the function  $B(r)$  can be written in the form

$$B(r) = 2G \frac{m(r)}{r} = 8\pi G \frac{1}{r} \int_0^r \rho(\tilde{r}) \tilde{r}^2 d\tilde{r}, \quad (5.4)$$

where the density profile  $\rho(r)$  is given by equation [5.2]. Since we are interested in the asymptotic form for the metric, we can consider late times for which the scale  $r_\infty$  is stretched beyond the horizon  $r_H$ . In this limit, the function  $B(r)$  can be simplified to the form

$$B(r) = 4\pi G \rho_0 r_S^2 \frac{1}{\xi} \int_0^\xi \frac{x dx}{(1+x^p)^{3/2}} \equiv \eta_0 \beta(\xi). \quad (5.5)$$

In the second equality, we have defined the parameter  $\eta_0 = 4\pi G \rho_0 r_S^2$  which sets the “strength” of the curvature and the dimensionless function  $\beta(\xi)$  which specifies the radial dependence of the metric coefficient (where  $\xi = r/r_S$ ). For typical values, the strength parameter  $\eta_0 \approx 10^{-6}$ , indicating that the departure from flatness is relatively small. The resulting function  $\beta(\xi)$  is shown in Figure 5.1.

The function  $A(r)$  is related to the usual gravitational potential  $\Phi$  through the definition  $e^{2\Phi} \equiv 1 - A(r)$  [12], where the potential is defined through the source equation

$$\frac{d\Phi}{dr} = \frac{G[m(r) + 4\pi r^3 p]}{r(r - 2Gm)}. \quad (5.6)$$

In this setting, the mass is dominated by collisionless dark matter particles and the pressure  $p$  is negligible. Furthermore, the potential is small so that we can use the approximation  $e^{2\Phi} \approx 1 + 2\Phi$  and hence  $A(r) = -2\Phi(r)$ , with  $\Phi$  given by the integral of equation [5.6]. As a result, the function  $A(r)$  can be written in the form

$$A(r) = A_\infty - \int_0^r \frac{2Gm(r)}{r} \frac{dr/r}{1 - 2Gm(r)/r} = \eta_0 \left[ \alpha_\infty - \int_0^\xi \frac{\beta(\xi)}{1 - \beta(\xi)} \frac{d\xi}{\xi} \right] \equiv \eta_0 \alpha(\xi), \quad (5.7)$$

where  $\eta_0$  and  $\beta(\xi)$  are as defined previously. We have also defined an analogous dimensionless function such that  $A(r) = \eta_0 \alpha(\xi)$ . The quantity  $A_\infty$  and its dimensionless counterpart  $\alpha_\infty$  are defined so that the potential  $\Phi$  vanishes at spatial infinity

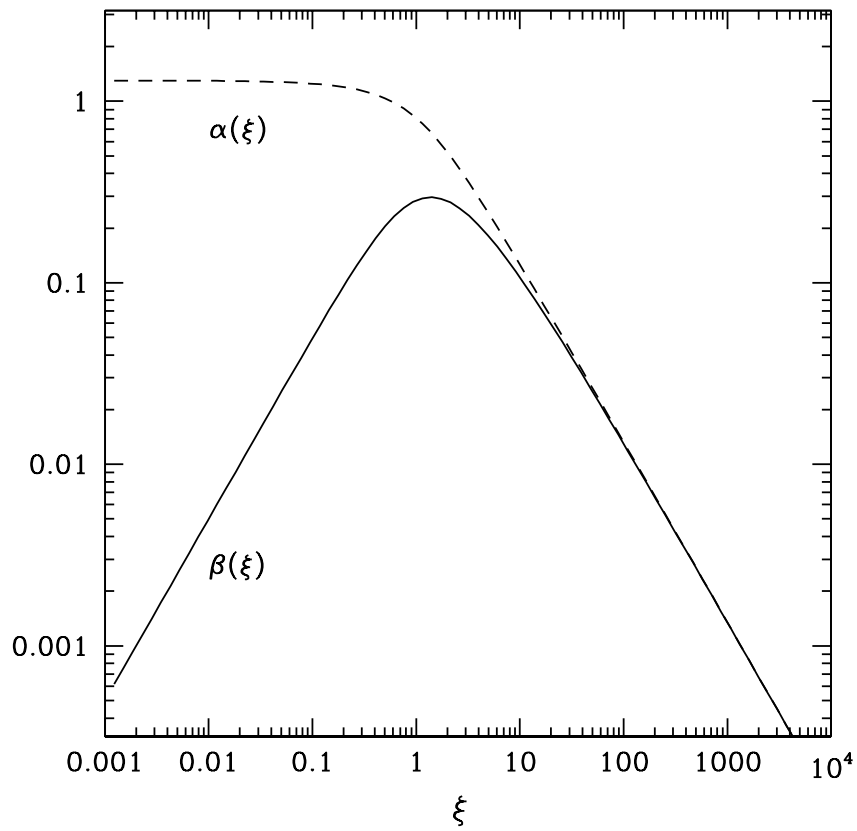


**Figure 5.1.** The dimensionless functions  $\alpha(\xi)$  and  $\beta(\xi)$  appearing in the asymptotic form of the space-time metric of equation [5.8]. The functions are plotted versus the dimensionless radial coordinate  $\xi = r/r_S$  (see text). These functions, in conjunction with equation [5.8], specify the line element for the majority of the life of the universe.

(Misner et al., 1973). As before, the dimensionless parameter  $\eta_0 = 4\pi G\rho_0 r_S^2 \approx 10^{-6}$  sets the level of the curvature. The resulting function  $\alpha(\xi)$  is shown in Figure 5.1. This completes the specification of the metric.

### 5.3 Summary

In this chapter, we have constructed the asymptotic form of the metric that describes space-time in our cosmological future. Using numerical simulations, we have demonstrated that individual gravitationally bound structures will become isolated in the near future and thereby become their own “island universes” (Figure 4.1). Each of these gravitationally bound entities — dark matter halos — will attain a characteristic form for its density distribution (see Figure 4.4 and equation [5.2]). Finally, each bound structure will live at the center of its own island universe, and the metric of the surrounding space-time can be described by a line element of the form

$$ds^2 = -\left(1 - \eta_0 \alpha(\xi) - \chi^2 r^2\right) dt^2 + \left(1 - \eta_0 \beta(\xi) - \chi^2 r^2\right)^{-1} dr^2 + r^2 d\Omega^2, \quad (5.8)$$

where  $\eta_0 = 4\pi G\rho_0 r_S^2$ ,  $\xi = r/r_S$ , and where  $\alpha(\xi)$  and  $\beta(\xi)$  are shown in Figure 5.1. Astronomical entities (planets, stars, and galaxies) living within the universe will continue to evolve over much longer time scales (Adams & Laughlin, 1997; Dyson, 1979; Islam, 1977; Cirkovic, 2003), but space-time itself can be described by equation [5.8] for the vast majority of the total life of the universe.

The idea that some type of dark energy could affect the expansion of the universe dates back to Einstein’s original introduction of a cosmological constant. Although this idea has been called Einstein’s greatest blunder, the currently observed cosmic acceleration suggests that this concept may become one of Einstein’s greatest legacies. The motivation for the cosmological constant was to keep the cosmos static. In a twist of irony, the observed dark vacuum energy does not make the universe static, but rather drives it to expand at an accelerating rate. But even though the universe

expands and changes, and its constituent astrophysical objects age, this chapter shows that the local space-time metric does approach a “static” asymptotic form (equation [5.8]).

## CHAPTER 6

# Asymptotic Halo Mass

For cosmologies in which density fluctuations are seeded by an early inflationary period (e.g., Kolb & Turner, 1990), gravity acts during the era of cold dark matter domination to evolve a “cosmic web” of non-linear structures (e.g., Bond et al., 1996) that can be approximately described as a set of roughly spherical halos, each characterized by a mass  $M$ . Within a given cosmology, the spatial density, clustering properties, and internal structure of such halos evolve with time in ways that are becoming increasingly well understood (e.g., Cooray & Sheth, 2002; Kravtsov et al., 2004).

Oddly, the central element of this picture, the halo mass, is difficult to define. During the growth phase of the web, the mass distribution within a halo smoothly connects to the cosmological background of adjoining filaments, sheets, and voids. Any given halo is a mix of ‘old’ material that may be near hydrostatic and virial equilibrium and ‘new’ material gained from recent accretion. Although a radial gradient in the ratio of these two components is present, no clear edge that would allow a unique definition of mass separates them. In contrast, analytic collapse models based on spherical symmetry possess a well-defined outer shock or caustic surface (Bertschinger, 1985; Fillmore & Goldreich, 1984) that emerges at a characteristic density. These models have motivated several mass definitions based on enclosed density. White (2001) offers a recent discussion of these and other mass definitions applied to large-scale structure simulations.



In contrast to the present epoch, the far future of a  $\Lambda$ CDM universe provides an opportunity to cleanly define halo mass. In the relatively near cosmological future, merger activity comes to an effective end and dark matter halos evolve toward a dynamically quiet state (chapter 4; Nagamine & Loeb, 2003; see also the reviews of Adams & Laughlin, 1997; Cirkovic, 2003). In this chapter, we show that the phase-space configuration of dark matter halos reaches a well-behaved asymptotic state characterized by a single zero-velocity surface that uniquely defines the halo edge. Essentially all material internal to this surface is bound to and equilibrated within the halo, whereas material outside this surface is expanding away with the locally perturbed Hubble flow. In §6.1, we describe the simulation used and the mass measures employed in our analysis. Results are given in §6.2, followed by brief summary and discussion section (§6.3). Our mass and radius measurements assume a Hubble constant  $H_0 = 100h \text{ km s}^{-1} \text{ Mpc}^{-1}$  with  $h = 0.7$ .

## 6.1 Simulations and Mass Measures

We present results based on a simulation run with L-Gadget, a specialized version of the N-body code GADGET (Springel et al., 2001b). L-Gadget simulates only collisionless matter in a manner that optimizes cpu and memory resources. Our simulation models a patch of flat space in a  $\Lambda$ CDM universe with current matter density  $\Omega_m = 0.3$ , vacuum density  $\Omega_\Lambda = 0.7$ , and power spectrum normalization  $\sigma_8 = 0.9$ , values consistent with observational measurements of the CMB (Spergel et al., 2003).

The dark matter in a periodic cube of side length  $200h^{-1}\text{Mpc}$  is modeled by  $256^3$  particles of mass  $3.97 \times 10^{10}h^{-1}M_\odot$ . The simulation was started at redshift  $z = 19$  (scale factor  $a = 0.05$ ), evolved through the present epoch ( $a = 1$ ), and continued forward to  $a = 100$ . Although somewhat low, the starting redshift is in agreement with the analysis in Power et al. (2003) for our mass resolution (see figure 10 of their

paper). A gravitational softening parameter fixed at  $40h^{-1}\text{kpc}$  (in physical units) was used throughout the computation. The simulation was run on 8 dual-cpu nodes of a Beowulf cluster at the University of Michigan. A total of 300 outputs equally spaced in  $\log(a)$  were stored from the run. As the scale factor increases, the universe evolves from being matter dominated to vacuum energy dominated. We define  $a_{\text{eq}}$  as the epoch at which the energy densities in the two components are equal. For the chosen model, this transition occurs at  $a_{\text{eq}} = (\Omega_m/\Omega_\Lambda)^{1/3} = 0.75$ .

We identify dark matter halos using a standard percolation (or friends-of-friends, FOF) algorithm with linking length 0.15 times the inter-particle spacing. The halo center is identified as the most bound particle of the resulting group, and the halo velocity is defined as the center of mass velocity of the linked set of particles. At the end of the simulation this algorithm identified about 2900 halos with at least 500 particles. The largest halo at that time contains 83,600 particles, equivalent to  $3.3 \times 10^{15}h^{-1}M_\odot$ . In the analysis below, we measure ensemble properties using the 400 most massive halos, the smallest of which contains 3,000 particles.

The FOF algorithm defines halo centers about which we measure several enclosed mass scales. The first mass scale is  $M_{200}$ , the mass contained within a sphere of radius  $r_{200}$  that encloses a mean density 200 times the critical density  $\rho_c(a)$  at the epoch of interest. In addition, a so-called virial mass  $M_{\text{vir}}$  (within  $r_{\text{vir}}$ ) is defined to enclose a mean density  $\Delta_c(a)$  times the critical density, where  $\Delta_c(a)$  is an epoch-dependent threshold based on a simple, spherical collapse model (e.g., Eke et al., 1996).  $\Delta_c$  reaches a constant value of 20.4 as  $\Omega_m(a) \rightarrow 0$ . A third mass scale  $M_{180b}$  is defined by a mean enclosed density of 180 times the *background* mass density  $\rho_m(a)$ . Two body relaxation is not anticipated to affect these halos substantially. We have performed an analysis similar to that of Power et al. (2003) which indicates that at late times halos of this mass are stable to well within  $0.1r_{200}$ .

## 6.2 Results

Previous studies (chapter 4; Nagamine & Loeb, 2003) have shown that large-scale structure quickly approaches a stable configuration in the future deSitter phase of a  $\Lambda$ CDM cosmology. Mergers and accretion slow dramatically after the scale factor exceeds  $a = 2 - 3$ , signifying the end of the dynamically active stage of the cosmic web. The change in dynamical activity, from active to absent, is apparent in the reduced phase-space density  $f(r, v_r)$  of halos as shown in Figure 6.1. This figure plots the proper radial velocity  $v_r$  against distance from the halo center  $r$  for an ensemble average of the 400 most massive halos using  $r_{200}$  and  $v_{200} = \sqrt{GM_{200}/r_{200}}$  as scale variables.

Figure 6.1a shows the conditional probability  $p(v_r | r) = f(r, v_r)/\rho(r)$  for these 400 halos at  $a = 1$ . The solid line gives the mean radial velocity, while the grey scale regions delimit velocities containing 40%, 60%, 80%, 95%, and 99% of the material at each radius. This ensemble average phase space density can be divided into three principal regions: i) an inner hydrostatic core ( $\langle v_r \rangle = 0$ ) that is relatively well relaxed; ii) an intermediate accretion envelope ( $\langle v_r \rangle < 0$ ) containing two opposing streams of material, one on its first inward journey toward the halo center and the other passing outward after pericentric passage; and iii) an outflow region ( $\langle v_r \rangle > 0$ ) dominated by the locally perturbed Hubble flow. Nearly all of the material in regions i) and ii) is gravitationally bound to the halo (a modest fraction of material within  $r_{200}$  can be scattered out of a halo, see figure 4.3) while essentially all of region iii) is unbound. The characteristic scale that separates the outflow and accretion regions is often called the turnaround radius  $r_{\text{ta}}$  (Gunn & Gott, 1972), a term motivated by spherical models of expanding mass shells. We call the radius that separates the two interior zones the hydrostatic radius  $r_{\text{hs}}$  and measure its value using a threshold condition for the binned, mean radial velocity. Starting from the interior, we identify  $r_{\text{hs}}$  as the minimum radius at which  $|\langle v_r \rangle / v_{200}| > 0.1$ . The turnaround radius is identified

in the same manner, identifying the maximum radius at which  $|\langle v_r \rangle / v_{200}| < 0.1$ . At  $a = 1$ , the values of these characteristic radii are  $r_{\text{hs}} = 0.70r_{200}$  and  $r_{\text{ta}} = 3.3r_{200}$  and are marked by the vertical dashed lines in Figure 6.1a.

The averaging process used to create the density in Figure 6.1a blends the effects of substructures within individual halos, especially in the hydrostatic region. At a given radius, this region has a nearly Gaussian distribution of radial velocities with zero mean, signatures of hydrostatic and virial equilibrium. Due to the presence of pairs of massive clusters, the outflow region for the ensemble profile has a rather broad dispersion. The fact that the distribution of radial velocities for the outflow region is more sharply peaked than in the virialized region indicates that the surrounding regions generally contain halos that are less massive than those of our high-mass selected sample.

The situation in the far future is markedly different from the present. Figure 6.1b shows the ensemble phase-space density at  $a = 100$ . The most striking changes are the disappearance of the accretion region and the dramatic cooling of the outflow region due to the Hubble expansion. Here,  $r_{\text{hs}}$  and  $r_{\text{ta}}$  have merged to form a single zero-velocity surface at  $r_{\text{halo}} = 4.5r_{200}$ , represented by the dashed vertical line. In addition, relatively few nearby halos are present to disrupt the outflow stream. Neighboring halos that existed at  $a = 1$  have either merged or been pulled away in the deSitter expansion. Although not shown here, the phase-space density of the single most massive halo at  $a = 100$  is nearly identical to the ensemble averaged profile. Because mergers cease long before  $a = 100$ , the substructure present within any individual halo has several dynamical times to relax via tidal stripping, phase mixing, and dynamical friction (see figure 4.3 for a comparison with the phase-space distributions for individual halos).

The elimination of the accretion region at  $a = 100$  is accompanied by an expansion of the hydrostatic region. Figure 6.1c shows the evolution of the average  $v_r/v_{200}$ . The

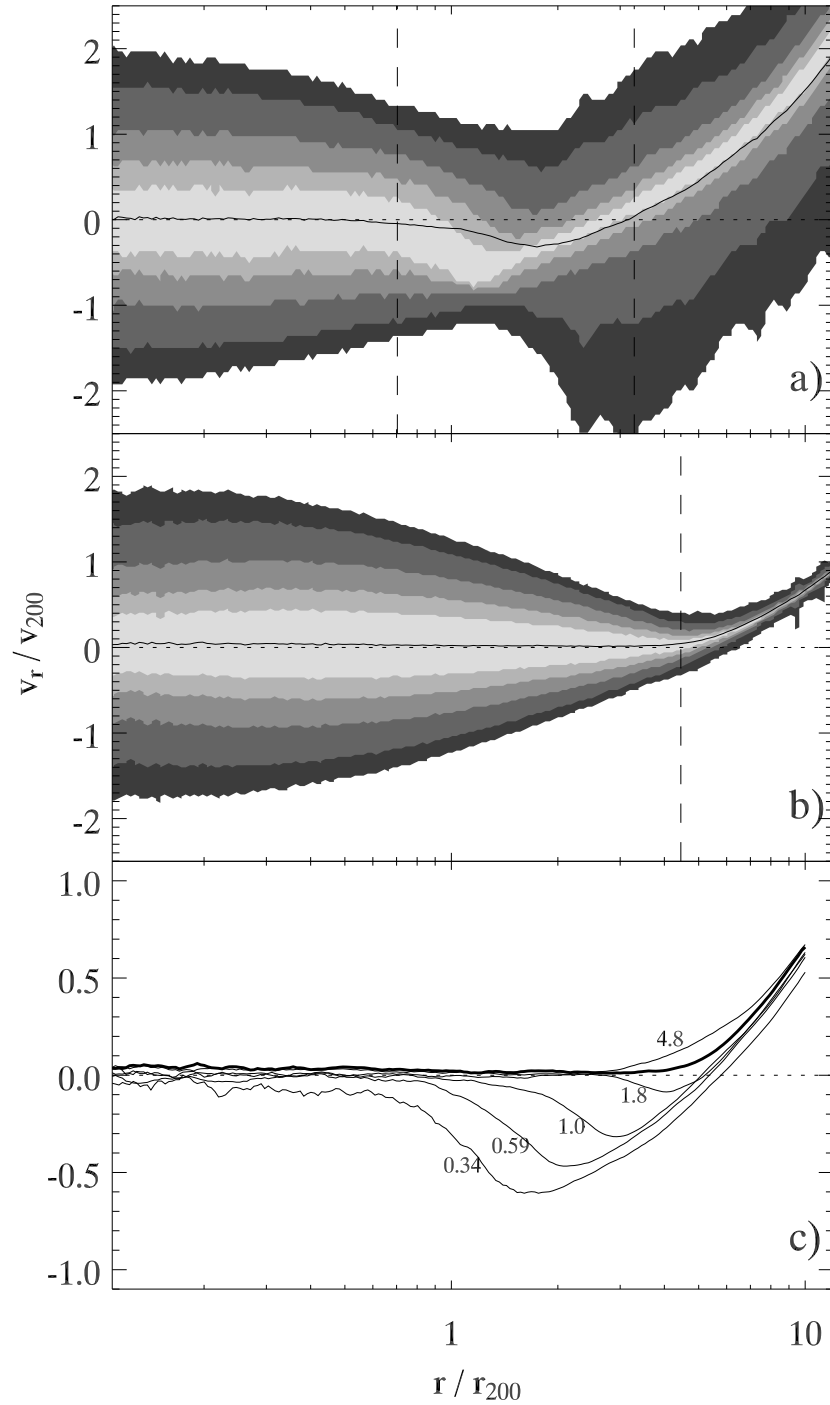


**Figure 6.1.** The distribution of dark matter radial velocities as a function of distance from the halo center. The top two panels show the conditional phase-space density  $p(v_r|r)$  as a function of radius for the ensemble of 400 largest halos at the present epoch (a) and for the future when  $a = 100$  (b). The solid line shows the mean velocity as a function of radius; the grey scale indicates the regions enclosing 40, 60, 80, 95, and 99 percent of the particle population as specified by  $p(v_r|r)$ ; the vertical lines represent the zero-velocity surfaces. Panel (c) shows the mean radial velocity for an ensemble of halos at epochs  $a = 0.34, 0.59, 1.0, 1.8,$  and  $4.8$ , with the bold line representing the function at  $a = 100$ .

bold curve shows the final profile at  $a = 100$ ; the thinner curves depict the epochs  $a = 0.34, 0.59, 1.0, 1.8,$  and  $4.8$ . The extent of the accretion region decreases with time as  $r_{\text{hs}}/r_{200}$  grows and  $r_{\text{ta}}/r_{200}$  slightly shrinks. Note also that there is an expulsion epoch at  $a = 4.8$ , shortly after mergers have ended. At this time,  $v_r/v_{200}$  is somewhat larger than its asymptotic value in the range  $r/r_{200} = 3 - 8$  because the unbound particles from the final mergers are being ejected.

The time evolution of this transition is presented in Figure 6.2. As before, we show ensemble behavior of the 400 most massive halos selected at  $a=100$ , with halos at earlier epochs restricted to the most massive progenitors of this final population (where most massive progenitor is defined to be the halo with the largest  $M_{\text{FOF}}$  that contributes at least 20% of its particles to its descendant). For each halo and epoch, we identify the physical values of the characteristic radii,  $(r_{\text{hs}}, r_{\text{ta}}, r_{200}, r_{\text{vir}}, r_{180b})$  along with the respective enclosed masses. To determine  $r_{\text{hs}}$  and  $r_{\text{ta}}$  for each halo, we first time smooth the individual profile by co-adding the halo configuration over seven consecutive outputs. We then measure  $r_{\text{ta}}$  using a linear extrapolation of the outflow over a factor of six in  $v_r$ , starting at the radius  $r = 10\text{Mpc}$  and working inward. Applying a threshold (as above) instead of extrapolating produces somewhat larger values for  $r_{\text{ta}}$ , but causes only a small change in the values for  $M_{\text{ta}}$ . We choose the extrapolation method because it provides less noisy estimates during the early phase of active halo growth. The hydrostatic region,  $r_{\text{hs}}$  is measured using a threshold technique on the mean radial velocity measured in radial bins, identical to the method used for Figure 6.1. We use logarithmically spaced bins, 30 per decade, and identify  $r_{\text{hs}}$  as the radius at which  $|v_r|/v_{\text{ta}} > 0.1$ ,  $v_{\text{ta}} = \sqrt{GM_{\text{ta}}/r_{\text{ta}}}$ . Typically,  $v_{\text{ta}} \sim 0.7v_{200}$ .

Figure 6.2 shows the time evolution of the mean physical radii and enclosed masses for the different measures. During the early Einstein-deSitter phase,  $a \ll a_{\text{eq}}$ , the sizes defined by mean interior densities  $r_{200}$ ,  $r_{\text{vir}}$  and  $r_{180b}$  are similar, whereas the hydrostatic boundary  $r_{\text{hs}}$  lies somewhat interior to  $r_{200}$  and  $r_{\text{vir}}$ . The turnaround ra-

dius  $r_{\text{ta}}$  lies well beyond these scales while the growth of linear perturbations remains robust.

The interior scales diverge at epochs  $a > a_{\text{eq}}$  when vacuum effects dominate. As linear growth stagnates, large-scale mass density fluctuations  $\delta\rho/\bar{\rho}$  become frozen into the background. Continuity of the density field implies that the mean size  $r_{180b}$  (defined relative to the mean matter density) becomes constant in the comoving frame, so the physical size grows exponentially in time. In contrast, the ensemble mean  $r_{200}$  rapidly approaches its asymptotic value, following  $r_{200}(a) = r_{200,\infty} [1 - \exp(-(a/a_{\text{eq}})^{1.5})]$  at late times, with  $r_{200,\infty} = 1.2$  Mpc for this high-mass sample. This fit is shown for  $a > a_{\text{eq}}$  by the dot-long-dashed line in Figure 6.2b.

The value of  $r_{\text{vir}}$  relaxes less quickly, due to the decline in the variable threshold  $\Delta_c(a)$  as the scale factor increases. The enclosed masses  $M_{200}$ ,  $M_{\text{vir}}$  and  $M_{180b}$  grow monotonically until reaching 99% of their asymptotic limits at  $a = 2.9$ , 8.6 and 13.6, respectively, corresponding to ages of 32, 52 and 60 Gyr. The innermost mass scale  $M_{200}$  experiences a slight decline at late epochs,  $\propto (0.00045 \pm 0.00015)\ln(a)$ , but it is not clear whether this drift is physical or numerical.

The hydrostatic boundary  $r_{\text{hs}}$  tracks  $r_{180b}$  until  $a \sim 2$ , then slows its growth and relaxes toward an asymptotic value. The turnaround radius also grows rapidly until  $a \simeq 1.5$ , then declines until  $a \sim 5$ , and increases slowly thereafter. The decline in size and enclosed mass from the peak until  $a \sim 5$  arises from a change from infall to outflow in the accretion regime lying between  $r_{\text{hs}}$  and  $r_{\text{ta}}$ , as indicated by the outflow enhancement at this epoch in Figure 6.1c. At  $a \sim 1$ , accretion just outside the hydrostatic boundary drops dramatically. After a crossing time, the modest mass fraction of this accreted material that is scattered to unbound orbits emerges at radii  $r > r_{\text{hs}}$  with positive radial velocity at  $a \sim 2-5$ . This material escapes from the halos, but we have not investigated its ultimate fate. Presumably, some fraction emerges as the cores of stripped sub-halos that remain self-bound, whereas the remainder may

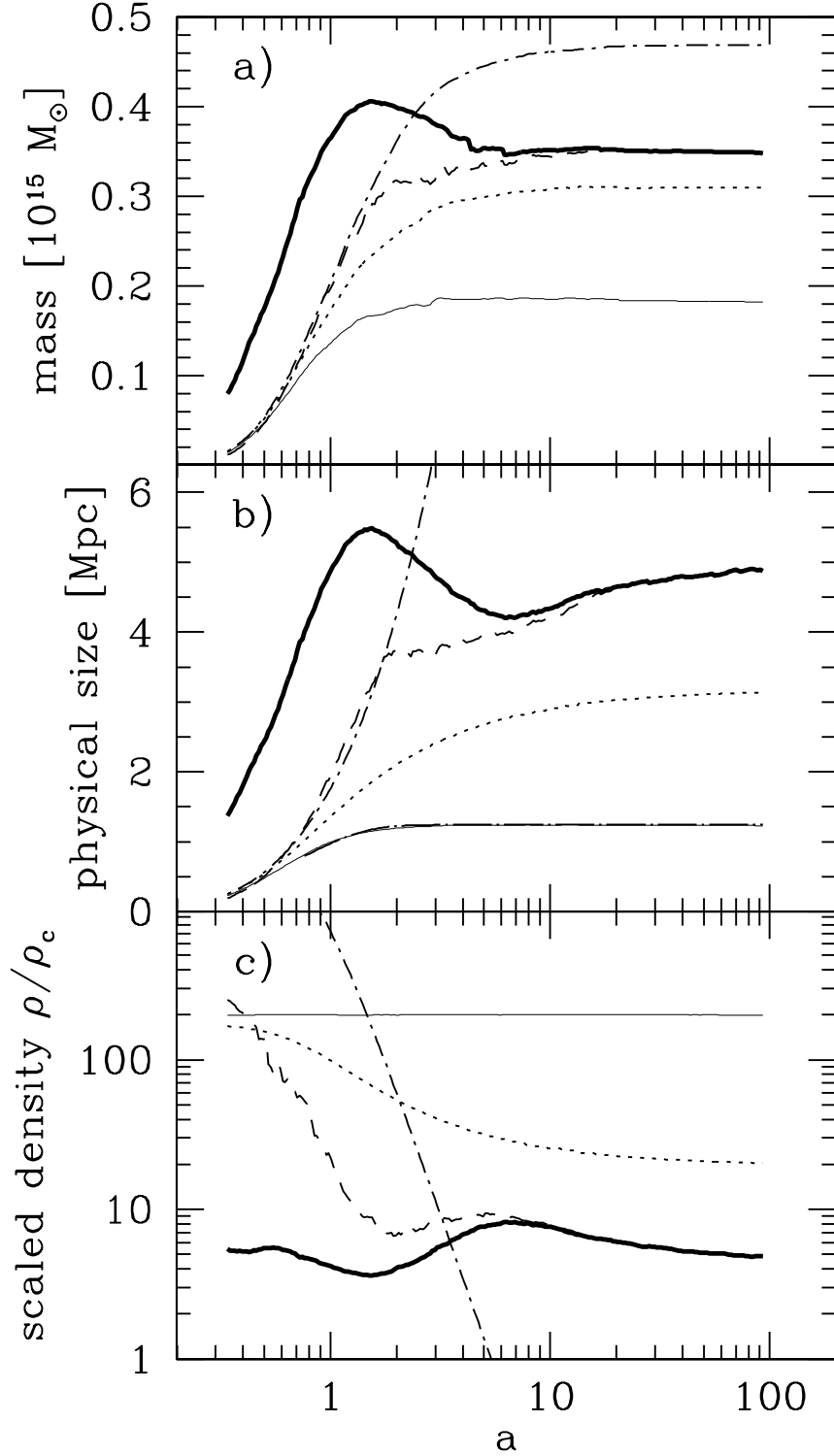


**Figure 6.2.** Comparison of mass and radial scales for the progenitors of the 400 most massive halos identified at the end of the computation. The four panels show the scale factor dependence of (a) mean masses; (b) mean physical sizes; (c) enclosed densities relative to the critical value. The line styles indicate the different mass measures:  $M_{\text{ta}}$  (bold);  $M_{\text{hs}}$  (dashed);  $M_{200}$  (solid);  $M_{\text{vir}}$  (dotted); and  $M_{180b}$  (dot-dashed). The line styles for the radial scales are analogous. In panel (b), the dot-long-dashed curves show the asymptotic form of  $r_{200}$  (see text) for  $a > a_{\text{eq}} = 0.75$ .



emerge sufficiently tenuous and hot that it never collapses into a halo of cosmologically interesting mass. Future studies using higher resolution experiments are needed to address this question.

For test particles in Hubble flow around a halo of mass  $M$ , the outer zero-velocity surface location can be estimated using a Newtonian binding energy, with the result (Equation [4.11])  $r \simeq (M/10^{12}M_{\odot})^{1/3}\text{Mpc}$ . Applying this estimate using the mean asymptotic halo mass in Figure 6.2a yields a value of 5Mpc, close to the asymptotic mean size shown in Figure 6.2b. We caution that the values of  $r_{\text{hs}}$  and  $r_{\text{ta}}$  are sensitive at the  $\sim 10\%$  level to the choice of threshold and/or the interpolation scheme used to locate the zero-crossing. However, the steep behavior of the density profile near the boundary ( $\rho \propto r^{-\gamma}$ ,  $\gamma \gg 4$ ) leads to a much smaller uncertainty ( $\lesssim 2\%$ ) in enclosed mass.

The merging of the turnaround and hydrostatic scales signals the end of high mass structure formation, and therefore the end of the growth phase of the cosmic web. Thereafter, halos maintain a fixed physical size and the morphology of the cosmic web, when viewed in the comoving frame at a density threshold near critical, becomes less of a web and more an increasingly fine spray of droplets (see chapter 4 and Nagamine & Loeb, 2003). From Figure 6.2a, the ratio  $M_{\text{hs}}/M_{\text{ta}}$  reaches 99% of its asymptotic value at  $a = 7.4$  ( $a/a_{\text{eq}} = 10$ ). At epochs beyond  $10a_{\text{eq}}$ , we can clearly define the (ultimate) halo mass as  $M_{\text{halo}} \equiv M_{\text{hs}} = M_{\text{ta}}$ , i.e., *the mass enclosed within the single zero-velocity surface is the ultimate halo mass*.

Figure 6.2c shows that the turnaround/ultimate halo mass is defined by a density threshold  $\rho_{\text{halo}}$  relative to critical that lies at all times within a factor of two range spanning  $\sim (5 - 10)\rho_{\text{c}}(a)$ . The threshold at early times lies close to the canonical  $9\pi^2/16 = 5.5$  value expected from spherical collapse in an Einstein-deSitter universe (Peebles, 1980). After  $a_{\text{eq}}$ , the ratio  $\rho_{\text{halo}}/\rho_{\text{c}}(a)$  first drops while the mean halo mass peaks, then climbs to  $\sim 10$  during the period  $a/a_{\text{eq}} = 2 - 10$  when the mean halo mass

drops. At late times,  $\rho_{\text{halo}}$  is declining weakly, and its asymptotic limit, although not well determined by this simulation, is only about 12% shy of the canonical value.

While the gap between  $r_{180b}$  and  $r_{\text{halo}}$  expands exponentially in the far future, the enclosed mass ratio converges to  $M_{180b}/M_{\text{halo}} \approx 1.35$ . While thresholding with respect to the background mass density extends beyond the halo edge at late times, the scales defined relative to the critical density pick out mass shells interior to the halo:  $M_{\text{vir}} = 0.89 \pm 0.04 M_{\text{halo}}$  and  $M_{200} = 0.52 \pm 0.04 M_{\text{halo}}$ . These particular values are sensitive to the asymptotic form of the radial density distribution. Considering the forward evolution of the halos, the distribution of  $M_{\text{halo}}(100)/M_{200}(1)$  is log-normal with a high-end tail containing about 10% of the population. The peak of the log-normal is at mass ratio 2.2 with dispersion 0.38. The tail starts around the  $2\sigma$  point and extends out to  $M_{\text{halo}}(100)/M_{200}(1) = 100$ , with the largest factors representing smaller objects that have merged with the most massive halos.

Figure 6.3 shows the mean radial profile obtained at  $a = 100$  from the stacked ensemble of the 400 most massive halos. We use  $r_{200}$  as the scale radius, but results are similar when other characteristic scales are used. The light solid line shows the mean profile while the heavy solid line shows the profile for material bound to each halo, using specific energy  $E/m = v^2/2 - GM(< r)/r + (4\pi/3)G\rho_{\Lambda}r^2$  (with  $v$  and  $r$  the proper velocity and radius, respectively). The bound material is well fit over the entire halo volume by a truncated Hernquist (1990) profile

$$\rho(r) = \frac{\rho_0}{(r/r_c)(1+r/r_c)^3} e^{-(r/\hat{r}_{\text{halo}})^{5.6}}, \quad (6.1)$$

with characteristic radius  $r_c = 0.62r_{200}$  and truncation scale  $\hat{r}_{\text{halo}} = 4.6r_{200}$ . The latter measure of halo size agrees extremely well with the value of  $4.5r_{200}$  obtained from the ensemble average zero-velocity surface. This fit has a least-square error of about 12%. For comparison, an NFW profile  $\rho(r) = 4\rho_s(r/r_s)^{-1}[1 + (r/r_s)]^{-2}$  (Navarro et al., 1996b), obtained by fitting within  $r_{200}$  is shown in Figure 6.3 by the dotted line. The profile with  $r_s = 0.25r_{200}$  fits the inner regions of the halo well, but it is

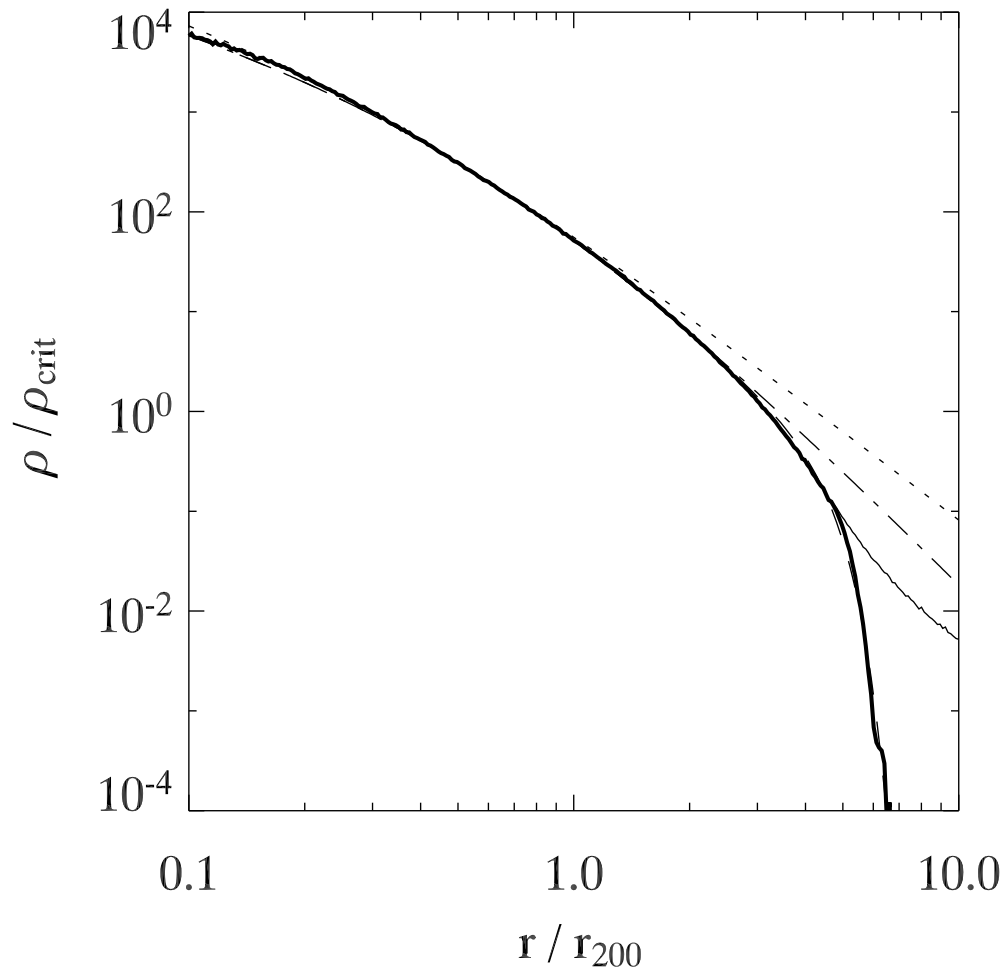


**Figure 6.3.** The asymptotic form of the density distribution for dark matter halos. The solid curves show the density profile for an ensemble average of the 400 most massive halos in the simulation at scale factor  $a = 100$ . The upper solid curve shows the total density as a function of radius, whereas the lower solid curve includes only the bound particles. The dotted curve shows the best fit NFW profile. The dot-dashed curve shows the best fit Hernquist profile, and the dashed curve represents a truncated Hernquist profile (see equation [6.1]).

much too shallow beyond  $r_{200}$ , overestimating the halo density at  $r_{\text{halo}}$  by an order of magnitude. Note that simple scaling for the evolution of the concentration proposed by Bullock et al. (2001),  $c_{\text{vir}}(a) \sim a$ , breaks down as the growth rate becomes constant and the profile out to  $r_{\text{vir}}$  becomes fixed after a few Hubble times.

### 6.3 Summary

From a large N-body simulation that follows the long term evolution of collisionless structure in a  $\Lambda$ CDM cosmology, we have examined the ultimate approach to equilibrium for a sample of 400 massive halos with final mean mass  $3.5 \times 10^{14} M_{\odot}$ . During the matter-dominated era ( $a \lesssim a_{\text{eq}} = 0.75$ ), the radial phase-space structure of the halos is complex, consisting of an inner hydrostatic region, an intermediate accretion zone, and an exterior region that expands with the perturbed Hubble flow. During the interval  $a_{\text{eq}} \leq a \leq 10a_{\text{eq}}$ , accretion shuts down and the intermediate region is briefly dominated by outflow rather than infall. For  $a \gtrsim 10a_{\text{eq}}$ , the intermediate region disappears, and the hydrostatic and turnaround scales merge to form a single zero-velocity surface that provides an unambiguous definition of halo mass.

The existence of multiple mass scales commonly used in the literature to describe clusters is a direct reflection of the complexity of the accretion region during the growth phase of structure. This work illuminates the evolving relationships between the hydrostatic and turnaround scales of halos and scales defined by mean interior density thresholds. Although thresholding with respect to the background density ( $M_{180b}$ ) has advantages for calculating the halo space density (Jenkins et al., 2001), its use to describe future structure is compromised by our finding that  $M_{180b}$  exceeds the asymptotic halo mass for  $a \gtrsim 2$ . Masses defined by thresholds relative to the critical density converge to well-defined values. For  $a \gtrsim 10 a_{\text{eq}}$ , we find  $M_{\text{halo}} = 1.1M_{\text{vir}} = 1.9M_{200}$ .

Using only bound material, the ensemble mean density profile of the 400 most

massive halos is well fit by a modified Hernquist model, with scale radius  $0.62r_{200}$  and truncation radius  $4.6r_{200}$  (equation [6.1]). The origin of this particular form, as well as other issues such as its dependence on halo mass and its extension to an ellipsoidal description, remains to be investigated.

## CHAPTER 7

### Small Scale Power and Accretion History

In this chapter, we continue along the lines of chapter 6 where we analyzed the equilibrium structure of halos. The previous chapter concentrated on the question of how exactly one defines a halo. The next open question is to understand why non-linear structure takes the form that it does — a form that, as discussed in section 2.4.2 has been predicted by simulations and confirmed, more or less, by observational data. In particular, we would like to know how and why dark matter halos attain a nearly universal form for their density profiles, as first described by Navarro, Frenk, & White 1997 (hereafter NFW). One aspect of this issue is understanding the importance of the method of mass accretion: How much does the final structure depend on accreting mass as virialized clumps as opposed to a continuum of diffuse material and how effectively does violent relaxation (Lynden-Bell, 1967) erase the memory of this accretion process.

As discussed in section 2.3.1, the basic process for the buildup of structure in our cold dark matter (CDM) dominated universe is the hierarchical merging of collapsed structures (see, e.g., Press & Schechter, 1974; Aarseth et al., 1979; Blumenthal et al., 1984; Davis et al., 1985). This process creates small halos early in the universe which merge with each other while accreting material from their surroundings, eventually creating the large cluster-sized structures of today through a “bottom up” process.

For a time it was thought that light neutrinos might dominate the mass density, forcing galaxy formation to occur through a “top down” process (e.g., Bond & Szalay,

1983). In such a hot dark matter model, perturbations on small scales are washed out by free streaming, preventing the formation of the early low-mass seeds of hierarchical structure formation. Dark matter halos still form, but the first objects are large cluster-mass halos (Zel'Dovich, 1970; Doroshkevich & Zeldovich, 1975). While popular in the 1970's because simulations reproduced the outline of the cosmic web that surveys were just beginning to map out (Thompson & Gregory, 1978), hot dark matter models have been ruled out based on observations of the galaxy distribution (White et al., 1983). Tuning the free-streaming mass-scale leads to WDM possibilities which suppress density perturbations below some (typically dwarf galaxy sized) scale. The most immediate effect of this suppression is to reduce the number of small halos and subhalos existing in large halos. Several numerical studies of WDM cosmologies have been carried out (e.g., Evrard & Crone, 1992; Avila-Reese et al., 2001; Bode et al., 2001; Colín et al., 2000; White & Croft, 2000; Knebe et al., 2002, 2003), mostly in an attempt to explain the apparent lack of substructure in our local group as compared to predictions from  $\Lambda$ CDM simulations.

CDM and hierarchical merging have emerged as the standard paradigm for structure formation and the key ingredients in setting the distribution of dark matter halos. Although there have been a number of studies on the role of mass accretion on setting internal halo properties (see, e.g., Avila-Reese et al., 1998; Huss et al., 1999; Wechsler et al., 2002), the exact impact of this process remains unclear. While some studies indicate that the accretion of substructures plays a significant role in setting the inner slope of the radial halo density profile (Ma & Boylan-Kolchin, 2004), simulations of monolithic collapse events in WDM cosmologies and other forms of non-hierarchical growth produce halos with global properties unchanged relative to similar structures in CDM cosmologies (Evrard & Crone, 1992; Moore et al., 1999b; Alvarez et al., 2003). By truncating the initial power spectrum in an otherwise CDM simulation at some scale  $k_c$  (with corresponding mass scale  $M_c = 4/3\pi^4 k_c^{-3} \bar{\rho}$ ), one can mimic

WDM cosmologies and test the importance of hierarchical growth for establishing halo structure. Compared to the CDM model, where mass is continually accreted in dense clumps, WDM cosmologies have an early period of monolithic collapse, where large halos form out of a smooth background and relax with many fewer disruptions due to merger events. If the halo is in a dense enough region, this initial collapse is followed by hierarchical accretion. Previous simulations of this process (Moore et al., 1999b; Bode et al., 2001; Avila-Reese et al., 2001) have shown that the resulting density profile is virtually unchanged for halos well above the truncation scale.

Halos in a WDM cosmology are effectively a re-scaled versions of the first halos expected in a CDM cosmology. Most physical CDM candidates (i.e., SUSY-LSP's) have some intrinsic velocity dispersion, washing out perturbations on very small scales (much smaller than we are able to simulate on cosmological scales), effectively truncating the power spectrum at some very large  $k$  (see Diemand et al., 2005; Gao et al., 2005 for discussions of such simulations). In this manner, studying WDM cosmologies can provide clues to the earliest collapse of CDM structures.

To gain insight into the question of the origin of the internal structure of dark matter halos, we have performed a set of simulations of cosmic structure, using both a standard  $\Lambda$ CDM and truncated WDM-like power spectra. Simulations are run into the far future, allowing halos to relax toward equilibrium configurations. Our numerical simulations are described in §7.1. In §7.2, we compare the differences in the halo distribution for the two cosmologies, concentrating on the mass function, evolution of the power spectrum, and the formation of WDM halos with mass well below the truncation scale. In §7.3 we compare the internal structure of the halos in the two cosmologies, including the mass accretion histories (MAHs), the distribution of substructure, and the halo density profiles. Results and their implications are summarized and discussed in §7.4.



## 7.1 Simulations

We simulate the formation of dark matter halos in  $\Lambda$ -dominated CDM and WDM-like cosmologies with a suite of dark matter N-body simulations using the publicly available TreePM code Gadget 2.0 (Springel, 2005). We use two  $\Lambda$ CDM and WDM simulations with different mass resolutions for a total of four large-scale cosmological simulations. The simulation pairs at each mass resolution were created with the same initial phases so that the the large-scale environment would be unchanged. All simulations model a patch of space in a flat universe with current matter density  $\Omega_{m,0} = 0.3$ , vacuum density  $\Omega_{\Lambda} = 0.7$ , Hubble parameter  $H_0 = 70 \text{ km s}^{-1} \text{ Mpc}^{-1}$  and power spectrum normalization  $\sigma_8 = 0.9$ , values consistent with the first year release of WMAP measurements of the CMB power spectrum (Spergel et al., 2003). The lower resolution simulations model periodic cubes of side length  $L = 200h^{-1} \text{ Mpc}$  containing  $N_p = 256^3$  particles of mass  $3.97 \times 10^{10} h^{-1} M_{\odot}$  and gravitational softening length  $\epsilon_p = 40h^{-1} \text{ kpc}$ . The higher resolution simulations use cubes of side length  $L = 50h^{-1} \text{ Mpc}$ , containing  $256^3$  particles with mass  $6.20 \times 10^8 h^{-1} M_{\odot}$  and softening length  $\epsilon_p = 10h^{-1} \text{ kpc}$ . The softening scales quoted here correspond to their values at the present epoch and are held constant in comoving space for  $a < 1$ , but become physical lengths for  $a > 1$  to prevent structures from being over-softened due to the exponential increase in  $a$  during the deSitter phase. The initial conditions were generated by perturbing particles initially in a glass configuration. A glass configuration is a distribution of particles such that the net force acting on each particle is zero. Table 7.1 lists these simulation parameters. All simulations were started at redshift  $z = 19$  (scale factor  $a = 0.05$ ) and were run into the far future,  $a = 100$ . Although the starting redshift is somewhat late, it is consistent with the analysis by Power et al. (2003) for a simulation of our resolution, and should present no problem for the late-time results we are primarily concerned with. We store a total of 300 outputs equally spaced in  $\log(a)$  for each simulation. At  $a = 100$  the universe is about  $64h^{-1} \text{ Gyr}$  old

**Table 7.1.** Simulation parameters:

$L[h^{-1}\text{Mpc}]$	$M_p[h^{-1}M_\odot]$	$\epsilon_p[h^{-1}\text{Mpc}]$	$N_p$
200	$3.97 \times 10^{10}$	0.04	$256^3$
50	$6.20 \times 10^8$	0.01	$256^3$

and structure formation has preceded to completion in a  $\Lambda$ CDM cosmology (Busha et al., 2003; Nagamine & Loeb, 2003). The simulations were run on 16 nodes of a dual-Opteron Beowulf cluster at the University of Michigan.

The initial power spectrum for our CDM simulations was set using `CMBFAST` (Seljak & Zaldarriaga, 1996) in accordance with WMAP year 1 data (Spergel et al., 2003). Our second, WDM-like, simulation used a truncated version of this initial power spectrum,

$$P_t(k) = CP_0(k)e^{-(k/k_c)^2}, \quad (7.1)$$

where  $k_c$  is the truncation scale and  $C$  a normalization coefficient that allows us to set  $\sigma_8$ . Figure 7.1 plots our input spectra, with  $P_0$  as the solid line and  $P_t$  as the dashed line. For our simulations, we choose a truncation scale of  $k_c = 0.511h\text{Mpc}^{-1}$ , which corresponds to a mass scale of  $M_c = 8.09 \times 10^{13}h^{-1}M_\odot$  (2037 particles for our lower resolution simulations and 130,396 at the higher resolution). This truncated spectrum was re-normalized to  $\sigma_8 = 0.9$  so that high mass halo abundances would be similar. As noted earlier, phase information was retained for each resolution pair, resulting in similar large scale structures (Figure 7.2) and allowing us to identify corresponding halos in the two cosmologies.

Equation (7.1) represents a transfer function that differs from the standard transfer function for a WDM cosmology. Generally, the mass of the WDM particle,  $m_W$  sets a free streaming length,  $R_f = 0.2(\Omega_W h^2)^{1/3}(m_W/1\text{keV})^{-4/3}\text{Mpc}$  (Sommer-Larsen & Dolgov, 2001), which approximates the WDM power spectrum through the relation

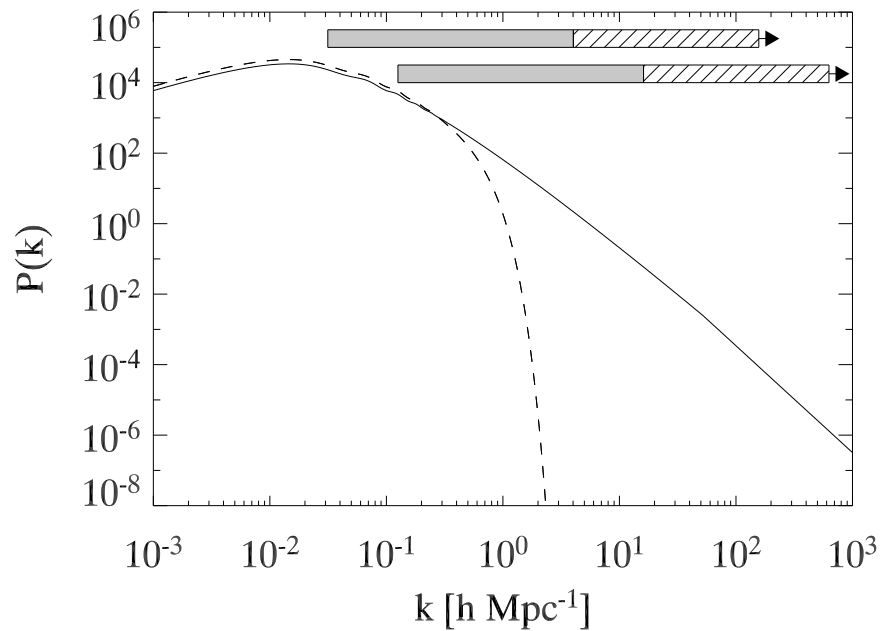


**Figure 7.1.** The input power spectra for the  $\Lambda$ CDM (solid line) and WDM (dashed line) simulations. The  $\Lambda$ CDM spectrum is calculated using `CMBFAST`. The WDM model adds an exponential cutoff to the  $\Lambda$ CDM model at a mass scale of  $8.09 \times 10^{13} h^{-1} M_{\odot}$ . Both spectra were normalized so that  $\sigma_8 = 0.9$ . The light gray boxes represent the range between the fundamental and Nyquist frequencies for the small (top) and large (bottom) volume runs. The hatched-line boxes show the range between the Nyquist and softening frequencies for  $a \leq 1$ . For  $a > 1$ , the softening is constant in the physical frame and its corresponding wavenumber grows with  $k \propto a$  in this comoving representation.

(Bardeen et al., 1986)

$$P_{WDM}(k) = \exp \left[ -kR_f - (kR_f)^2 \right] P_{CDM}(k). \quad (7.2)$$

This spectrum has a slightly more gradual cutoff than equation (7.1). It should be noted that we refer to our truncated models as “WDM” cosmologies even though they were not created using this transfer function. For reference, our truncated model most closely approximates a WDM cosmology with  $m_{WDM} = 0.13\text{keV}$  and  $R_f = 1.6\text{Mpc}$ .

The evolution of the resulting density fields of the simulations are shown in Figures 7.2 and 7.3. Figure 7.2 shows a slice the comoving density field from our smaller volume CDM and WDM simulations at  $a = 0.3, 1, 3,$  and  $100$ . The differences between these two models are striking, especially at  $a = 0.3$ , where the CDM cosmology exhibits a well-formed web with an abundance of small halos. The WDM cosmology, in contrast, has a mostly uniform density, with only one visible halo and a handful of weak filamentary structures making up the cosmic web. A clear cosmic web does rapidly develop in the WDM simulation, however, and by  $a = 1$  similar large scale structures are present in both cosmologies, even though there is a strong suppression of small halos in the WDM filaments. By  $a = 3$ , the large scale density field is set and undergoes little evolution from  $a = 3$  to  $100$ . Once the cosmological constant becomes dominant the growth function saturates, ending halo formation and freezing the comoving web. Halos continue to contract in this comoving picture, and by  $a = 100$  they consist of small, tightly bound knots along and at the intersection of filaments.

Figure 7.3 shows the evolution of the density field in a fixed physical region. Here, we focus on the evolution of a particular CDM halo with mass  $M_{200} = 5.38 \times 10^{14} h^{-1} M_{\odot}$  and its counterpart in the WDM cosmology (see §7.2.3). While much of the late time growth is identical (such as the major merger around  $a = 1$ ), the initial formation processes differ substantially. At  $a = 0.3$ , there are many low mass CDM

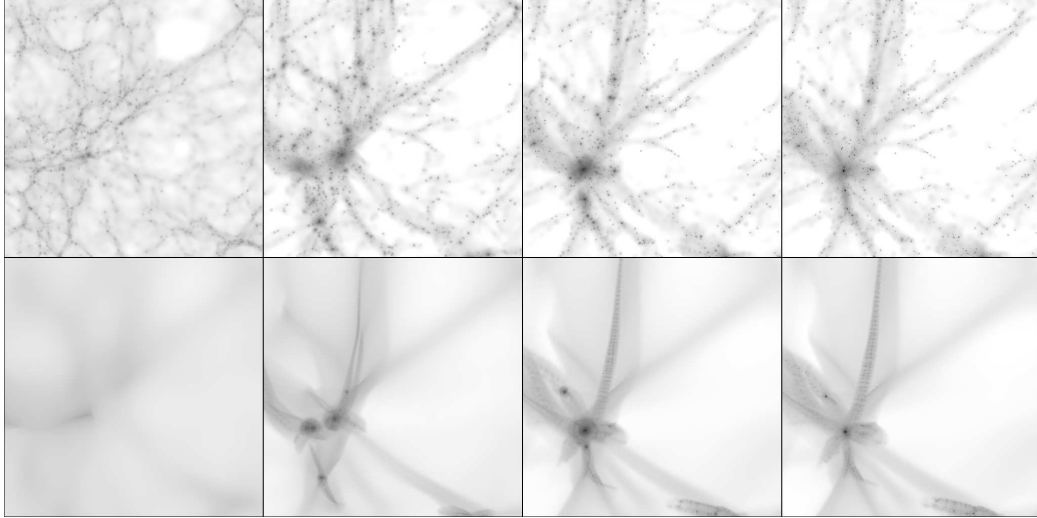


**Figure 7.2.** The density fields of comoving slices of the cosmic web at  $a = 0.3, 1, 3,$  and  $100$  (columns, left to right) of a  $\Lambda$ CDM (top) and WDM (bottom) cosmologies from our small volume simulations. The side length for each image is  $35h^{-1}\text{Mpc}$ , with thickness  $5h^{-1}\text{Mpc}$ . The grey-scale is proportional to  $\log(\rho/\bar{\rho})$ .

progenitor halos present, while the WDM halo looks like a weak (uncollapsed) perturbation in an otherwise smooth background. This difference is manifest throughout all plotted epochs by the persistent lack of substructure in the WDM halo at the three later epochs.

One way to quantify the expected suppression of hierarchical buildup is to look at the critical mass scale,  $M_*(a)$ , where one expects a perturbation to go non-linear and collapse, defined through the relation

$$\sigma[M_*(a)] = \frac{\delta_c}{D(a)}. \quad (7.3)$$

Here,  $\sigma(M) = (2\pi)^{-3} \int_0^\infty P(k) \tilde{W}^2(M, k) d^3k$ ,  $\tilde{W}$  is the Fourier transformation of the top-hat window function,  $D(a)$  is the linear growth function, and  $\delta_c = 1.686$  is the linearly extrapolated criterion for collapse of an overdense perturbation in an  $\Omega_m = 1$  universe. (Press & Schechter, 1974; Peebles, 1980). The factor  $D(a)$  can be calculated numerically from the expression

$$D(a) \propto H(a) \int_0^a \frac{da'}{[a'H(a')]^3}, \quad (7.4)$$

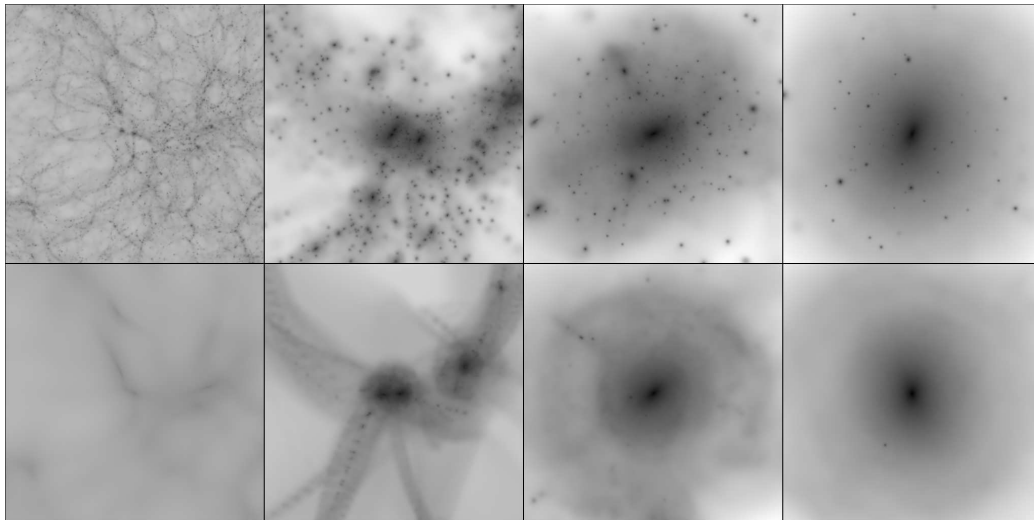


**Figure 7.3.** The density field around a large halo at  $a = 0.3, 1, 3,$  and  $100$  (columns, left to right) from our small volume simulations. The top row shows the largest halo from the  $\Lambda$ CDM cosmology ( $M_{200} = 5.38 \times 10^{14} h^{-1} M_{\odot}$  at  $a = 100$ ) and the bottom row shows the corresponding WDM halo ( $M_{200} = 5.24 \times 10^{14} h^{-1} M_{\odot}$  at  $a = 100$ ). The side length for each image is  $12 h^{-1} \text{Mpc}$ , with thickness  $6 h^{-1} \text{Mpc}$  in physical units. The grey-scale is proportional to  $\log(\rho/\rho_c)$ .

and is normalized such that  $D(1) = 1$ . The left panel of Figure 7.4 shows the amplitude of  $2\sigma(M)$  perturbations as a function of  $M$  at the present epoch. The horizontal dotted line shows the critical scale,  $\delta_c = 1.686$ . The right panel of Figure 7.4 shows the evolution of  $M_{2\sigma}(a)$  — the mass of a  $2\sigma$  perturbation that goes nonlinear as a function of cosmic time. In both cases, the solid line represents the full power spectrum model and the dashed line represents the truncated power spectrum model. We consider  $2\sigma$  perturbations because, in our WDM cosmology,  $1\sigma$  perturbations do not collapse until  $a = 1.33$  and are prevented from growing substantially by the cosmological constant. The normalization  $\sigma_8 = 0.9$  boosts the power at large mass ( $M > 10^{14} h^{-1} M_{\odot}$ ) in the WDM model relative to the CDM case and causes the largest perturbations to collapse slightly earlier and with larger asymptotic masses in the WDM model. We also expect no structures in the WDM cosmology for  $a < 0.4$ , agreeing with Figure 7.3 in which the most massive halo of the simulation has yet to form a coherent structure prior to this epoch.

Dark matter halos in our simulations are identified using a standard friends-of-

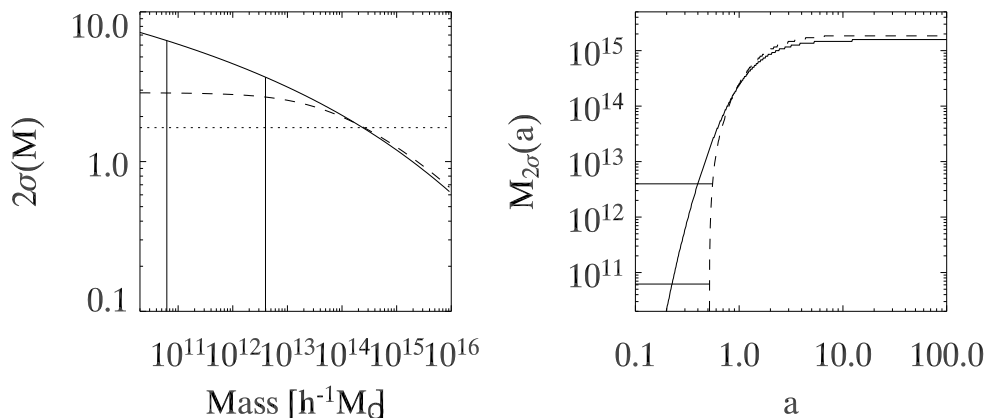


**Figure 7.4.** *Left:* Rare ( $2\sigma$ ) perturbation amplitude as a function of mass at  $a = 1$  for the  $\Lambda$ CDM (solid line) and WDM (dashed line) models. The vertical lines show the mass scales for 100 particles at the two resolutions. *Right:* Characteristic collapsed mass as a function of scale factor for the  $\Lambda$ CDM (solid line) and WDM (dashed line) cosmologies. The solid horizontal lines show the mass scales for 100 particles at the two resolutions.

friends (FOF) algorithm with linking length 0.15 times the inter-particle spacing. Halo centers are identified as the most bound particle of the resulting group. As a mass measure capable of spanning both early and late times we use  $M_{200}$ , the mass of all particles inside a sphere of radius  $r_{200}$  with over-density 200 times the critical density,  $\rho_c$ . In previous work, we found the  $M_{200}$  provides a good proxy for the asymptotic halo mass and is roughly half the value of the ultimate halo mass,  $M_{200} \simeq 0.5M_{halo}$  (Busha et al., 2005). The halo velocity is defined to be the center of mass velocity of all particles within  $r_{200}$ .

Subhalos were identified using the `SUBFIND` routine (Springel et al., 2001a). This routine works on top of an FOF group and identifies density maxima within halos from an SPH smoothing kernel that uses the distance to the 32<sup>nd</sup>-nearest neighbor to obtain local density estimates. Subhalos are then selected as locally overdense regions containing at least 20 bound particles. The largest subhalo identified by `SUBFIND` is actually the host halo of the FOF group. At  $a = 100$ , this host halo should correspond to the actual equilibrated halo as defined in Busha et al. (2005), minus any locally

bound subhalos. A comparison between these mass estimates shows good agreement, with the masses agreeing to within 1%.

Throughout this chapter, we use several scale radii. Halo sizes are defined using  $r_{200}$  (see above) and  $r_{halo}$ , the spherical radius containing all bound particles (which is only defined for  $a \gtrsim 5$ , see Busha et al. 2005). Additionally, we fit NFW and Hernquist density profiles to our halos,

$$\rho_{NFW} = \frac{4\rho_s}{r/r_s(1+r/r_s)^2}, \quad (7.5)$$

$$\rho_{Hern} = \frac{\rho_0}{r/r_c(1+r/r_c)^3}, \quad (7.6)$$

which adds the scales  $r_s$  (the radius where the best fit NFW profile has logarithmic slope  $-2$ ) and  $r_c$  (where the best fit Hernquist profile has slope  $-2.5$ ). Generally, we find that  $r_{halo} = 4.6r_{200}$  and  $r_s = 0.4r_c$  (see §7.3.3, Busha et al., 2005).

## 7.2 Comparisons Of The Dark Matter Distribution

In this section we compare properties of the distribution of dark matter halos in our simulations, including the evolution of the power spectrum, the halo mass function, the correspondence between CDM and WDM halos, and the formation of WDM halos below the truncation scale.

### 7.2.1 Evolution of the Power Spectrum

Figure 7.5 shows the evolution of the power spectrum for all four of our simulations at the epochs  $a = 0.3, 1, 3,$  and  $100$ . The solid lines represent the CDM cosmologies and the dashed lines the WDM spectrum. The power spectrum is shown in dimensionless units,  $\Delta^2(k) \propto k^3 P(k)$ . Power spectra for the large and small volume simulations are combined, allowing us to probe a larger range in  $k$ . The arrows represent the softening lengths for the large and small volume simulations at the plotted epoch. The collapse of non-linear structure creates substantial power beyond the Nyquist frequency, which we measure using the tiling method of Jenkins et al. (1998). The



spectra are plotted from the fundamental simulation frequency out to a wavenumber where the shot noise of a Poisson distribution of particles becomes comparable to the measured power.

At  $a = 0.3$ , when non-linear structure formation is in its early stages, the power spectrum of the WDM model is heavily truncated above  $k_c$ . By the present epoch, much of this suppression has disappeared due to power transfer from collapsing structures, and the WDM cosmology matches the CDM model almost perfectly at low and intermediate wavenumber, up to an order of magnitude above  $k_c$ . Relatively little happens to the power spectrum beyond  $a = 1$ . As noted earlier, the dominance of  $\Lambda$  halts the growth of structure beyond  $a \sim 3$  and causes the power spectrum to freeze after only a modest amount of additional evolution. Since Figure 7.5 plots the power spectrum in comoving space, beyond  $a = 1$  the expansion of the universe transfers power to larger scales with no real change in the shape of the spectrum. For most of the measurable range,  $0.1 < k < 100h\text{Mpc}^{-1}$ , the power spectrum is well characterized by the expected power law,  $\Delta^2 \propto k^3$ , caused by the freezing of structure in an expanding universe. Collapse, however, has not managed to elevate the WDM power spectrum up to that of the CDM model at all scales by  $a = 3$ , and a small suppression of power at the highest wavenumbers persists at  $a = 100$ . This suppression is due to the lack of low mass halos. If we measure the halo power the spectrum using only halos with  $M_{200} > M_c$  we recover spectra that are identical at the few percent level, which indicates that the distribution of halos on scales greater than  $M_c$  is statistically unchanged.

The evolution of the power spectrum in WDM cosmologies was studied previously by White & Croft (2000) and Knebe et al. (2002). These studies present results similar to ours. By  $a \sim 0.5$ , non-linear collapse has boosted the truncated portion of the power spectrum substantially, agreeing with a  $\Lambda\text{CDM}$  model for  $k < 10h\text{Mpc}^{-1}$  with only a slight suppression for larger  $k$ .

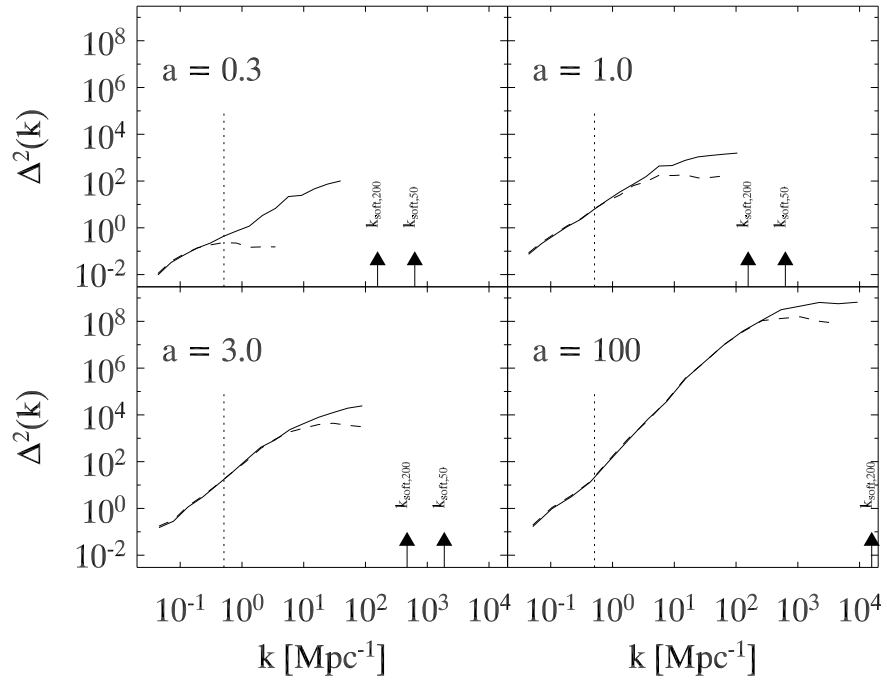


**Figure 7.5.** The evolution of the power spectrum for halos in CDM (solid lines) and WDM (dashed lines) cosmologies. The spectra are shown at  $a = 0.3, 1, 3,$  and  $100$ . Power spectra from the small and large volume realizations are laid on top of each other. The dotted vertical lines represent the truncation scale,  $k_c$ , and the arrows show the softening scales for the large and small volume runs. The spectra are plotted from the fundamental frequency of the simulation volume to the frequency where the shot noise becomes comparable to the measured power, generally  $\sim 0.1k_{soft}$ .

### 7.2.2 Mass Function

Figure 7.6 shows the mass function for our large volume CDM and WDM simulations at  $a = 1$  and 100. Errors are calculated assuming Poisson statistics and the vertical dotted line is the truncation scale,  $M_c$ . Here, the dark lines represent the  $\Lambda$ CDM model and the light lines the WDM version. For comparison, the figure also shows the Jenkins Mass Functions (JMF, Jenkins et al. (2001)) as dashed lines. The JMF is defined via

$$\frac{dn_{JMF}(M, a)}{d \ln(M)} = A \frac{\bar{\rho}}{M} \frac{d \ln \sigma^{-1}(M, a)}{d \ln M} \times \exp[-|\ln \sigma^{-1}(M, a) + B|^\epsilon], \quad (7.7)$$

where  $A, B$ , and  $\epsilon$  are fitting parameters. Two mass values are used in this plot to compare with published JMF parameters: FOF masses with a linking length  $b = 0.164$  (upper curves, Jenkins et al. 2001) and  $M_{200}$  from a spherical overdensity groupfinder (SO, lower curves, Evrard et al. 2002). The fitting parameters are listed in Table 7.2. For the  $a = 100$  spherical overdensity JMF, we used the  $\Omega_M = 0$  parameters from Evrard et al. (2002). Although not shown, The Sheth & Tormen mass function with published parameters (Sheth & Tormen, 1999) agrees quite well with the JMF FOF mass function at all epochs. While the agreement between FOF masses in the CDM cosmology and equation (7.7) is good for  $a = 1$ , a substantial mass excess is present in the mass range  $10^{13} < M_{\text{FOF}} < 5 \times 10^{14} h^{-1} M_\odot$  at  $a = 100$ . Additional simulations of this cosmology confirm that this excess is significant and not a result of one particular realization. The use for FOF masses in measuring the mass function does create difficulties in the far future because the FOF groupfinder identifies isosurfaces relative to the background matter density, which is dropping rapidly from the exponential expansion. Compared with the critical density, the physical density isosurface identified by a FOF groupfinder is  $\rho_{\text{FOF}} = [(a^6 \Omega_{m,0}) / (\Omega_{m,0} + a^3 \Omega_{\Lambda,0})] b^{-3} \rho_{\text{crit}}$ . By  $a = 3$ ,  $\rho_{\text{FOF}} = 3.5 \rho_{\text{crit}}$ , which includes a substantial amount of material outside the virialized

**Table 7.2.** Mass Function Parameters:

Mass Function	$A$	$B$	$\epsilon$
JMF – FOF(0.164)	0.301	0.64	3.88
JMF – SO(200, $a = 1$ )	0.220	0.73	3.86
JMF – SO(200, $a = 100$ )	0.199	0.76	3.90

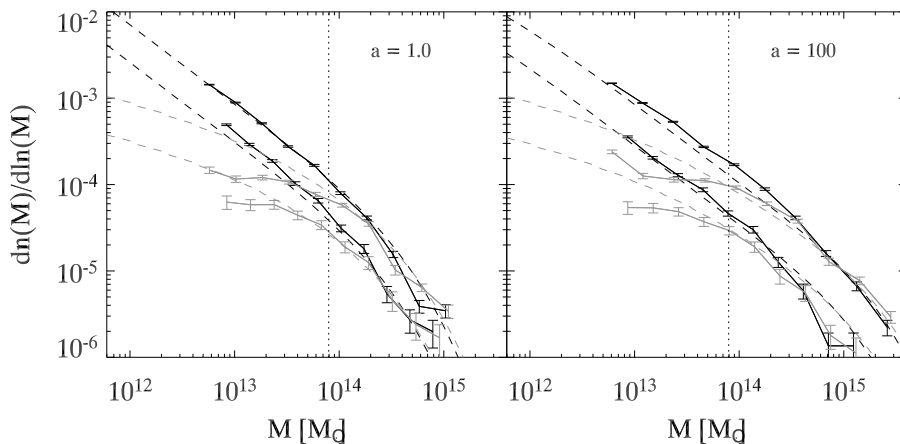


**Figure 7.6.** The mass function for the CDM and WDM cosmologies (dark and light curves) at  $a = 1$  and 100 for our larger volume simulations. The upper curves show the FOF(0.164) mass function and the lower curves the SO(200) mass function. The FOF(0.164) function has been offset vertically for clarity. The dashed lines represent the Jenkins et al. (2001) models. The vertical dotted line shows the truncation scale. Error bars assume Poisson statistics.

region of a halo that is unbound and being pulled away by the Hubble flow (Busha et al., 2005). At late epochs,  $M_{\text{FOF}}$  is a poor proxy for the actual (virialized) mass of a halo. The  $M_{200}$  mass function, however, does not suffer from this defect. The  $a = 1$  result agrees with Evrard et al. (2002) to  $\sim 20\%$  in number, approximately the quoted statistical accuracy. The parameters are slightly off, however, due to insufficient mass resolution of the simulation. The  $a = 100$  mass function does provide a substantially better agreement than the FOF mass function, fitting to within about  $2\sigma$  at all masses.

The mass function for the WDM cosmology exhibits a striking suppression for low masses, beginning slightly above the the truncation scale,  $M_c$  (dotted vertical

line). An unexpected upturn appears in the WDM model at the lowest masses ( $\lesssim 50$  particles) for FOF halos. Bode et al. (2001) and Knebe et al. (2002) claim that this behavior is a result of physical halos forming through fragmentation from Jeans instability. However, such an upturn is not present in the SO mass function and we show evidence in Appendix C that it is actually a numerical artifact of the FOF groupfinder. We have also calculated JMF and ST fits for our WDM cosmology, which do not fit as well as in the  $\Lambda$ CDM cosmology. Both the JMF and ST mass functions strongly over-predict the abundance of halos with masses  $M < M_c$ . The poor fit in the range  $10^{13}h^{-1}M_\odot < M < 8 \times 10^{13}h^{-1}M_\odot$  should not be surprising because equation (7.7) was motivated by a perturbation collapse threshold, similar to the Press-Schechter (1974) model, which uses spherical collapse to determine a collapse epoch. As we discuss in the next section, WDM halos with mass below  $M_c$  form out of larger mass perturbations that do not follow this model, at odds with the assumptions of Press-Schechter.

### 7.2.3 Halo Correspondence

Because we used the same phases in constructing the initial conditions, we can cross-match halos in the CDM and WDM cosmologies using a Lagrangian scheme. We select a FOF halo in one cosmology (usually  $\Lambda$ CDM) and identify for the largest halo in the other cosmology containing at least 50% of particles of the selected halo. When starting with a  $\Lambda$ CDM halo, we don't allow any two WDM halos to be identified with the same  $\Lambda$ CDM halo. This simple method is robust for massive systems, and corresponding halos are found for 98% of all halos with  $M_{200} > M_c = 8.08 \times 10^{13}h^{-1}M_\odot$ . The “missing” halos are lost because the smoothing of the power spectrum causes distinct halos in the CDM cosmology to form as single halos in the WDM run. Our requirement that each WDM halo have only a single CDM counterpart prevents all but the most massive of these CDM halos from having a WDM counterpart. If

we relax this correspondence requirement, all CDM halos with  $M_{FOF} > M_c$  have WDM counterparts. Figure 7.7 shows the masses of corresponding halos in the WDM and  $\Lambda$ CDM models. At higher masses ( $M_{200} > 2M_c$ ) the masses are similar,  $M_{200,CDM} \approx M_{200,WDM}$  with about a 6% scatter. As the mass falls below the truncation scale,  $M_c$ , the WDM halos become less and less massive relative to their CDM counterparts, eventually disappearing altogether. There are a few extreme outliers from the general relationship. Halos with a low  $M_{WDM}/M_{CDM}$  (the three halos with  $M_{200,CDM} \sim 10^{14}h^{-1}M_\odot$  and  $M_{200,WDM} \sim 2 \times 10^{12}h^{-1}M_\odot$ ) are CDM halos in filaments that never completely collapse in the WDM cosmology. Most of their particles are located in a spray along the filament, but there is a small WDM halo in the filament with  $\sim 90\%$  of its members in the CDM halo. The halo with the  $M_{200,WDM} \gg M_{200,CDM}$  is a rare occurrence where many small CDM halos ( $\sim 10$ ) were merged into a single, much more massive halo in the WDM cosmology.

Also plotted in Figure 7.7 is the completeness function for identifying corresponding halos. Virtually all  $\Lambda$ CDM halos with  $M_{200} > M_c$  have corresponding WDM halos, but the completeness function drops very rapidly for  $M_{200} < M_c$ , the mass range where halo formation is strongly suppressed.

#### 7.2.4 Sub-Truncation Scale Halos In WDM

One surprising observation from the WDM simulations is that many halos form with mass scale  $M_{200}$  well below the truncation scale,  $M_c = 8.08 \times 10^{13}h^{-1}M_\odot$ . Although physical halos with  $M_{200} < M_c$  account for only a few percent of all collapsed mass, these halos represent a substantial population by number. Previous WDM studies have addressed the formation of sub-truncation scale halos and reached different conclusions. Bode et al. (2001) and Knebe et al. (2003) claim that such halos form through top-down fragmentation, while Avila-Reese et al. (2001) and Götz & Sommer-Larsen (2003) argue that small halos originate due to finite resolution ef-

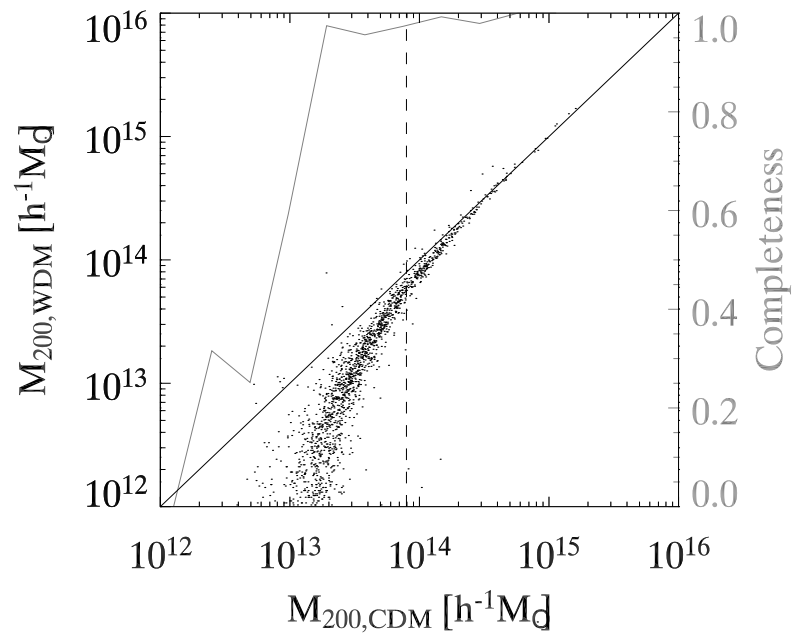


**Figure 7.7.** A comparison of the  $M_{200}$  values for corresponding halos in the  $\Lambda$ CDM and WDM runs at  $a = 100$ . The dashed vertical line denotes the truncation scale. Halos with  $M_{200} \gg M_c$  have roughly the same mass with a scatter of about 6%. The light line shows the probability for finding a WDM halo corresponding to a  $\Lambda$ CDM halo of a given mass.

fects and grid like initial conditions. Wang & White (2007) go further, arguing that finite resolution effects are also responsible for creating such halos even with glass initial conditions. We argue that some of this confusion between fragmentation and numerical artifacts arises because these halos generally fall into two categories: more massive halos ( $M_{200} \lesssim M_c$ ) are genuine structures whose statistical presence is predicted from collapse models such as Bertschinger (2006), who calculated that the mass fraction should have a long tail extending well below the dark matter free streaming length. At very low masses, however, our FOF mass function turns up dramatically (see Figures 7.6 and C.1), and we argue that halos below this mass are numerical artifacts. In this section, we discuss the presence and formation of the more massive sub-truncation halos and argue that they form through the “incomplete” collapse of massive density perturbations due to limitations of the spherical collapse model. We discuss the smaller halos, which we argue are numerical artifacts, in Appendix C.

In order to understand the formation of more massive sub-truncation scale halos, we first note that all WDM halos in the small volume realization with  $M_{200} > 0.0125M_c = 10^{12}h^{-1}M_\odot$  have CDM counterparts, indicating that these halos are not purely numerical artifacts resulting from our truncation process. Additionally, examining the initial conditions and measuring  $M_{pert}$ , the mass of the perturbation out of which the halo forms calculated with the spherical collapse model, we see that  $M_{pert}$  is never less than  $0.2 \times 10^{14} = 0.25M_c$ . From these observations we note that, as discussed in Katz et al. (1993), there is not a strong relation between  $M_{halo}$ , the final collapsed halo mass, and  $M_{pert}$ . A given perturbation is free to collapse to a halo of any size such that  $M_{halo} \lesssim M_{pert}$ . Indeed, we see the same effect for a similar number of halos in this mass range in our CDM cosmology. This now raises the (cosmology-independent) question, why do some large perturbations collapse to objects with  $M_{halo} \ll M_{pert}$ ? Certainly this could be related to the top-down fragmentation method proposed by Bode et al. (2001) and Knebe et al. (2003), but



this implies that  $\sim 20\%$  of CDM halos also form top-down instead of hierarchically. The answer appears to come from a shortcoming of the spherical collapse picture we have presented above. Cosmological collapse actually proceeds triaxially, and strains caused by the surrounding environment typically have a significant effect (Bond & Myers, 1996; Sheth et al., 2001). In particular, the collapse threshold in the ellipsoidal collapse model,  $\delta_{ec}$ , grows with the ellipticity of the initial perturbation, causing non-spherical perturbations to collapse to lower masses than predicted from the spherical collapse model. A comparison of the ellipticity of halos with  $M_{pert} < M_{halo}$  with those that collapse to  $M_{pert} = M_{halo}$  reveals that the halos that don't collapse to their spherical model prediction have initial strains that are several times larger than those that do collapse to their spherical prediction. From this we conclude that all halos with mass greater than the upturn in the mass fraction (see Appendix C) are not numerical in nature but arise through the standard halo formation process.

### 7.3 Comparison Of Halo Properties

This section compares properties of individual halos in our CDM and WDM cosmologies. In particular, we focus on the mass accretion histories, subhalo abundance, and density profiles. In spite of some substantial and fundamental differences in the first two properties, the form of the radial density profiles is unchanged between the CDM and WDM cosmologies. Furthermore, halo concentrations follow the same relation with formation epoch in both models.

#### 7.3.1 Mass Accretion Histories

One property for which we expect a clear difference between CDM and WDM halos is the halo mass accretion history (MAH). For the WDM model, the reduced merger activity should result in a smoother MAH since mass is primarily accreted in the form of diffuse material. The suppression of power at large  $k$  also alters the characteristic

collapse mass at low mass/early times (Figure 7.4, right panel). The implication is that halos will form later and more rapidly (in the sense of a larger  $d \ln M / d \ln a$ ) in a WDM cosmology.

The MAHs are measured using a halo’s most massive progenitor, where a progenitor is any halo at a preceding output in which at least 50% of the FOF particles end up in the subsequent halo. When comparing halos between the two runs, we first select CDM halos from a given mass range and then select either their WDM counterparts (as in Figure 7.7, ignoring CDM halos that have no match) or WDM halos from the same mass ranges. These selection methods are nearly degenerate for  $M_{200} > M_c$ , as shown in Figure 7.7. At lower CDM halo masses  $M_{200, \text{WDM}}$  is strongly suppressed, so the selection methods differ substantially. Generally, we prefer to consider halos of similar final masses so that we do not have to worry about halos with no counterpart.

Figure 7.8 shows MAHs for three halos in the full run (solid curves) and their matched halos in the truncated run (dashed curves). These individual halos were selected from our smaller volume run to have  $M_{200} \gg M_c$  (dark curves),  $M_{200} \sim M_c$  (medium curves), and  $M_{200} < M_c$  (light curves) at  $a = 100$  in the CDM cosmology. As expected, the halos in the truncated model have smoother MAHs during the initial halo growth phase and form slightly later, with these effects becoming more pronounced for smaller halos. The overall shape of the MAHs for the halos with  $M_{200} \gg M_c$  is remarkably similar. While the most massive halo in the truncated model has no progenitor before  $a \sim 0.2$ , it grows quickly and catches up with the CDM halo by  $a = 0.7$ . Afterwards, the two halos evolve almost identically, even undergoing the same major mergers around  $a = 1$  and 2. These mergers happen slightly earlier in the WDM cosmology due to the increase in power at this scale from our normalization  $\sigma_8 = 0.9$ , which effectively starts the “cosmic clock” for these large halos at a later time. In contrast with the these late-time similarities, the MAHs at

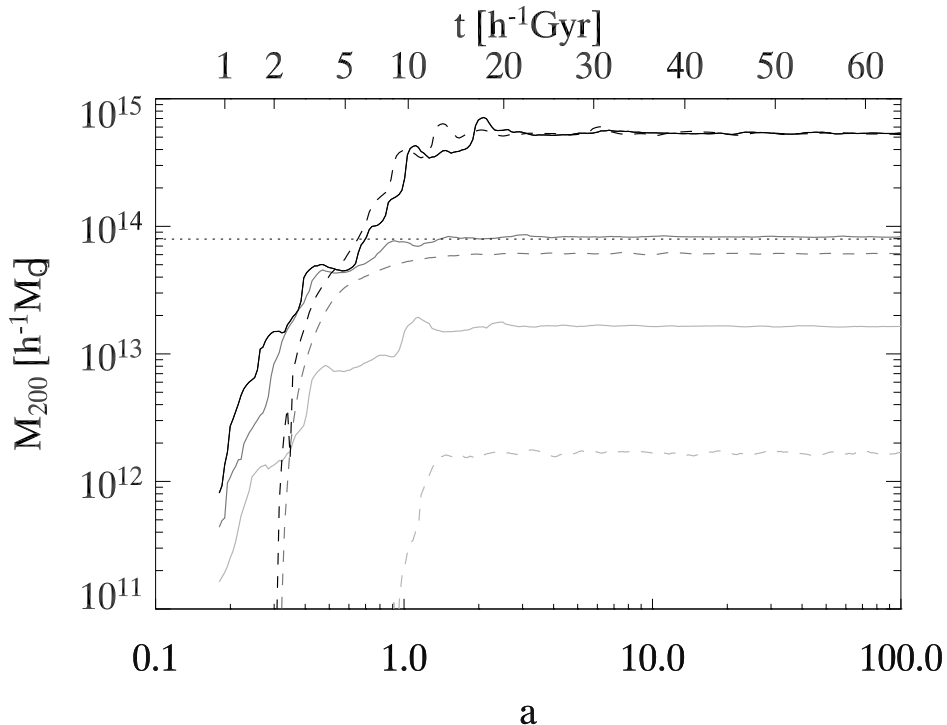


**Figure 7.8.** The accretion history for three individual halos in the full run (solid curves) and their corresponding halos in the truncated run (dotted curves). The halos were selected with  $M_{200} \gg M_c$  (dark curves),  $M_{200} \sim M_c$  (medium curves), and  $M_{200} \ll M_c$  (light curves) in the run with the full power spectrum. The dotted horizontal line represents  $M_c$ .

$a < 0.7$  are substantially different. In the WDM scenario, a large mass perturbation will collapse more or less as a unit, as soon as it goes non-linear. This collapse creates a phase of smooth, rapid mass growth with  $d \ln M_{\text{WDM}}/d \ln a \gg d \ln M_{\text{CDM}}/d \ln a$ . Once the halo reaches  $M_{200, \text{WDM}} \approx M_c$ , the halo is the approximate size of its counterpart in the CDM cosmology and  $d \ln M_{200}/d \ln a$  drops to match the rate of the CDM halo. The WDM halo then begins to accrete mass as already-collapsed clumps in a quasi-hierarchical fashion. The CDM halos with masses  $M_{200} \leq M_c$ , in contrast, have corresponding WDM halos that never accrete mass in virialized clumps. The MAHs of such WDM halos are much smoother and accrete the bulk of their mass in a single period of rapid accretion.

Figure 7.9 shows ensemble average MAHs for halos from our large volume simulations. Here, the diamonds represent CDM halos and the crosses are WDM ha-

los. Halos from different mass ranges have been offset in time to make the figure more readable. Both the CDM and WDM halos are selected to lie in the mass ranges  $M_{200} = (2 - 4) \times 10^{13} h^{-1} M_{\odot}$ ,  $(0.5 - 1.3) \times 10^{14} h^{-1} M_{\odot}$ , and  $> 4 \times 10^{14} h^{-1} M_{\odot}$  at  $a = 100$ . Figure 7.9 shows many of the same trends observed in Figure 7.8. For the most massive halos, the two cosmologies again show mass equality around  $M_{200,\text{CDM}} \approx M_{200,\text{WDM}} \approx M_c$ , with the WDM halos accreting mass significantly faster before this time. For  $M_{200} \leq M_c$ , WDM halos form later and more rapidly than CDM halos with similar mass. Also shown in the bottom panel of this figure are the growth rates,  $d \ln(M_{200})/d \ln(a)$ , of the halos and their fits to equation (7.9).

Wechsler et al. (2002, hereafter W02) proposed a fitting formula for the MAH of a halo up to the present epoch of the form

$$M(a) = M_0 e^{-(a_c, w02/a_0) S (a_0/a - 1)}. \quad (7.8)$$

The free parameter  $S$  in this equation is used only in defining  $a_{c,w02}$ , the creation epoch for the halo, when  $d \ln M/d \ln a = S$ . We choose to follow their convention and adopt  $S = 2$ . This formula is fit to our CDM MAHs over the range  $a = 0.2 - 1.0$  (but continued out to  $a = 100$ ) and plotted as the dotted curves in Figure 7.9. In general, the fit is good for both CDM and WDM (not shown) models for  $a < 1$ , but overestimates halo masses by a factor of 2 in the CDM run and more than an order of magnitude for the WDM run at late times. If the fit is calculated for the full range,  $0.2 < a < 100$ , the late time asymptote is correct, but  $d \ln M_{200}/d \ln a$  is substantially lower than observed for either cosmology at all epochs. This behavior is probably an indirect result of the coincidence problem — the surprising observation that we live during the relatively short epoch where  $\Omega_M \approx \Omega_{\Lambda}$ . The fit works well for  $a < 1$ , even when calculated for just a fraction of the region and then extrapolated. Although equation (7.8) was created for halos in a  $\Lambda$ CDM universe,  $a = 1$  is not much later than the equality epoch,  $a_{eq} = 0.75$ , when  $\Omega_{m,0} = \Omega_{\Lambda}$ . Once  $\Lambda$  becomes the dominant component of the universe, the growth function quickly saturates and

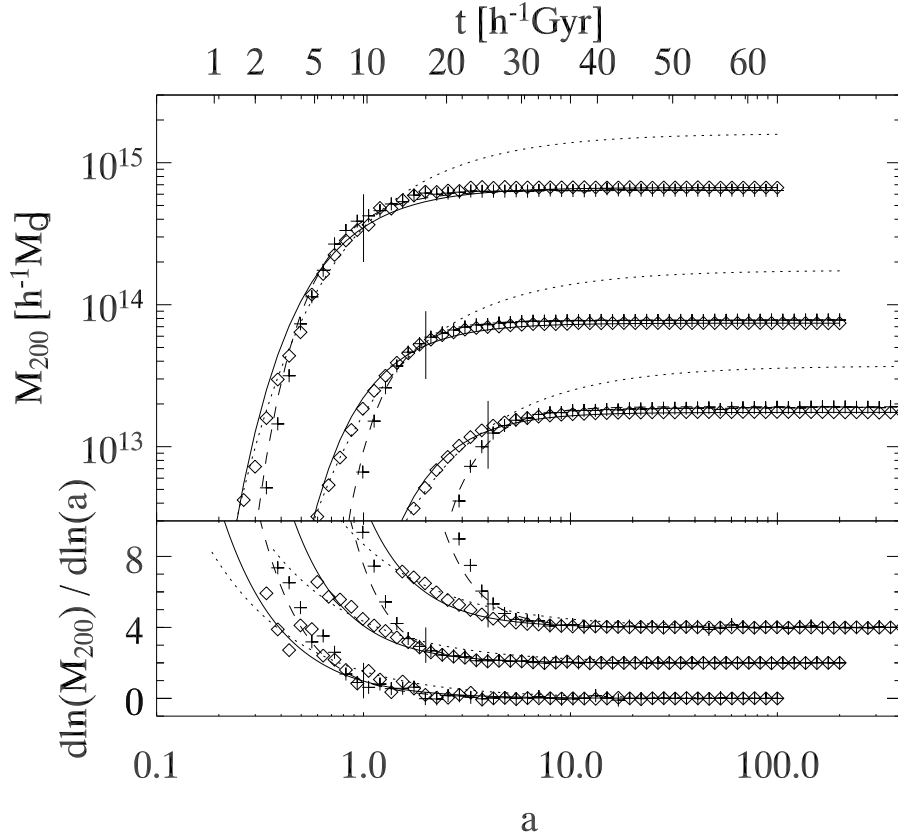


**Figure 7.9.** *Top Panel:* Average MAHs for CDM (diamonds) and WDM halos (plus symbols) from our large volume simulations. The halos are selected from the mass ranges  $M_{200} = (1 - 4) \times 10^{13}, (0.5 - 1.3) \times 10^{14}$ , and  $> 4 \times 10^{14} h^{-1} \text{Mpc}$ . The curves are offset in  $a$  by a factor of 2 (intermediate mass range) and 4 (low mass range) to make them easier to distinguish, but the short vertical lines represent  $a = 1$  for all mass ranges. The dotted curves are fits to equations (7.8) for the CDM halos and the solid and dashed curves are fits to equation (7.9) for the CDM and WDM cosmologies. *Bottom Panel:* The mass growth rates,  $d\ln(M_{200})/d\ln(a)$ , of the halos and plotted above and their fits to equation (7.9). Curves are offset in both the horizontal and vertical directions to make them more distinguishable.

halos cease to grow (Busha et al., 2005). Consequently, equation (7.8) approaches its asymptote much more slowly than halos feeling the full effects of a dominant cosmological constant. To capture the full histories in both cosmologies, we propose a generalization of the form

$$M(a) = M_0 e^{-(a_c/a_0)^\gamma \frac{S}{\gamma} ((a_0/a)^\gamma - 1)}, \quad (7.9)$$

where  $\gamma$  is the rate index which sets the mass growth rate through the relation  $d \ln M / d \ln a = S(a_c/a)^\gamma$ . This variable is introduced such that  $a_c$  is still the epoch where  $M(a)$  has a logarithmic slope of  $S$ , but  $\gamma$  sets how quickly a halo grows and asymptotes to its equilibrium mass. When  $\gamma = 1$  this generalized form reduces to equation (7.8). We expect to recover  $\gamma > 1$ , which corresponds to more rapid formation and faster asymptote behavior (see Figure 7.9)

The fits to equation (7.9) in Figure 7.9 (solid and dashed curves for CDM and WDM halos) closely follow the measured MAHs. They provide good agreement over all epochs and work equally well for both CDM and WDM halos. Although not shown, the errors for this fit are generally  $\lesssim 5 - 10\%$ , depending on the number of halos we average over. Figure 7.10 compares  $a_{c,W02}$ , from equation (7.8), and  $a_c$  from our modified form, equation (7.9), with dots representing halos from the large volume simulations, and crosses are from the small volume simulations. In the CDM cosmology (left panel),  $a_{c,W02} = 2.7a_c^{1.4}$  with a 27% scatter. The few WDM halos with  $a_{c,W02} < 1$  are also well described by this relation. In both cases, there are several halos with  $a_{c,W02} > 1$ . These are typically halos that first appear around  $a \geq 0.7$  and have rapid growth phases, powered either by major mergers or the collapse of a sub-truncation scale perturbation in the WDM cosmology. These formation epochs, based on equation (7.8), appear unphysical since they give formation epochs in the period of exponential expansion when halo growth has stopped. Equation (7.9) resolves this issue by increasing the halo rate index, resulting in a substantially lowered  $a_c$  which pulls these halos significantly above the measured linear relation between  $a_c$

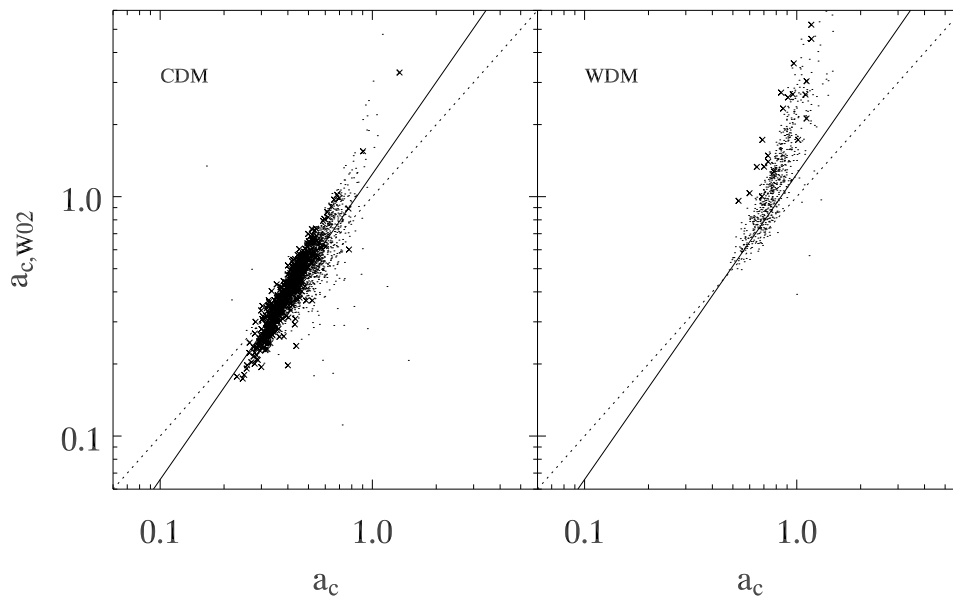


**Figure 7.10.** Comparison of the formation epochs defined by W02 (equation [7.8]) and our generalization (equation [7.9]). The left panel represent halos from the CDM run and the right panel shows WDM halos. Dots are halos from the large volume run and crosses are from the small volume run. The dotted line shows an exact correspondence and the solid black line is a polynomial fit to the CDM halos.

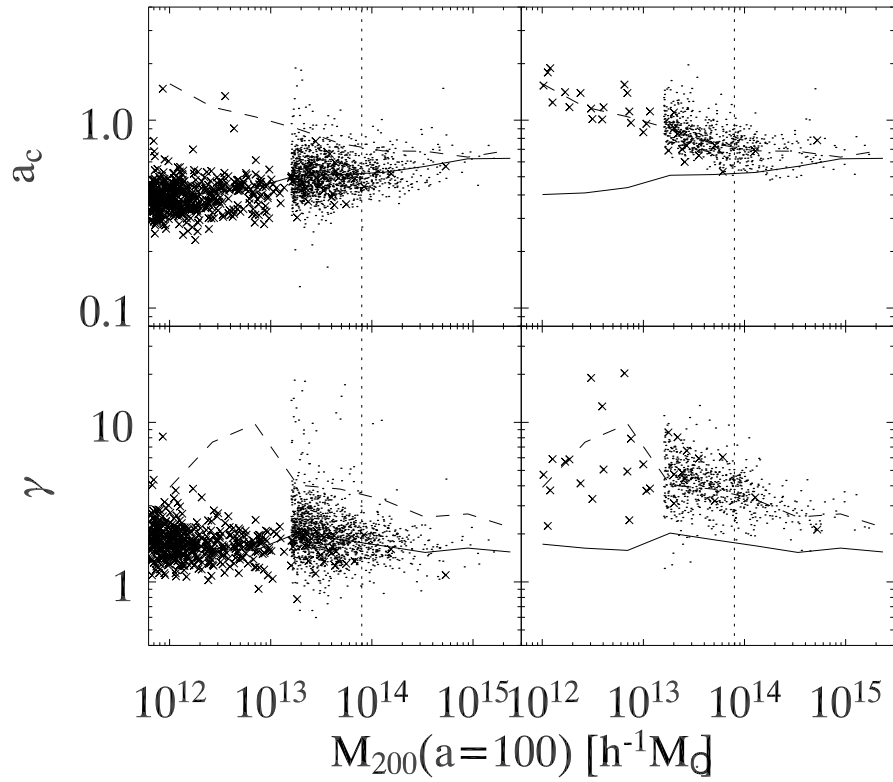
and  $a_{c,W02}$ .

Figure 7.11 plots the variation of  $a_c$  (top panels) and  $\gamma$  (bottom panels) with mass for CDM (left panels) and WDM (right panels) halos. Again, dots represent halos from the large volume realizations, and crosses are halos from the smaller volumes. Common to both the left and right panels are average trend lines for the CDM (solid curves) and WDM (dashed curves) halos. The plot shows all halos from our simulations that are well resolved at the end of the simulation ( $M_{200} > 400$  particles for the large volume realizations and  $M_{200} > 1000$  particles for the smaller volume realizations — see Appendix C for a further discussion). At the high mass end,  $M_{200} > 2M_c = 2 \times 10^{14} h^{-1} M_\odot$ , the average  $a_c$ 's differ by only  $\sim 10\%$ , less than the scatter for either cosmology. The rate index,  $\gamma$ , however, is about 50% higher in the WDM cosmologies at these high masses, reflecting the steeper MAHs presented in right side of Figure 7.9.

As mass decreases, both  $a_c$  and  $\gamma$  behave differently in the two cosmologies. The formation epoch decreases with mass in the CDM runs (in accordance with “bottom up” structure formation) but actually increases with mass in the WDM cosmologies. The number of WDM halos that exist with  $M_{200} \ll M_c$  — all with later formation times than halos with mass greater than  $M_c$  — again suggests that most small halos form through an instability of regions inside larger structures. This claim is consistent with our picture of sub-truncation scale halos forming through incomplete collapse of larger perturbations. For CDM halos, we again see the presence of the hierarchical structure formation from the fact that  $\gamma$  is relatively constant throughout the entire mass range,  $\gamma \approx 2$  with modest scatter. In contrast, the WDM cosmology has  $\gamma$  increasing with lower masses, roughly as  $\gamma \propto M_{200}^{-0.2}$ . The spray of particles with  $a_c$  and  $\gamma$  much larger than the averages in the CDM cosmologies is a result of the difficulty in measuring these parameters for poorly resolved halos. The MAH cannot be measured accurately for halos that do not grow substantially above our resolution limit, and consequently our fit parameters have large uncertainties. The mean relation is actually within these uncertainties for all the low mass halos.

We also compare our modified MAH fitting formula with the model of W02 in the range of halo formation up to the present epoch in Figure 7.12. In this figure, we compare the residuals of fits of the average MAH to equation (7.9), fit from  $a = 0.3 - 100$  (dark line) and  $a = 0.3 - 1$  (medium line) with equation (7.8) fit from  $a = 0.3 - 1$  (light line) for different mass ranges taken from our CDM simulations. The RMS values for the residuals in  $\ln M$  are shown in Table 7.3. While the rms residual between our modified fitting formula from  $a = 0.3 - 100$  is approximately a factor of 2 lower than the W02 model for all mass ranges, equation (7.9) fit from  $a = 0.3 - 1$  offers a substantial improvement over equation (7.8), decreasing the rms residual by a factor of 5 or more at the plotted masses. The introduction of  $\gamma$  is apparently an important correction for the early time MAH growth as well as





**Figure 7.11.** *Top Panels:* The dependence of halo's formation epoch ( $a_c$  in equation [7.9]) on mass. The left panel shows halos from the CDM run, and the right halos from the WDM cosmology. Dots represent halos from the large box run, and crosses are from the small box run. The solid and dashed curves show the trend of  $a_c$  mass for the CDM and WDM cosmologies, and the vertical dotted line is  $M_c$ . *Bottom Panel:* Same as the top panel, but now plotting the behavior of  $\gamma$ , the amplification factor of equation (7.9), as a function of mass.

**Table 7.3.** RMS residuals of MAH fits:

$M_{200}[h^{-1}M_{\odot}]$	Equation (7.9): $a = 0.3 - 100$	Equation (7.9): $a = 0.3 - 1$	Equation (7.8): $a = 0.3 - 1$
$(0.6 - 1.2) \times 10^{14}$	0.14	0.044	0.21
$(3 - 6) \times 10^{13}$	0.14	0.036	0.31
$(1.5 - 3) \times 10^{13}$	0.15	0.088	0.43

**Table 7.4.** MAH Parameters:

$M_{200}[h^{-1}M_{\odot}]$	$a_{c,W02}$ 0.3 - 100	$a_c$ 0.3 - 1	$a_c$ 0.3 - 1	$\gamma$ 0.3 - 100	$\gamma$ 0.3 - 1
$(0.6 - 1.2) \times 10^{14}$	0.54	0.47	0.52	2.0	1.5
$(3 - 6) \times 10^{13}$	0.53	0.50	0.52	2.1	1.6
$(1.5 - 3) \times 10^{13}$	0.48	0.48	0.50	2.3	1.8

the late time asymptote. Table 7.4 lists the values for  $a_c$  and  $\gamma$  for the profiles of Figure 7.12. The fits are robust in the sense that  $a_c$  does not change substantially depending on how the MAH is calculated. In all cases, however, the best fit returns  $\gamma$  substantially larger than 1, and may have some mass dependence. The exact value of  $\gamma$  depends strongly on the fit range, with fits out to  $a = 100$  requiring a larger value in order for the MAH to asymptote properly. These larger values of  $\gamma$  in turn push  $a_c$  slightly earlier. Fitting in the range  $0.3 \leq a \leq 1$ , results in  $\gamma \approx 1.6$  with values for  $a_c$  that differ from those of the W02 model by only 4%. While our average halo MAHs all appear to have  $\gamma > 1$ , there is a much larger spread when considering fits for individual halos. Here,  $\gamma$  ranges from 0.2 – 10 and the fits have residuals that are typically 20% lower than those of equation (7.8).

### 7.3.2 Halo Substructure

In this section, we compare the subhalo distribution of our CDM and WDM cosmologies, considering only halos from our smaller volume simulations. While these

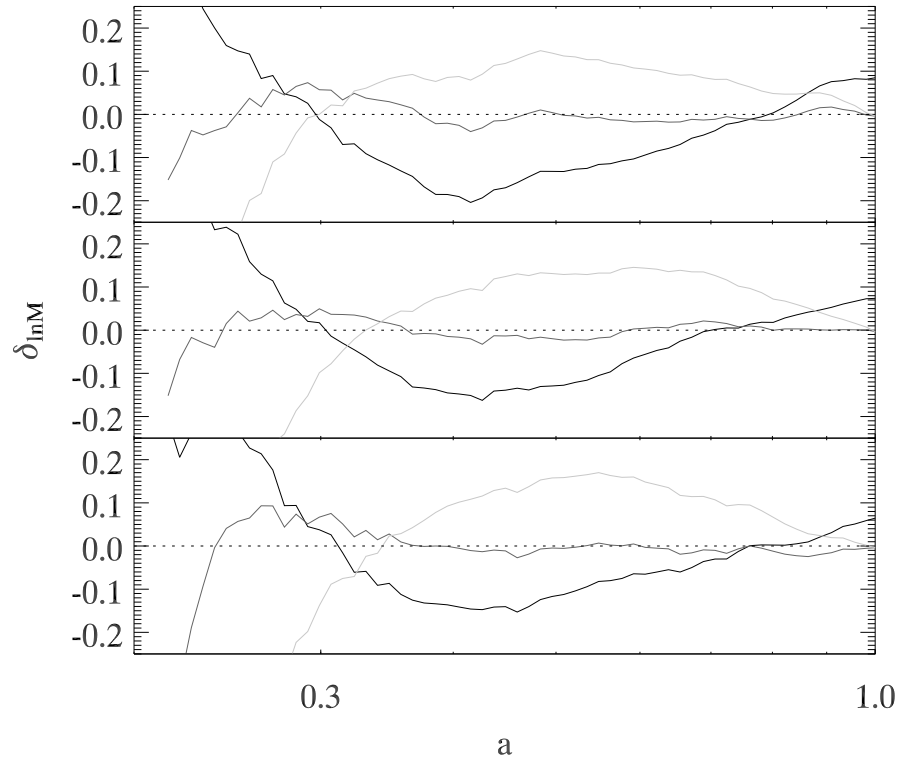


**Figure 7.12.** Residuals of average MAHs to various fits. The dark lines are the residuals to equation (7.9) fit in the range  $a = 0.3 - 100$ . The medium lines also use equation (7.9), but the fit is calculated over  $a = 0.3 - 1$ . The light lines fit the model of Wechsler et al. (2002), equation (7.8), to the range  $a = 0.3 - 1$ . The halos are in the mass ranges (top to bottom)  $M_{200} = (0.6 - 1.2) \times 10^{14}, (3 - 6) \times 10^{13}, (1.3 - 3) \times 10^{13} h^{-1} M_{\odot}$ .

simulations do not contain a statistically large number of halos, the larger volume simulations do not have the necessary resolution to accurately describe the subhalo population.

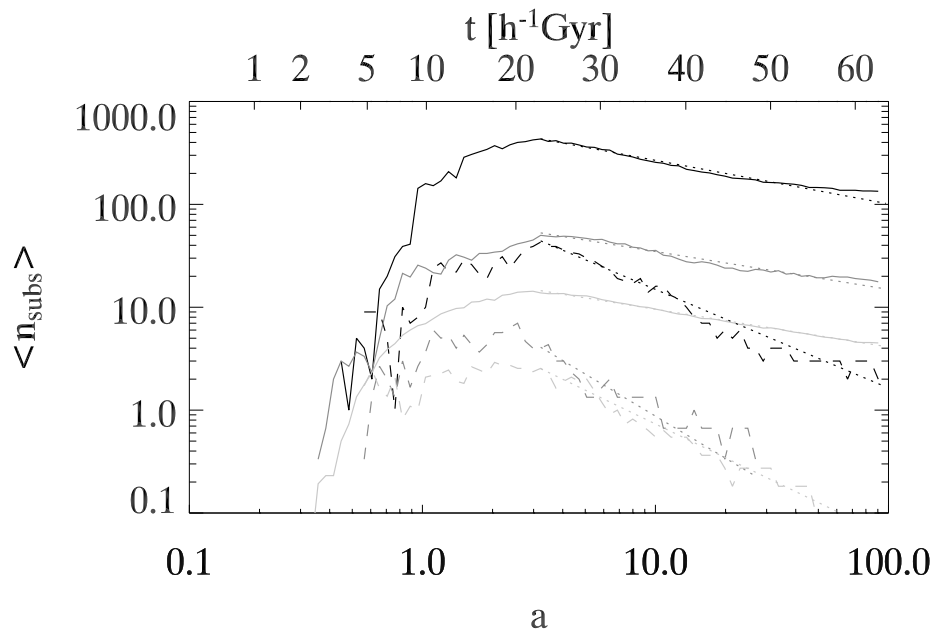
Not surprisingly, the most dramatic difference between the subhalo populations of our CDM and WDM halos is their abundance. In the CDM simulation, the average number of subhalos with  $M > 1.24 \times 10^{10} h^{-1} M_{\odot}$  (20 particles) is roughly proportional to the mass of the host halo,  $\bar{n}_{subs} \propto M_{200}$  at  $a = 1$ . For host halos of all masses, approximately 10% of the host mass is in bound substructures at this epoch, a value consistent with previous studies (Klypin et al., 1999). In contrast, for the WDM cosmology  $\bar{n}_{subs} \propto M_{200}^{0.4}$ , with only about 5% of the host mass in bound subhalos. By  $a = 100$  in the CDM cosmology, the slope of the number of subhalos with mass has not changed substantially,  $\bar{n}_{subs} \propto M_{200}^{1.2}$ , but many subhalos have been destroyed, and only 0.3% of the mass of an average halo is contained in substructure. The steepening of the slope is caused by a more efficient destruction of subhalos in hosts with lower masses. Small halos today contain smaller, more weakly bound, subhalos than larger hosts. Additionally, these small halos undergo fewer future mergers to replenish their subhalo population. By contrast, with the exception of the single largest WDM halo, none of the WDM halos contain any substructures at  $a = 100$ . Even this largest halo has only  $\bar{n}_{subs} = 2$ , as opposed to  $\bar{n}_{subs} = 137$  in its CDM counterpart. Surprisingly, the shape of the subhalo mass function,  $dn_{sub}(M_{sub})/d\ln(M_{sub}/M_{Host})$ , does not change substantially between today and  $a = 100$ . The mass function is truncated at the high mass end ( $M_{sub}/M_{Host} > 0.01$ ) and is slightly steepened. This is due to the increased effect of dynamical friction on more massive objects, pulling them towards the center of the halo where they are more easily disrupted and stripped of mass.

Figure 7.13 shows the evolution of the average number of subhalos in halos of various masses. CDM and WDM halos of all sizes show similar evolution in the average

number of subhalos. For  $a \leq 3$ , mergers create substructure, resulting in an increasing  $\bar{n}_{subs}(a)$ . After mergers end,  $a \approx 3$ , no new subhalos are accreted and existing subhalos gradually fall inward and are disrupted due to dynamical friction and tidal forces. The number of subhalos in the WDM cosmology, however, drops much more rapidly than in the CDM cosmology. The primary reason for this difference is the lower binding energy of the subhalos caused by the later formation epoch of low-mass WDM halos. When these halos accrete onto more massive halos, they are much more prone to disruption and consequently have a shorter life, as discussed in Cloin et al. (2000). While WDM subhalos are formed with a lower binding energy/density, most other properties, including their average velocity, velocity dispersion, and mass, differ very little between the CDM and WDM models. The only other systematic difference is the average distance a subhalo lives from the center of its host — WDM subhalos tend to live further out. This is also related to the lower binding energy of WDM subhalos, since they are more easily disrupted when they move closer to center of their host. As a measure of subhalo destruction, we have fit the evolution of  $\bar{n}_{sub}$  during the late-time deSitter expansion (when the host halos are no longer being disrupted by mergers) to an exponential decay,

$$\bar{n}_{sub}(a) = \bar{n}_m e^{-\alpha'(t-t_m)} = \bar{n}_m (a/a_m)^{-\alpha}, \quad (7.10)$$

where the subscript  $m$  denotes the epoch where the subhalo population is at its maximum, and  $\alpha'$  is the subhalo decay rate, with  $\alpha' = H\alpha = \alpha 0.0856 \text{Gyr}^{-1} h$  for our  $\Lambda$ -dominated cosmology ( $H = H_\infty$ ). For our CDM halos, we get  $\alpha = 0.38 \pm 0.03$ , while for the WDM halos there is a much more rapid decay,  $\alpha = 1.1 \pm 0.2$ , yielding subhalo half-lives of  $21 \pm 2$  and  $7.4 \pm 1 h^{-1} \text{Gyr}$ , respectively. Figure 7.13 makes it appear that equation (7.10) fits better for lower mass halos. This, however, is an artifact of the fact that we have only a few high mass halos in each simulation, giving us poor statistics.



**Figure 7.13.** The evolution of the average number of subhalos in host halos of various masses. The solid curves indicate CDM halos, and the dashed WDM halos. At  $a = 100$ , the halos have masses  $M_{200} = (2 - 4) \times 10^{13}$  (light line),  $(0.5 - 1.3) \times 10^{14}$  (medium line), and  $> 4 \times 10^{14} h^{-1} M_{\odot}$  (dark line). The dotted lines show fits to equation (7.10).

### 7.3.3 Density Profile

The radial density profile is one of the most fundamental halo properties. Previous WDM studies (Moore et al., 1999b; Colín et al., 2000; Bode et al., 2001) indicate that WDM halo density profiles do not differ substantially from their CDM counterparts, and our simulations support this finding. Figure 7.14 shows average density profiles for all particles bound to halos from the CDM and WDM cosmologies at  $a = 100$  from our smaller volume runs. The solid lines are CDM halos from the mass ranges of Figure 7.9, and the dashed lines are WDM halos. The different mass ranges have been offset and the density multiplied by  $r^2$  to make the differences between the various profiles more visible. The halos can be described by an NFW profile, equation(7.5) for the range  $0.05r_{200} \lesssim r \lesssim r_{200}$ . Here,  $r_s$  and  $\rho_s$  are the the NFW scale radius and density. The middle panel of Figure 7.14 shows the residuals to the NFW fits for the nine plotted profiles, which generally fall in the  $\sim 5\%$  range.

Previous work (Busha et al., 2005) has shown that well before  $a = 100$ , halos in a  $\Lambda$ -dominated universe develop clear edges at  $r \approx 4.6r_{200}$ . Beyond  $r_{200}$ , the NFW profile is much too shallow and the density profile for all bound material is better fit by a truncated Hernquist profile,

$$\rho = \frac{\rho_0}{(r/r_c)(1 + r/r_c)^3} e^{(-r/r_{halo})^{5.6}}, \quad (7.11)$$

where  $\rho_0$  and  $r_c$  are the central density and core radius, and  $r_{halo}$  is the radial extent of all bound halo material. Residuals to this fit are shown in the bottom panel of Figure 7.14. This fit has larger residuals than NFW for  $r < r_{200}$ , but has much smaller residuals at larger radii and provides a good description of the halo out to its actual edge.

As with the MAHs, there is little difference between the density profiles of the WDM and CDM cosmologies for halos with  $M_{200} \gg M_c$ . Specifically, for the plotted profiles in this range, most differences are at the  $\sim 1\%$  level. Significant differences

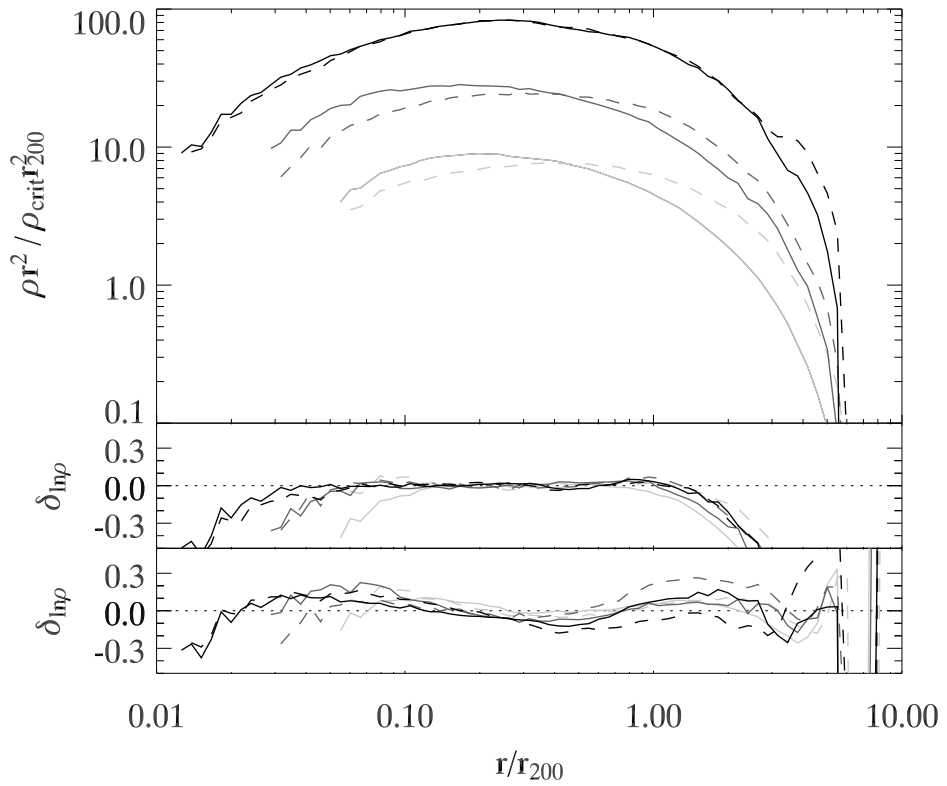


**Figure 7.14.** *Top Panel:* Average density profiles times  $r^2$  for all bound material in halos at  $a = 100$  from our smaller volume runs. Halos selected according to the mass ranges  $M_{200} = (2 - 4) \times 10^{13}$  (light line),  $(0.6 - 1.3) \times 10^{14}$  (medium line), and  $> 4 \times 10^{14} h^{-1} M_{\odot}$  (dark line), with the solid and dashed lines representing CDM and WDM halos. The profiles have been offset from each other to make them easier to see. *Middle Panel:* Residuals of NFW fits to the above six profiles. *Bottom Panel:* Residuals of truncated Hernquist fits (equation [7.11]) to the above six profiles.



appear as we near the truncation scale,  $M_c$ , but, remarkably, the profiles are still well fit by both the NFW and Hernquist profiles, as indicated by the residuals in the bottom panels of Figure 7.14. We define the concentration in the usual way,  $c_{200} = r_{200}/r_s$ . As noted above, the parameter  $r_s$  is measured by fitting an NFW profile to our profiles using logarithmically spaced radial bins in the range  $0.05r_{200} - r_{200}$  (similar to Bullock et al., 2001). For equilibrated halos at  $a = 100$ , the steepness of the halo density profile causes  $r_s$  to change substantially if we fit to a different radius. By increasing the outer fit radius to  $r_{vir} \approx 2.5r_{200}$  as in Bullock et al. (2001), concentrations typically decrease by a factor of 2 or greater, depending on the mass of the halo. A more robust concentration could alternatively be measured as  $c_{halo} = r_{halo}/r_c$  from equation (7.11), although the definition using the NFW fit is more standard (and our new definition is not well defined for  $a \lesssim 3$ ). The relation between  $r_c$  and  $r_s$  is well fit by a power law,  $r_c \propto r_s^\nu$ , with  $\nu = 0.974 \pm 0.004, 0.88 \pm 0.02$  and proportionality constants 0.40 and 0.24 for the CDM and WDM cosmologies. For what follows, however, we will continue to use the concentration defined with an NFW fit.

Figure 7.15 shows the dependence of the concentration on mass for our halos at  $a = 100$ . As with Figure 7.11, the left panel shows CDM halos and the right panel WDM halos, with dots representing halos from the large volume realizations and crosses halos from the small volume realizations. While not shown, the  $a = 100$  concentrations are very similar to the  $a = 1$  values. This should not be surprising in light of the fact that halo growth is nearly complete at  $a = 1$ . As seen in Figures 7.8 and 7.9,  $M_{200}$  for CDM halos only grow by  $\sim 30\%$  between  $a = 1$  and 100, saturating around  $a \sim 2 - 3$ . Similarly, concentrations for halos of a given mass increase by a modest 10% during this time and reach their final value around  $a \sim 2$ . Figure 7.15 follows many of the overall trends of Figure 7.11. Again, for  $M_{200} \gg M_c$  the average values for  $c_{200}$  differ by less than 10% for CDM and WDM halos and systematically

diverge for lower masses. The low mass WDM halos are much “puffier” than similar mass halos (or their counterparts) in the CDM simulations. W02 explained the trend of changing  $c_{200}$  with  $M_{200}$  by identifying a relationship between  $c_{200}$  and  $a_c$ , which we have reproduced with our data in Figure 7.16. Both the CDM (left panel) and WDM (right panel) halos follow a power law relation  $c_{200} \propto a_c^{-\beta}$ , although there is a substantial amount of scatter present in the CDM relation. For CDM halos,  $\beta = 0.79 \pm 0.2$  (solid line), while the WDM halos have  $\beta = 0.86 \pm 0.3$  (dashed line), values that are both within  $2\sigma$  from the combined slope  $\beta = 0.79 \pm 0.1$  (dotted line). This finding is similar to the  $c \propto a_c^{-1}$  relation proposed by W02. Note that for W02,  $r_{200}$  is replaced with  $r_{vir} \approx 2.5r_{200}$  at  $a = 100$  (Eke et al., 1996). The explanation for this trend is that  $c_{200}$  is a reflection of the average density at the time of collapse, so that halos forming earlier should have higher concentrations, exactly as observed. This trend holds even for WDM halos with  $M_{200} \ll M_c$ . The right panel of Figure 7.15 shows that low mass WDM halos have lower concentrations, while the upper right panel of Figure 7.11 demonstrates that such low-mass halos collapse later. This picture is further enforced by a toy model for concentrations proposed by Eke et al. (2001), modified to use our density threshold. Noting that in WDM models  $c_{200}$  decreases with mass below the truncation scale, Eke et al. (2001) defined an effective perturbation spectrum,

$$\sigma_{eff}(M) = -\frac{d\sigma(M)}{d \ln(M)}, \quad (7.12)$$

so that the spectrum also decreases at low masses. From this equation, a collapse epoch,  $a_{c,toy}$  can be identified as the epoch where  $D(a_{c,toy})\sigma_{eff}(M_s) = 1/C_\sigma$ , where  $M_s = M(< 2.17r_s)$  (the mass contained within the radius where the circular velocity of a NFW profile reaches its maximum) and  $C_\sigma$  is a fitting parameter. A central density is defined as in Bullock et al. (2001) such that  $M_{200} = 4/3\pi r_s^3 \tilde{\rho}_s$ . We then assume that

$$\tilde{\rho}_s = 200\rho_{crit}(a)c_{200}^3 \quad (7.13)$$

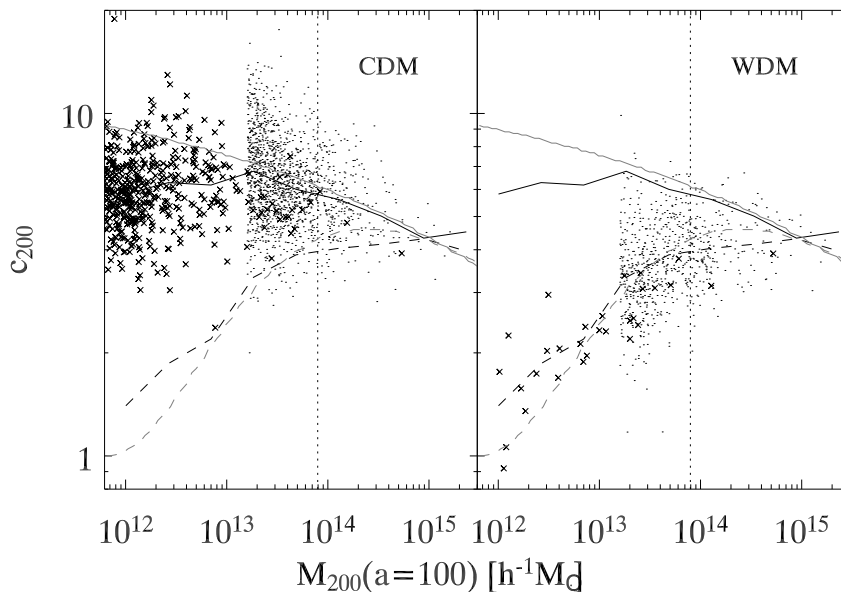


**Figure 7.15.** The concentration ( $c_{200} = r_{200}/r_s$ ) as a function of mass for CDM and WDM halos at  $a = 100$ . Dots represent halos from the large box run, and crosses are from the small box run. The dark solid and dashed lines show average  $c_{200}(M_{200})$  values for CDM and WDM halos, and the vertical dotted line marks the truncation scale,  $M_c$ . The light solid and dashed lines show the calculated  $c_{200}(M_{200})$  relation from the toy model discussed in §7.3.3.

and set this density scale equal to our overdensity at the epoch of formation,  $200\rho_{crit}(a_{c,toy})$ .

This procedure yields the relation

$$c_{200} = \left[ \frac{\rho_{crit}(a_{c,toy})}{\rho_{crit}(a)} \right]^{1/3}. \quad (7.14)$$

The only free parameter in this model is the constant  $C_\sigma$ , which we set equal to 32. The results of this model are plotted as the lighter curves in Figure 7.11. The model characterizes the simulated halos for both the CDM and WDM cosmologies at  $a = 100$ , and produces equally good agreement at earlier epochs. Our toy model differs from that of Eke et al. (2001) only in that we define our halos in terms of  $200\rho_{crit}$ , as opposed to the epoch-dependent quantity  $\Delta(a)\rho_{crit}$ . We find that using  $\Delta(a)\rho_{crit}$  requires different values for  $C_\sigma$  at  $a = 1$  and 100.

In all of our simulations, the density profile is well characterized by an NFW profile for much of the halo's radial extent, and that the quality of the fit does not depend on whether a halo was taken from a CDM or WDM cosmology. The primary difference

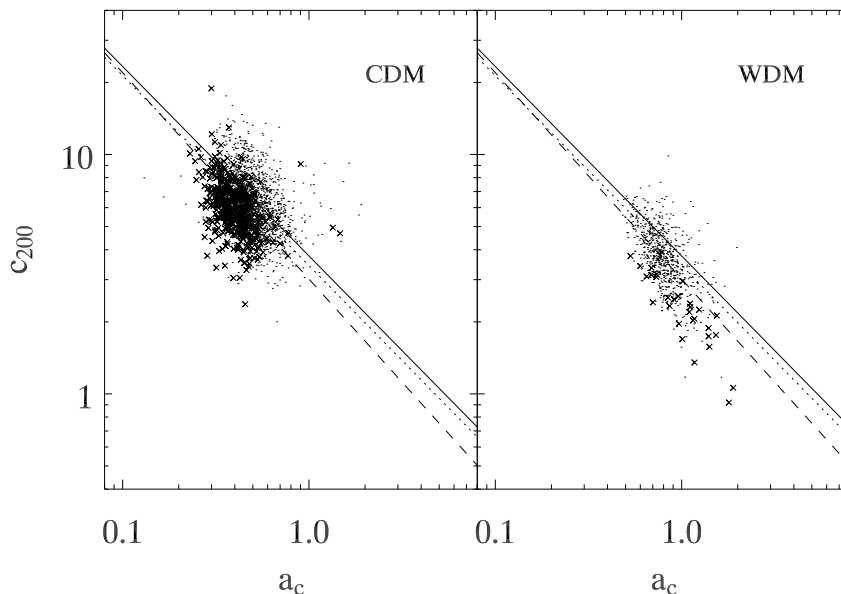


**Figure 7.16.** The  $a = 100$  concentrations as a function of formation epoch,  $a_c$  from equation (7.9) for CDM and WDM halos. Dots represent halos from the large box run, and crosses are from the small box run. The solid line is the trend-line for CDM halos, and the dashed line is the trend-line for WDM halos. The dotted line is the trend-line for the combined sample of all CDM and WDM halos.

between halos in these two models — the change in concentration parameter — follows a simple relationship with the formation epoch that is relatively insensitive to how the halos form: CDM halos that have accreted their mass as virialized clumps; WDM halos with  $M_{200} > M_c$  that have formed through a period of rapid smooth accretion followed by growth through accretion of clumps; and WDM halos with  $M_{200} < M_c$  that have formed through a single period of rapid smooth accretion.

## 7.4 Conclusions

This work examines the effects of small scale structure and merger activity on the formation and ultimate structure of halos in a  $\Lambda$ -dominated universe. Using N-body simulations with an initial power spectrum that is truncated on small scales, we model a WDM-like universe where the formation of early low-mass objects is suppressed and compare the results to standard  $\Lambda$ CDM simulations. Without these seeds for

hierarchical growth, halos above the truncation scale form through an initial rapid accretion phase, resulting in objects with mass  $M_{200} \sim M_c = 8 \times 10^{13} h^{-1} M_\odot$ . These objects can then grow through mergers with other large halos. Many halos also form below the truncation scale through incomplete collapse of larger perturbations. These halos form solely through a monolithic-like collapse process. Regardless of their size, WDM halos typically form later and faster, with a larger  $\dot{M}_{200}(a)$  than their counterparts in an  $\Lambda$ CDM cosmology.

To describe this rapid accretion, we generalize the Wechsler et al. (2002) mass accretion history formula by introducing a rate index,  $\gamma$ , that controls the growth rate evolution,  $d \ln(M)/d \ln(a) \propto a^{-\gamma}$ . This parameter is necessary in order to fit the halo MAH into the far future. Otherwise, the halo mass approaches its asymptote much too slowly. Additionally, for ensemble-averaged halo histories fit to the present epoch ( $a \leq 1$ ), we recover  $\gamma \sim 1.6$ , substantially higher than the  $\gamma = 1$  assumed in Wechsler et al. (2002). The larger  $\gamma$  reduces the RMS errors of the fit to the mean MAHs by a factor of 5. Our generalization also reduces the number of objects that have unphysical formation epochs,  $a_c \gg 1$ .

We have also calculated abundances and decay rates for substructure in our dark matter halos. As expected, WDM halos contain much less substructure, and most host halos destroy all of their subhalos by the end of our simulations at  $a = 100$ . The decay of subhalos is (on average) exponential in time with half-lives 21Gyr and 7.4Gyr for the CDM and WDM cosmologies. This is consistent with the picture discussed below where later formation times create lower concentration objects that are more prone to disruption.

Despite differences in the formation process and substructure abundance, WDM halos exhibit NFW density profiles, just like CDM halos, albeit with a different  $c_{200}(M_{200})$  relationship. Halos in WDM cosmologies have lower concentrations than their CDM counterparts, but follow the same  $c_{200}(a_c)$  relation, allowing us to relate

concentration to mass in both cosmologies using a 1 parameter toy model that characterizes the concentration using the linear power spectrum. This characterization is motivated by the idea that the concentration is set by the cosmological background density at the epoch of collapse. The form of the halo density profile persists, even though the method of formation and amount of substructure is changed substantially in our WDM cosmology. Taken together, our results suggest that the form of the halo density profile is set not by merger activity, but instead through large-scale modes of the gravitational relaxation process. Halos appear to be very efficient at erasing their initial conditions and do not care whether their mass was accreted rapidly, slowly, in clumps, or continuously. The only aspect of the density profile directly linked to the halo formation process appears to be the concentration, which is set by the formation epoch, the epoch when the mass accretion rate drops to a specific value. In particular, substructures and major mergers seem to have little effect in driving the equilibrium structure of a halo.

## CHAPTER 8

# Conclusions

We live at a special epoch when the contributions of dark matter and dark energy to the total energy budget of the universe are comparable. While the universe is in this state, we can observe galaxies forming and growing through hierarchical processes, but we can also detect the presence of the dark energy component that will soon (on a cosmological timescale) end such growth. Because the universe exists in this state only briefly, this is often called the coincidence problem. We live during the rare epoch when we have the ability to understand both the past and future of our universe.

Most studies attempting to understand the origin of the halo density profile examine halos at the present epoch. However, as we have shown, the  $a = 1$  halos are in a state of frustrated equilibrium, making it difficult to separate the relaxed material from that which is unbound and unrelaxed. Because the halo is being substantially affected by continuous mass accretion, it is impossible to study the structure of the entire halo, whose boundary is poorly defined. This thesis provides an important contribution by showing that, interior to  $r_{200}$ , halo structure changes little between today and the epoch where the entire halo has relaxed. In this chapter, we summarize the major points of this dissertation and address some unresolved issues.

Using a suite of N-body simulations, we use the quiet, lonely future of the universe to understand the equilibrium structure and distribution of dark matter halos. While the far future of large scale structure is an aspect of structure formation to which

little attention has been paid (aside from the work presented in this dissertation see the papers of Nagamine & Loeb, 2003; Dünner et al., 2007; Hoffman et al., 2007; and Krauss & Scherrer, 2007), such studies can yield a wealth of insight about dark matter halos. In particular, this work emphasizes that structure formation is nearly over (yet not quite complete) and that dark matter halos of the present epoch have yet to fully relax. While these may seem like obvious points within the context of the hierarchical growth model, they are nonetheless important to emphasize.

In order to understand halo equilibrium, chapter 4 addresses the halo sphere-of-influence. This emphasizes that structure formation is incomplete at the present epoch and that halos will grow substantially before reaching an ultimate mass. Using energy considerations, we derived a critical overdensity of  $\delta_0 = 17.6$  that determines the boundary between material that will ultimately collapse into the halo and that which is destined to remain unbound in a  $\Lambda$ CDM cosmology. Numerical simulations validate this estimate at roughly the 10% level. While halos are still growing today, the accelerated expansion of the universe will eventually cause halo growth to cease.

We also show that the cosmic web — the large scale distribution of halos — remains relatively unchanged between today and the far future. Because of the dark energy-dominated era, the accelerated expansion quickly causes the growth function,  $D(a)$ , to saturate, which prevents the future collapse of any perturbations that have yet to go non-linear. Halos that have already formed will experience a limited amount of growth by accreting material within their spheres of influence. This has only a second order impact on the large scale matter distribution because substantial halo growth is halted as the accelerated expansion overcomes gravitational attraction to push halos further and further away from each other in the physical frame. The comoving cosmic web becomes frozen in place as halos shrink to become smaller and smaller objects in this frame.

We also examine the asymptotic halo density profile. We show that there is little



evolution in the inner density profile ( $r < r_{200}$ ) out to  $a = 100$ , which remains similar to the NFW profile. At larger radii, however, the profile becomes much steeper. Using a fit for the time-evolving density profile, equation (4.16), we are able to estimate the asymptotic form of the halo density profile as  $a \rightarrow \infty$  (assuming that halos do not evaporate due to the true 2-body relaxation of the dark matter particles, which happens on a vastly longer time scale than those considered here). Given this asymptotic universal density profile, chapter 5 calculated the associated asymptotic form of the halo metric. The idea that such a metric exists is a profound one. In the far future, spacetime will consist of a flat background space-time that is occasionally punctuated by isolated halos with nearly identical local metrics. This emphasizes how we will return to a pre-1900 view of cosmology as the population of the universe becomes a spray of isolated galaxies that are effectively island universes. As halos establish their equilibrium, they become isolated from each other and are allowed to relax without disruption from nearby material.

We examine the approach of halos to equilibrium in chapter 6. In particular, we show that today's halos exist in a state of frustrated equilibrium where accretion events continuously disrupt halo relaxation. The halo radial velocity profile of today is characterized by two zero-velocity surfaces: an inner surface internal to which material is in hydrostatic equilibrium, and an outer surface external to which the Hubble flow dominates over the gravitational attraction of the halo. Much of the material that will ultimately be a part of the halo exists in a confusion region between these two surfaces that contains both virialized material in stable orbits around the halo and non-virialized material that has only recently been accreted and may not remain bound. The various methods for sorting out the material living in this region are responsible for the plethora of halo mass definitions. As  $\Lambda$  becomes more dominant, accretion is turned off and the halo begins to relax. The inner hydrostatic surface marches out toward and merges with the turnaround surface. As a consequence of

this merging, the halo develops a well-defined edge and mass that is roughly twice that of the final  $M_{200}$ . Throughout this relaxation, the total amount of virialized material in the halo roughly doubles.

While chapters 4-6 concentrated on the establishment of an equilibrium configuration, little effort was made to understand the physical processes important for setting this configuration. Chapter 7 considers the affect of mass accretion on the equilibrium structure by running a suite of simulations with and without small-scale power, effectively comparing  $\Lambda$ CDM and  $\Lambda$ WDM cosmologies. The absence of small-scale power substantially alters the accretion history of dark matter halos. The formation of small WDM halos is strongly suppressed relative to the CDM cosmology. While low-mass halos are virtually non-existent, the distribution of high-mass halos in the WDM cosmologies is relatively unchanged when compared to the CDM cosmologies. These high-mass WDM halos accrete the bulk of their mass through a single, smooth, and rapid accretion event that is minimally disrupted by merger activity, in stark contrast with the hierarchical growth of CDM halos. The suppression of low-mass halos also results in a strong suppression of the subhalo population in the large WDM halos.

In spite of these differences, the global properties of halo structure are essentially unchanged between the two cosmologies. Halos of both cosmologies have density profiles that are equally well characterized by the NFW profile for sufficiently small radii. The one persistent difference between the two cosmologies, the lower concentrations of halos at a fixed mass in the WDM cosmology, is explained by later formation epochs of the WDM halos. In particular, the form of the density profile is not set by the method of mass accretion but must instead come from violent relaxation that erases memory of the initial conditions regarding how mass is accreted.

Using the far future of the universe as a laboratory, this thesis has presented a picture of the equilibrium structure of dark matter and an analysis of some of the processes relevant in setting this structure. However, a number of unresolved

issues remain. The most obvious (and challenging) issue is the lack of an analytic framework that would allow us to use the cosmological initial conditions (i.e., the power spectrum  $P(k)$ ) to predict both the halo distribution and internal structure, in particular the NFW profile. This profile results from a collective relaxation process that is nearly independent of the power spectrum, but identifying and understanding the exact process remains elusive. There are a number of ways to approach this issue. One method would be to study the evolution of the halo phase space structure, using  $\rho/\sigma^3$  as a proxy, where  $\rho$  is the local density and  $\sigma$  the local velocity dispersion. As mentioned in section 2.4.2, a number of studies have shown that the radial halo phase space profile is a featureless power-law, whose origin may be easier to understand than the broken power-law density profile. Preliminary examinations of  $a = 100$  halos show the persistence of a power-law profile that does not appear to be appreciably different from the  $a = 1$  profile for both CDM and WDM cosmologies. Additionally, the interior phase space distribution for CDM and WDM halos that formed at the same epoch appears unchanged, in spite of the fact that in the initial conditions the WDM halos began with substantially higher phase space densities. Understanding how the phase-space distribution relaxes may give us some clues to the origin of the density profile.

An alternative approach to this question would be to remove halos from their cosmological setting and study them as isolated objects in idealized environments. While a number of such studies have been carried out, the conclusion of this thesis that cosmology is not an important factor in setting the equilibrium configuration lends additional justification for such an approach. By studying halos in idealized environments with simplified physics that limit the allowed relaxation mechanisms (such as a forced spherical symmetry for the force calculation that would further eliminate the effects of substructure) it may be possible to understand which relaxation processes are needed to create an NFW profile.

Another unresolved issue involves the validity of the halo model. While the halo model begins with the assumption that all dark matter lives in a collapsed halo of some mass, chapter 6 shows that a substantial amount of material is expelled from a halo as it relaxes. The fate of such expelled material should be addressed. Is this material able to condense into a series of small halos, or is it too hot and destined to exist as a low-density stream of diffuse material filling the otherwise empty space between halos? In particular, we must characterize how much material is destined to end up outside of all halos larger than some mass threshold.

Finally, throughout this thesis, it was assumed that the dark energy took the form of a cosmological constant,  $\Lambda$ . While this is certainly the simplest model and one that is well within current observational constraints, we have not addressed how these results would change if the dark energy had a different (possibly time-evolving) equation of state. I would be surprised to find any fundamental changes to the equilibrium halo structure if  $w$  was varied such that  $-1/3 > w \geq -1$ , but many of the exact values (i.e., the asymptotic ratio of  $M_{halo}/M_{200}$ ) should vary with  $w$ . This picture would be very different, however, for a cosmology with “phantom energy”, where the dark energy has an equation of state with  $w < -1$  (Caldwell et al., 2003). The energy density of such a substance would actually increase as the universe expands and eventually result in an expansion that would unbind halos, globular clusters, and even planets through a process known as the big rip. Unfortunately, because the very nature of studying the far future of the universe means that many of the results will be unobservable, we are unable to use such a test to constrain the nature of the dark energy.

All of these questions regarding the origin of dark matter halo structure are of fundamental importance to the field of cosmology. Being the dominant component of the universe, dark matter halos provide the environment where galaxies form and evolve, and a strong understanding of these structures should aid us in describing

galaxies both as astrophysical objects and as cosmological probes. This thesis has used simulations of the far future of our universe to study the equilibrium structure of such halos, studies that inform us about both their future and past states. Because a dynamical equilibrium is reached, studies of the future of our universe can be used to understand the dark matter halo structure of today. Additionally, we are able to address the theoretical question of our long-term fate.

If our universe is dominated by a cosmological constant (or some form of non-decaying vacuum energy such that  $-1 \leq w < -1/3$ ), the far future will look remarkably different from the present. While extragalactic astronomy is currently an active field of study in a data-rich era, the exponential expansion driven by the dark energy will be the death of extragalactic astronomy and cosmology. Galaxies will merge with all objects in the immediate vicinity and be pushed away from more distant objects until the separation is greater than the Hubble radius. Observations will tell us that we live in a massive galaxy embedded in a dark matter halo, possibly with some substructure. External to this halo we will observe a static (non-expanding), empty universe with no Hubble expansion, similar to the model originally envisioned by Einstein when he first postulated his theory of General Relativity. Even the cosmic microwave background, another of the three pillars of the Big Bang, will eventually be cooled to an unobservable temperature. It is very likely that, based only on observations at such an epoch, we will be unable to postulate a complete theory of cosmology. Without the aid of studies of the current epoch, the field will effectively revert to its pre-1900 state.

## APPENDICES

## APPENDIX A

### Quintessence

In this Appendix we generalize our results to the case of a vacuum energy that depends on time, or equivalently, the scale factor  $a$ . For the sake of definiteness, we adopt the standard form for the vacuum energy equation of state, i.e., the vacuum pressure is given by

$$p_{\text{vac}} = w\rho_{\text{vac}}, \quad (\text{A.1})$$

where the parameter  $w$  is constant and lies in the range  $-1 \leq w < 0$ . Current observations seem to indicate a somewhat smaller range  $-1 < w \lesssim -0.5$  (e.g., Wang et al., 2000; Balbi et al., 2001). In fact, Spergel et al. (2003) place a 95% confidence limit of  $w \leq -0.5$  using a combination of the WMAP CMB data and the HST key project (Freedman et al., 2001) value for the Hubble constant and find that  $w \leq -0.78$  when additional constraints are added (from the SNIa-derived redshift distance relation, the 2dFGRS large-scale structure, and Lyman- $\alpha$  data, assuming a flat universe with constant  $w$ ). For completeness, we consider here the full range of constant  $w$  values from 0 to  $-1$ . With this equation of state, the scale factor evolves according to

$$\left(\frac{\dot{a}}{a}\right)^2 = H_0^2 \left\{ \Omega_{\text{m},0} a^{-3} + \Omega_{\text{v},0} a^{-p} \right\} \quad (\text{A.2})$$

where the index  $p = 3(1 + w)$ .

The energy equation (4.6) that determines whether or not overdense regions collapse, and the fate of test bodies, can be written in the form

$$\left(\frac{d\xi}{d\tau}\right)^2 = \Omega_{\text{v},0} a^{-p} \xi^2 - \beta + (\Omega_{\text{m},0} + \beta)/\xi, \quad (\text{A.3})$$

where  $\beta$  measures the gravitational influence of an existing structure according to equation (4.7). The case of overdense regions can be considered by replacing  $\beta$  with  $\Omega_{m,0}\delta_0$ , where  $\delta_0$  is the overdensity.

In order to determine whether trajectories turn around (and hence remain bound or collapse), the right hand side of equation (A.3) must vanish as before. In this case, however, the resulting cubic equation has time dependent coefficients and so the evolution of the scale factor must be considered simultaneously. As a result, we combine the two equations by changing the independent variable to  $a$  and thereby obtain

$$\left(\frac{d\xi}{da}\right)^2 = \frac{\Omega_{v,0}a^{-p}\xi^2 - \beta + (\Omega_{m,0} + \beta)/\xi}{a^2[\Omega_{m,0}a^{-3} + \Omega_{v,0}a^{-p}]}. \quad (\text{A.4})$$

Trajectories turn around when the right hand side of this equation vanishes. The minimum value of  $\beta$  required for such turnaround occurs when the right hand side of the equation has a double zero (both the right hand side and its derivative with respect to  $\xi$  vanish). To find the critical value of  $\beta$ , denoted here as  $\beta^*$ , we numerically integrate equation (A.4) and iterate to find the value that provides a double zero. This procedure must be carried out for every value of  $w$  (or  $p$ ). The resulting values of  $\beta$  are given below. The overdensities required for the collapse of future structures, for a cosmology with a given value of  $w$ , are given by  $\delta_0 = \beta^*/\Omega_{m,0}$ . This quantity is shown in Figure A.1.

We also provide a simple fit to the numerical result:

$$\beta^*(w) = \beta_0^* \left[ 1 + a(1+w) + b(1+w)^2 + c(1+w)^3 \right], \quad (\text{A.5})$$

where  $\beta_0^*$  is the value for a cosmological constant ( $\beta_0^* \approx 5.3$ ; §3.2) and where the coefficients are given by

$$a = -2.33, \quad b = 2.58, \quad c = -1.20. \quad (\text{A.6})$$

This simple cubic fit reproduces the numerical results with an absolute error bounded by  $0.035\beta_0^* \approx 0.19$  (a relative error of a few percent – see Figure A.1). A better fit



could be obtained by using polynomials of higher order, but this level of accuracy should be adequate for most applications. With this fitting polynomial, the sphere of influence for existing structures,  $r_G = (2GM_{\text{obj}}/\beta^*H_0^2)^{1/3}$ , can be written in the form

$$r_G \approx 0.7 \text{ Mpc} \left( \frac{M_{\text{obj}}}{10^{12} M_\odot} \right)^{1/3} h_{70}^{-2/3} [1 + a(1+w) + b(1+w)^2 + c(1+w)^3]^{-1/3}. \quad (\text{A.7})$$

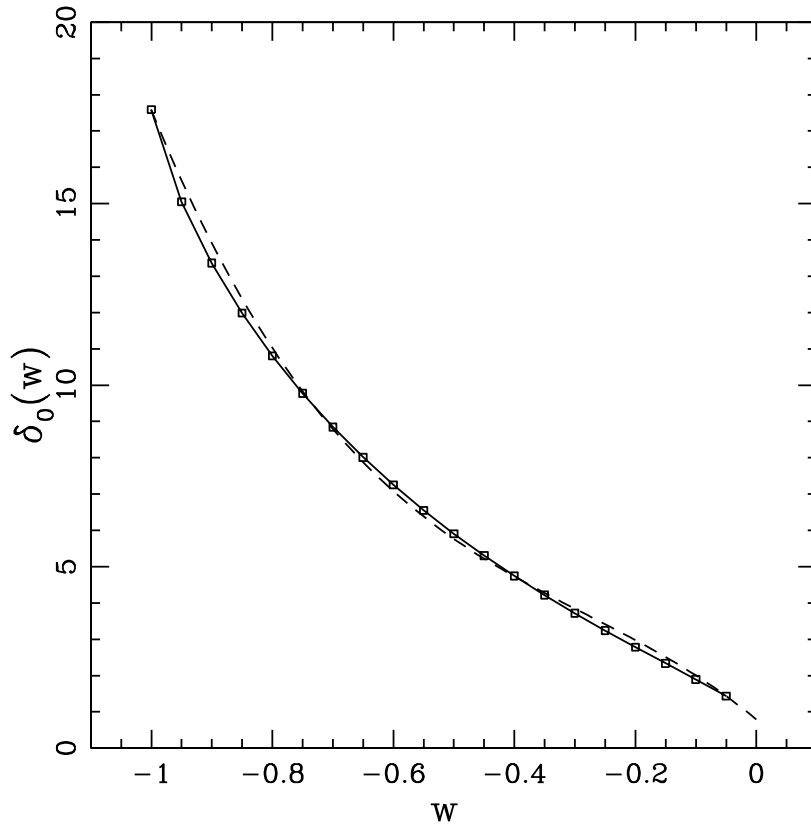


**Figure A.1.** This plot shows the overdensity required for the collapse of future structures as a function of the parameter  $w$  appearing in the equation of state for quintessence models. The sphere of gravitational influence for existing cosmological structures is given by  $r_G = (2GM_{\text{obj}}/\beta^*H_0^2)^{1/3}$ , where the parameter  $\beta^*$  is related to the overdensity required for collapse of existing regions via  $\beta^* = \delta_0\Omega_{\text{m},0}$  (see text). The solid curve shows the numerically determined values; the dashed curve shows a cubic fit to the function (using equations [A.5 – A.7]). As  $w$  becomes more negative, the overdensity required for collapse becomes larger and the sphere of gravitational influence (for existing structures) grows smaller — the formation of future structure is more suppressed for smaller  $w$ .

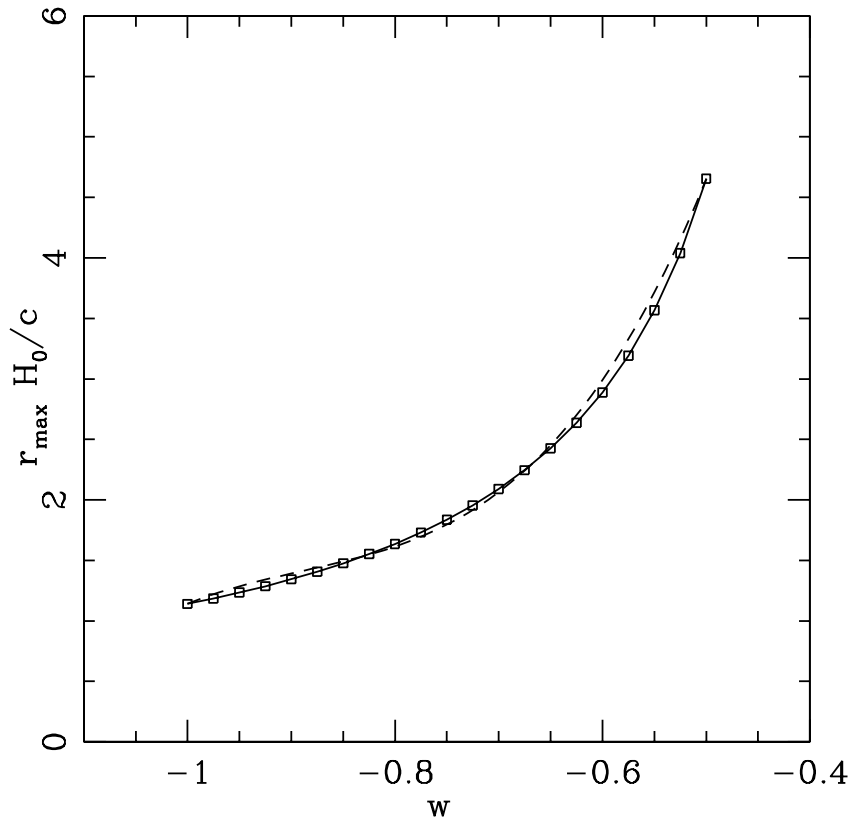


**Figure A.2.** The maximum distance that a light signal can propagate between the present epoch and temporal infinity for an accelerating universe described by equation of state parameter  $w$ . The dashed curve shows a cubic fit to the numerically obtained result (see Appendix A and equation [A.9]).

For accelerating universes, we can find the maximum distance that a light signal can propagate between now (the present epoch) and temporal infinity. This maximum distance  $r_{\max}$  is given by

$$r_{\max} \equiv \int_{t_0}^{\infty} \frac{cdt}{a(t)} = \frac{c}{H_0} \int_1^{\infty} \frac{da}{a^2} \left[ \Omega_{m,0} a^{-3} + \Omega_{v,0} a^{-p} \right]^{-1/2}. \quad (\text{A.8})$$

By solving the integral numerically and fitting the result, we can write the distance scale in the form

$$r_{\max} H_0 / c \equiv I(w) \approx I_0 \left[ 1 + \tilde{a}(1+w) + \tilde{b}(1+w)^2 + \tilde{c}(1+w)^3 \right], \quad (\text{A.9})$$

where  $I_0 = 1.141$ ,  $\tilde{a} = 3.073$ ,  $\tilde{b} = -12.39$ , and  $\tilde{c} = 37.13$ . This fitting function is valid for the range of equations of state  $-1 \leq w \leq -1/2$ . As  $w \rightarrow -1/3$ , the integral (and hence  $r_{\max}$ ) becomes divergent. The result is shown in Figure A.2.

With the sphere of gravitational influence defined by equation (A.7) and the maximum distance defined by equation (A.9), we can define the isolation time  $t_{\text{iso}}$  for structures through the relation  $a(t)r_G \geq r_{\max}$ . The asymptotic form for the scale factor  $a(t)$  is given by

$$a(t) \approx \left( \frac{p}{2} \sqrt{\Omega_{v,0}} H_0 t \right)^{2/p}, \quad (\text{A.10})$$

where  $p = 3(1+w)$  as before. The isolation time is then given by

$$t_{\text{iso}} \approx \frac{2H_0^{-1}}{p\sqrt{\Omega_{v,0}}} \left\{ I(w) [\beta^*(w)]^{1/3} c \left[ 2GM_{\text{obj}} H_0 \right]^{-1/3} \right\}^{p/2}. \quad (\text{A.11})$$

Notice that this form applies only for values of  $p$  strictly greater than zero ( $w > -1$ ). To properly take the limit  $w \rightarrow -1$ ,  $p \rightarrow 0$ , the function must include additional terms that are neglected in this approximation.

## APPENDIX B

### Dimensional Analysis

In this Appendix, we present a dimensional analysis that illustrates the fundamental results of this paper in simpler terms. With the benefit of hindsight, we can conceptually reproduce many of the results of this paper.

Because the universe is already dominated by its dark vacuum contribution, the future behavior of the universe is essentially one of exponential expansion at a well defined rate. This rate is set by the Hubble constant. For the sake of definiteness, we will use the asymptotic value of the Hubble constant  $H_\infty = H_0\sqrt{\Omega_{v,0}} \approx 59 \text{ km s}^{-1} \text{ Mpc}^{-1}$ . This rate also defines the basic time scale for the problem, i.e.,  $\tau = H_\infty^{-1} = 17 \text{ Gyr}$ .

Using square brackets to denote the units of a given quantity (in terms of length  $L$ , time  $T$ , and mass  $M$ ), we can list the variables that describe the asymptotic universe via

$$[H_\infty] = T^{-1} \quad [G] = L^3/MT^2 \quad [c] = L/T. \quad (\text{B.1})$$

These variables can be combined to produce a dimensionless field  $\Pi_0$  if only if a mass scale  $M_0$  is introduced. The field  $\Pi_0$  is then given by

$$\Pi_0 \equiv \frac{GM_0H_\infty}{c^3}. \quad (\text{B.2})$$

If no additional variables are introduced into the problem – no additional entities are introduced into the universe – then typically  $\Pi_0 \approx 1$ , which in turn defines a mass scale for the universe. Inserting numerical values, we find  $M_0 \sim 10^{23}M_\odot$  (essentially the same result as that of equation [4.23]).

Both our physical intuition and the results of our numerical simulations indicate that cosmic structure becomes frozen and bound astronomical objects – galaxies and clusters – grow isolated in the long term. The presence of a cluster or galaxy introduces another variable into the problem, namely the mass scale  $M_{\text{obj}}$ . This scale, in turn, defines another dimensionless field  $\Pi_1$  given by

$$\Pi_1 \equiv \frac{GM_{\text{obj}}H_\infty}{c^3} \sim 10^{-11}, \quad (\text{B.3})$$

an incredibly small number. This quantity represents the overdensity of an isolated cluster embedded in an island universe at late times.

Next, we want to define a length scale  $r_0$  associated with the galaxy or cluster itself. Such a length scale can be defined in several ways. The natural length scale of the universe is given by  $c/H_\infty = r_H$ . Since the ratio  $r_0/r_H$  is dimensionless, we expect that

$$r_0 = r_H \Pi_1^n = \frac{c}{H_\infty} \left( \frac{GM_{\text{obj}}H_\infty}{c^3} \right)^n, \quad (\text{B.4})$$

where the power-law index  $n$  is to be determined. If we argue that the length scale associated with the galaxy or cluster should be non-relativistic, then  $n$  must be chosen so that the scale  $r_0$  does not depend on the speed of light. This constraint specifies  $n = 1/3$  and hence

$$r_0 = (GM_{\text{obj}}/H_0^2)^{1/3}, \quad (\text{B.5})$$

which is the same as the gravitational sphere of influence defined by equation (4.11) (up to dimensionless factors of order unity). Equation (B.4) allows for a second “natural” length scale – that determined by eliminating the Hubble parameter by using  $n = 1$ . This choice results in the scale  $r = GM_{\text{obj}}/c^2$ , which is the length scale that determines the form of the functions  $A(r)$  and  $B(r)$  appearing in the metric (equation [4.24]).

Another result of this investigation is the time scales for which objects become isolated and radiation is stretched “beyond the horizon”. At this level of analysis, *all*

of these time scales are the same and are determined by the asymptotic e-folding time  $t = H_\infty^{-1} \approx 17$  Gyr. The more detailed mathematical analysis of the paper includes logarithmic correction factors, as listed in Table 1. For cosmological events, however, even the longest time scale is only 1260 Gyr or 74 e-folding times (it also turns out that  $\ln[r_H/\lambda] \sim 75$  – for ‘typical’ astrophysical photons of wavelength  $\lambda \sim 1\mu\text{m}$ ). For a universe with a cosmological constant, the basic result is that all future cosmological events must unfold with “nearly” the same time scale, given by  $H_\infty^{-1}$ . For comparison, stellar evolution time scales are determined by more complicated physics and span a wider range of time scales, both much shorter ( $\sim 10^5$  yr for star formation events; Adams & Fatuzzo, 1996) and much longer ( $\sim 10^{13} - 10^{14}$  yr for the duration of the longest-lived stars; AL97, LBA97). Galactic evolution – dynamical relaxation and evaporation – takes place over still longer times ( $\sim 10^{20}$  yr; Dyson, 1979; Binney & Tremaine, 1987, AL97).

## APPENDIX C

### Mass Function

The upturn in the FOF mass function (Figure 7.6) at small mass is a surprising and potentially troubling feature of our WDM simulations, and it is necessary to determine if this phenomenon is a result of the simulation or of the FOF group-finding algorithm. We have conducted a series of 5 WDM simulations with various volumes and mass resolutions to examine this effect, and present the resultant mass fractions at  $a = 1$  in Figure C.1. Here, we are plotting the mass fractions, as opposed to the mass functions shown in Figure 7.6. The mass fraction and mass function are related by  $dn(M)/d\ln(M) = (\bar{\rho}/M)f(M)$ . We used a mass resolution of  $3.97 \times 10^{10} h^{-1} M_{\odot}$  as our base model, conducting three runs at this scale with comoving box lengths of 200, 100, and  $50 h^{-1} \text{Mpc}$  (solid, dash-dot, and dash-dot-dot-dot lines), and two additional runs with box length  $50 h^{-1} \text{Mpc}$  with mass resolutions  $6.20 \times 10^8$  and  $4.96 \times 10^9 h^{-1} M_{\odot}$  (dotted and dashed lines). The left panel shows the mass fraction as a function of mass in units of  $h^{-1} M_{\odot}$ , while the right panel shows the same fractions in units of number of particles.

The most immediate feature of the left panel is that the location of the upturn changes with mass resolution, independent of the simulated volume. The right panel of Figure C.1 further indicates that this upturn is a purely numerical artifact. Here, the mass fraction is plotted in units of number of particles in the halo, and we see that at low masses all resolutions converge on the upturn. Finally, we also note that for the two runs that have corresponding CDM cosmologies (solid and dotted lines)

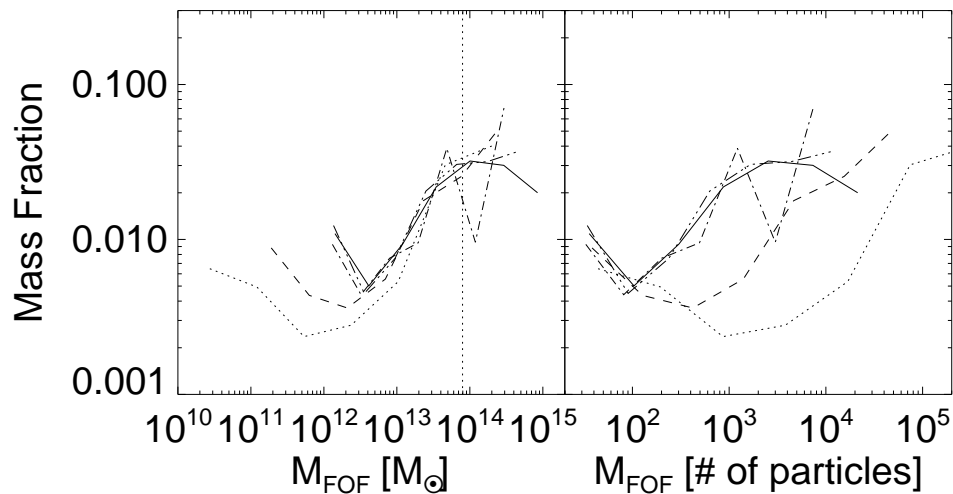


**Figure C.1.** *Left Panel:* The fraction of mass in a collapsed structure of a given mass as a function of mass for a number of WDM simulations with varying degrees of mass particle resolution ( $M_{particle} = 6.20 \times 10^8 - 3.97 \times 10^{10} h^{-1} M_{\odot}$ ) and simulated volume ( $50 - 200 h^{-1} \text{Mpc}$ ). The vertical dotted line represents the truncation scale,  $M_c$ . *Right Panel:* The same mass fractions, now plotted mass in units of number of particles.

the location of the minimum in the mass fraction ( $M_{min}$ ) corresponds to a transition point: halos with  $M > M_{min}$  have corresponding halos in the CDM simulation, while those with  $M < M_{min}$  do not (see Figure 7.7). In these, 90% of all halos with  $M_{FOF} \gg M_{min}$  have corresponding halos in the CDM cosmology, while less than 1% of halos with  $M_{FOF} < M_{min}$  have identified cross halos. Even though the input power spectrum for the CDM and WDM cosmologies is vastly different, it is not the value of  $M_c$ , but rather the value  $M_{min}$  that determines the mass where we are unable to find corresponding halos in the CDM cosmology. This trend is especially noteworthy in the case of the small volume realization, where  $M_{min}$  is almost two orders of magnitude below  $M_c$ . Wang & White (2007) argue that these low-mass halos form through numerical instability in the N-body simulation. While we do see many small halos that appear to have such an origin, we note that in Figure 7.6, the SO mass function exhibits a much weaker upturn than that FOF mass function. In fact, most of the FOF halos below the upturn have no central overdensity greater



than  $200\rho_{crit}$  and are not detected by our SO groupfinder. Instead of looking like a roughly spherical group, these FOF halos exist more as a linear string of particles that are not even identified as energetically bound by SUBFIND .

One expects an upturn eventually, since a FOF group finder puts every particle in a group of some size. At any given time, 50-70% of all particles end up in “groups” of one particle, requiring an upturn somewhere, something that you would expect even in a standard  $\Lambda$ CDMsimulation (although the effect there should be much smaller due to the large number of actual groups at this mass range). Our results suggest that this contamination is an issue for groups containing fewer than

$$N_{min} \approx 250 \left( \frac{M_{particle}}{10^{10}M_{\odot}h^{-1}} \right)^{-0.56} \quad (C.1)$$

particles when a linking length of 0.164 is used.

## APPENDIX D

### Stability of Halos

Because much of this work deals with the long-term fate of halos, care needs to be taken to insure that our halos are stable over very long periods of time. As discussed in section 3.1, numerical relaxation can become effective at removing particles from high density regions due to hard collisions and two-body encounters. Again, the relaxation time for a collisionless system is given by equation 3.3,

$$t_{relax} = t_{cross} \frac{N}{8 \ln(R/b_{min})}. \quad (D.1)$$

Here,  $t_{cross}$  and  $R$  are the crossing time and size of the system, while  $b_{min} = GM/v^2$  is the gravitational radius of the system. The relaxation time for the system,  $t_{relax}$  is directly proportional to the mass resolution of the simulation (which determines  $N$ ). While the relaxation times for most of our halos are on the order of  $10^4$ Gyr (and is, in fact, even longer because of the softened potential), the relaxation will proceed much more quickly in the inner regions, making it necessary to test simulations of various resolutions for long-term stability of the halo core. Even with the presence of the softening discussed in section 3.1, because of our long time-scale, if our resolution is too coarse, two-body collisions resulting from finite mass resolution will eject particles from halo centers, causing the systems to relax through an unphysical process.

We examine the effects of relaxation by measuring the radii of surfaces containing a fixed number of particles in relaxed halos, shown in Figure D.1. Each line represents the radius internal to which are a fixed number of particles, ranging from 100 to 409,600 as a function of time. Once the halo has reached dynamical equilibrium, we

expect the radius to be constant if relaxation is not having a significant effect. If there is an appreciable amount of relaxation present, however, we would expect these radii to increase as close encounters increase the energy of particles enough to move them onto larger orbits or to eject them all together.

At early times, Figure D.1 shows substantial evolution for all radii because the rapid mass accretion onto the halo. The outer radii decrease as mass is added into the system, while the inner radii increase due to virialization of the accreted material. By  $a \sim 3$ , however, mass accretion has ended and the radii stabilize substantially. The larger radii become extremely smooth while the lower radii exhibit small, rapid fluctuations due to stochastic processes. The important thing to consider, however, is the overall evolution of the radii smoothed over time. Clearly, surfaces containing  $\gtrsim 6400$  particles are stable throughout the time plotted, exhibiting no change  $r$  from  $a = 3 - 100$ . The inner surfaces, however, have a gradual, but persistent, increase that may be an indication of relaxation for radii enclosing  $\lesssim 1000$  particles. At these inner radii, a couple of percent of the particles are being pushed out every factor of 10 in  $a$ . While this is not catastrophic relaxation, we mitigate the effect by ignoring the inner regions,  $r \leq 0.1$ , of modestly resolved halos for most of the analysis. Whenever the inner regions of the halos are more important (as in measuring phase space distributions) we consider only the more highly resolved halos.

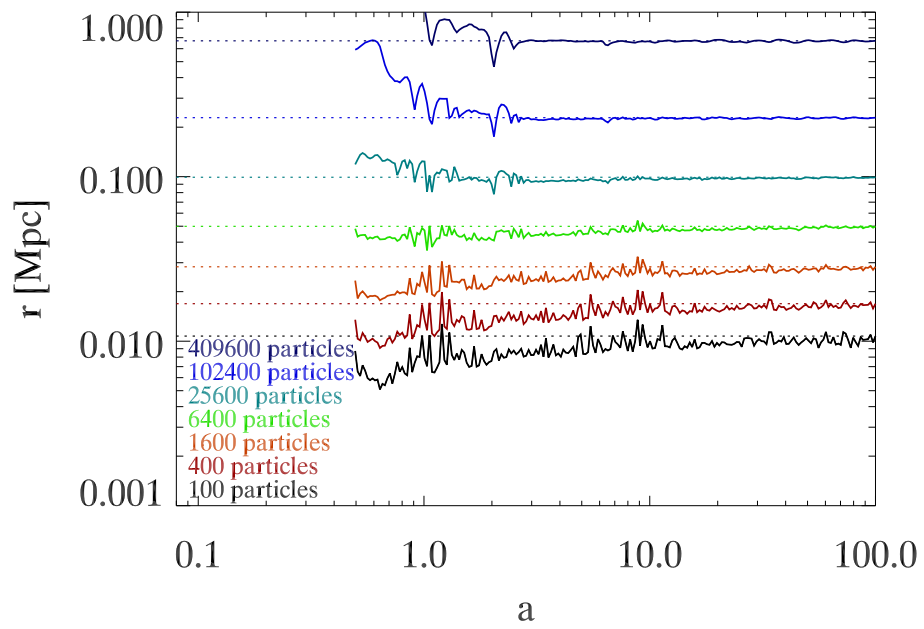


**Figure D.1.** The radii in a halo enclosing a given number of particles as a function of time. The different colors represent different numbers of enclosed particles. The dotted lines show the final ( $a = 100$ ) value for the radius.

## BIBLIOGRAPHY

## BIBLIOGRAPHY

- Aarseth, S. J., Turner, E. L., & Gott, III, J. R. 1979, *ApJ*, 228, 664
- Adams, F. C., Busha, M. T., Evrard, A. E., & Wechsler, R. H. 2003, *International Journal of Modern Physics D*, 12, 1743
- Adams, F. C., & Fatuzzo, M. 1996, *ApJ*, 464, 256
- Adams, F. C., & Laughlin, G. 1997, *Reviews of Modern Physics*, 69, 337
- Alpher, R. A., & Herman, R. C. 1948, *Nature*, 162, 774
- Alvarez, M. A., Shapiro, P. R., & Martel, H. 2003, in *Revista Mexicana de Astronomia y Astrofisica Conference Series*, Vol. 17, *Revista Mexicana de Astronomia y Astrofisica Conference Series*, ed. V. Avila-Reese, C. Firmani, C. S. Frenk, & C. Allen, 39–40
- Angulo, R., Baugh, C. M., Frenk, C. S., Bower, R. G., Jenkins, A., & Morris, S. L. 2005, *MNRAS*, 362, L25
- Ascasibar, Y., Yepes, G., Gottlöber, S., & Müller, V. 2004, *MNRAS*, 352, 1109
- Avila-Reese, V., Colín, P., Valenzuela, O., D’Onghia, E., & Firmani, C. 2001, *ApJ*, 559, 516
- Avila-Reese, V., Firmani, C., & Hernández, X. 1998, *ApJ*, 505, 37
- Bagla, J. S., & Ray, S. 2005, *MNRAS*, 358, 1076

- Balbi, A., Baccigalupi, C., Matarrese, S., Perrotta, F., & Vittorio, N. 2001, *ApJ*, 547, L89
- Bardeen, J. M. 1981, *Physical Review Letters*, 46, 382
- Bardeen, J. M., Bond, J. R., Kaiser, N., & Szalay, A. S. 1986, *ApJ*, 304, 15
- Berger, E., Chary, R., Cowie, L. L., Price, P. A., Schmidt, B. P., Fox, D. B., Cenko, S. B., Djorgovski, S. G., Soderberg, A. M., Kulkarni, S. R., McCarthy, P. J., Gladders, M. D., Peterson, B. A., & Barger, A. J. 2006, *ArXiv Astrophysics e-prints*
- Bertschinger, E. 1985, *ApJS*, 58, 39
- . 1998, *ARA&A*, 36, 599
- . 2006, *Phys. Rev. D*, 74, 063509
- Binney, J., & Tremaine, S. 1987, *Galactic Dynamics* (Princeton, New Jersey: Princeton University Press)
- Birrell, N. D., & Davies, P. C. W. 1982, *Quantum fields in curved space* (Cambridge: University Press, 1982)
- Blumenthal, G. R., Faber, S. M., Primack, J. R., & Rees, M. J. 1984, *Nature*, 311, 517
- Bode, P., Ostriker, J. P., & Turok, N. 2001, *ApJ*, 556, 93
- Bond, J. R., Kofman, L., & Pogosyan, D. 1996, *Nature*, 380, 603
- Bond, J. R., & Myers, S. T. 1996, *ApJS*, 103, 1
- Bond, J. R., & Szalay, A. S. 1983, *ApJ*, 274, 443

- Bullock, J. S., Kolatt, T. S., Sigad, Y., Somerville, R. S., Kravtsov, A. V., Klypin, A. A., Primack, J. R., & Dekel, A. 2001, *MNRAS*, 321, 559
- Busha, M. T., Adams, F. C., Wechsler, R. H., & Evrard, A. E. 2003, *ApJ*, 596, 713
- Busha, M. T., Evrard, A. E., & Adams, F. C. 2007, *ApJ*
- Busha, M. T., Evrard, A. E., Adams, F. C., & Wechsler, R. H. 2005, *MNRAS*, 363, L11
- Caldwell, R. R., Kamionkowski, M., & Weinberg, N. N. 2003, *Physical Review Letters*, 91, 071301
- Carroll, S. M. 2004, *Spacetime and geometry. An introduction to general relativity* (Spacetime and geometry / Sean Carroll. San Francisco, CA, USA: Addison Wesley, ISBN 0-8053-8732-3, 2004, XIV + 513 pp.)
- Carroll, S. M., Press, W. H., & Turner, E. L. 1992, *ARA&A*, 30, 499
- Chiueh, T., & He, X.-G. 2002, *Phys. Rev. D*, 65, 123518
- Cirkovic, M. M. 2003, *American Journal of Physics*, 71, 122
- Ćirković, M. M., & Samurović, S. 2001, *A&A*, 373, 377
- Clowe, D., Bradač, M., Gonzalez, A. H., Markevitch, M., Randall, S. W., Jones, C., & Zaritsky, D. 2006, *ApJ*, 648, L109
- Colín, P., Avila-Reese, V., & Valenzuela, O. 2000, *ApJ*, 542, 622
- Cooray, A., & Sheth, R. 2002, *Phys. Rep.*, 372, 1
- Copi, C. J., Schramm, D. N., & Turner, M. S. 1994, *Science*, 267, 192
- David, L. P., Nulsen, P. E. J., McNamara, B. R., Forman, W., Jones, C., Ponman, T., Robertson, B., & Wise, M. 2001, *ApJ*, 557, 546



- Davis, M., Efstathiou, G., Frenk, C. S., & White, S. D. M. 1985, *ApJ*, 292, 371
- de Bernardis, P., Ade, P. A. R., Bock, J. J., Bond, J. R., Borrill, J., Boscaleri, A., Coble, K., Crill, B. P., De Gasperis, G., Farese, P. C., Ferreira, P. G., Ganga, K., Giacometti, M., Hivon, E., Hristov, V. V., Iacoangeli, A., Jaffe, A. H., Lange, A. E., Martinis, L., Masi, S., Mason, P. V., Mauskopf, P. D., Melchiorri, A., Migliorini, L., Montroy, T., Netterfield, C. B., Pascale, E., Piacentini, F., Pogosyan, D., Prunet, S., Rao, S., Romeo, G., Ruhl, J. E., Scaramuzzi, F., Sforza, D., & Vittorio, N. 2000, *Nature*, 404, 955
- de Blok, W. J. G., McGaugh, S. S., & Rubin, V. C. 2001, *AJ*, 122, 2396
- Dehnen, W., & McLaughlin, D. E. 2005, *MNRAS*, 363, 1057
- Diemand, J., Kuhlen, M., & Madau, P. 2007, *ApJ*, 657, 262
- Diemand, J., Moore, B., & Stadel, J. 2005, *Nature*, 433, 389
- Doroshkevich, A. G., Kotok, E. V., Poliudov, A. N., Shandarin, S. F., Sigov, I. S., & Novikov, I. D. 1980, *MNRAS*, 192, 321
- Doroshkevich, A. G., & Zeldovich, I. B. 1975, *Ap&SS*, 35, 55
- Duncan, M. J., Levison, H. F., & Lee, M. H. 1998, *AJ*, 116, 2067
- Dünner, R., Reisenegger, A., Meza, A., Araya, P. A., & Quintana, H. 2007, *MNRAS*, 376, 1577
- Dyson, F. J. 1979, *Reviews of Modern Physics*, 51, 447
- Eke, V. R., Cole, S., & Frenk, C. S. 1996, *MNRAS*, 282, 263
- Eke, V. R., Navarro, J. F., & Steinmetz, M. 2001, *ApJ*, 554, 114
- Ellis, G. F. R., & Rothman, T. 1993, *American Journal of Physics*, 61, 883

- Evrard, A. E., & Crone, M. M. 1992, *ApJ*, 394, L1
- Evrard, A. E., & Gioia, I. M. 2002, *Clusters, Cosmology and Mergers (ASSL Vol. 272: Merging Processes in Galaxy Clusters)*, 253–304
- Evrard, A. E., MacFarland, T. J., Couchman, H. M. P., Colberg, J. M., Yoshida, N., White, S. D. M., Jenkins, A., Frenk, C. S., Pearce, F. R., Peacock, J. A., & Thomas, P. A. 2002, *ApJ*, 573, 7
- Evrard, A. E., Metzler, C. A., & Navarro, J. F. 1996, *ApJ*, 469, 494
- Fillmore, J. A., & Goldreich, P. 1984, *ApJ*, 281, 1
- Freedman, W. L., Madore, B. F., Gibson, B. K., Ferrarese, L., Kelson, D. D., Sakai, S., Mould, J. R., Kennicutt, Jr., R. C., Ford, H. C., Graham, J. A., Huchra, J. P., Hughes, S. M. G., Illingworth, G. D., Macri, L. M., & Stetson, P. B. 2001, *ApJ*, 553, 47
- Fukushige, T., & Makino, J. 2001, *ApJ*, 557, 533
- Fulling, S. A. 1977, *J. Phys. A: Math, Gen*, 10, 917
- Gamow, G. 1948, *Nature*, 162, 680
- Gao, L., White, S. D. M., Jenkins, A., Frenk, C. S., & Springel, V. 2005, *MNRAS*, 363, 379
- Garnavich, P. M., Jha, S., Challis, P., Clocchiatti, A., Diercks, A., Filippenko, A. V., Gilliland, R. L., Hogan, C. J., Kirshner, R. P., Leibundgut, B., Phillips, M. M., Reiss, D., Riess, A. G., Schmidt, B. P., Schommer, R. A., Smith, R. C., Spyromilio, J., Stubbs, C., Suntzeff, N. B., Tonry, J., & Carroll, S. M. 1998, *ApJ*, 509, 74
- Gentile, G., Salucci, P., Klein, U., Vergani, D., & Kalberla, P. 2004, *MNRAS*, 351, 903

- Gibbons, G. W., & Hawking, S. W. 1977, *Phys. Rev. D*, 15, 2738
- Gott, J. R. I. 1996, in *Astronomical Society of the Pacific Conference Series*, Vol. 88, Clusters, Lensing, and the Future of the Universe, ed. V. Trimble & A. Reisenegger, 107–+
- Götz, M., & Sommer-Larsen, J. 2003, *Ap&SS*, 284, 341
- Gudmundsson, E. H., & Björnsson, G. 2002, *ApJ*, 565, 1
- Gunn, J. E., & Gott, J. R. I. 1972, *ApJ*, 176, 1
- Guth, A. H. 1981, *Phys. Rev. D*, 23, 347
- Hansen, S. H., & Stadel, J. 2006, *Journal of Cosmology and Astro-Particle Physics*, 5, 14
- Hayashi, E., & Navarro, J. F. 2006, *MNRAS*, 373, 1117
- Hernquist, L. 1990, *ApJ*, 356, 359
- Hockney, R. W., & Eastwood, J. W. 1981, *Computer Simulation Using Particles* (Computer Simulation Using Particles, New York: McGraw-Hill, 1981)
- Hoffman, Y., Lahav, O., Yepes, G., & Dover, Y. 2007, *ArXiv e-prints*, 705
- Holmberg, E. 1941, *ApJ*, 94, 385
- Hu, W., & Sugiyama, N. 1996, *ApJ*, 471, 542
- Hubble, E. 1929, *Proceedings of the National Academy of Science*, 15, 168
- Huss, A., Jain, B., & Steinmetz, M. 1999, *ApJ*, 517, 64
- Islam, J. N. 1977, *QJRAS*, 18, 3
- Jackson, J. D. 1999, *Classical Electrodynamics*

- Jacoby, G. H., Branch, D., Ciardullo, R., Davies, R. L., Harris, W. E., Pierce, M. J., Pritchett, C. J., Tonry, J. L., & Welch, D. L. 1992, *PASP*, 104, 599
- Jenkins, A., Frenk, C. S., Pearce, F. R., Thomas, P. A., Colberg, J. M., White, S. D. M., Couchman, H. M. P., Peacock, J. A., Efstathiou, G., & Nelson, A. H. 1998, *ApJ*, 499, 20
- Jenkins, A., Frenk, C. S., White, S. D. M., Colberg, J. M., Cole, S., Evrard, A. E., Couchman, H. M. P., & Yoshida, N. 2001, *MNRAS*, 321, 372
- Jing, Y. P., & Suto, Y. 2002, *ApJ*, 574, 538
- Katz, N., Quinn, T., & Gelb, J. M. 1993, *MNRAS*, 265, 689
- Klypin, A., Kravtsov, A. V., Valenzuela, O., & Prada, F. 1999, *ApJ*, 522, 82
- Knebe, A., Devriendt, J. E. G., Gibson, B. K., & Silk, J. 2003, *MNRAS*, 345, 1285
- Knebe, A., Devriendt, J. E. G., Mahmood, A., & Silk, J. 2002, *MNRAS*, 329, 813
- Kolb, E. W., & Turner, M. S. 1990, *The early universe* (Frontiers in Physics, Reading, MA: Addison-Wesley, 1988, 1990)
- Krauss, L. M., & Scherrer, R. J. 2007, *ArXiv e-prints*, 704
- Krauss, L. M., & Starkman, G. D. 2000, *ApJ*, 531, 22
- Kravtsov, A. V., Berlind, A. A., Wechsler, R. H., Klypin, A. A., Gottlöber, S., Allgood, B., & Primack, J. R. 2004, *ApJ*, 609, 35
- Laughlin, G., Bodenheimer, P., & Adams, F. C. 1997, *ApJ*, 482, 420
- Loeb, A. 2002, *Phys. Rev. D*, 65, 047301
- Lokas, E. L., & Hoffman, Y. 2001, *ArXiv Astrophysics e-prints*

- Lynden-Bell, D. 1967, MNRAS, 136, 101
- Ma, C.-P., & Boylan-Kolchin, M. 2004, Physical Review Letters, 93, 021301
- Mallett, R. L. 1985, Phys. Rev. D, 31, 416
- Mather, J. C., Cheng, E. S., Eplee, Jr., R. E., Isaacman, R. B., Meyer, S. S., Shafer, R. A., Weiss, R., Wright, E. L., Bennett, C. L., Boggess, N. W., Dwek, E., Gulkis, S., Hauser, M. G., Janssen, M., Kelsall, T., Lubin, P. M., Moseley, Jr., S. H., Murdock, T. L., Silverberg, R. F., Smoot, G. F., & Wilkinson, D. T. 1990, ApJ, 354, L37
- Misner, C. W., Thorne, K. S., & Wheeler, J. A. 1973, Gravitation (San Francisco: W.H. Freeman and Co., 1973)
- Monaghan, J. J., & Lattanzio, J. C. 1985, A&A, 149, 135
- Moore, B., Ghigna, S., Governato, F., Lake, G., Quinn, T., Stadel, J., & Tozzi, P. 1999a, ApJ, 524, L19
- Moore, B., Quinn, T., Governato, F., Stadel, J., & Lake, G. 1999b, MNRAS, 310, 1147
- Mullis, C. R., Rosati, P., Lamer, G., Böhringer, H., Schwobe, A., Schuecker, P., & Fassbender, R. 2005, ApJ, 623, L85
- Nagamine, K., & Loeb, A. 2003, New Astronomy, 8, 439
- Navarro, J. F., Frenk, C. S., & White, S. D. M. 1996a, ApJ, 462, 563
- . 1996b, ApJ, 462, 563
- Navarro, J. F., Hayashi, E., Power, C., Jenkins, A. R., Frenk, C. S., White, S. D. M., Springel, V., Stadel, J., & Quinn, T. R. 2004, MNRAS, 349, 1039

- Okumura, S. K., Makino, J., Ebisuzaki, T., Fukushige, T., Ito, T., Sugimoto, D., Hashimoto, E., Tomida, K., & Miyakawa, N. 1993, PASJ, 45, 329
- Olive, K. A., & Skillman, E. D. 2004, ApJ, 617, 29
- O'Meara, J. M., Tytler, D., Kirkman, D., Suzuki, N., Prochaska, J. X., Lubin, D., & Wolfe, A. M. 2001, ApJ, 552, 718
- Peebles, P. J. E. 1970, AJ, 75, 13
- . 1980, The large-scale structure of the universe (Research supported by the National Science Foundation. Princeton, N.J., Princeton University Press, 1980. 435 p.)
- Pen, U.-L. 1997, ApJ, 490, L127+
- Penzias, A. A., & Wilson, R. W. 1965, ApJ, 142, 419
- Perlmutter, S., Aldering, G., Goldhaber, G., Knop, R. A., Nugent, P., Castro, P. G., Deustua, S., Fabbro, S., Goobar, A., Groom, D. E., Hook, I. M., Kim, A. G., Kim, M. Y., Lee, J. C., Nunes, N. J., Pain, R., Pennypacker, C. R., Quimby, R., Lidman, C., Ellis, R. S., Irwin, M., McMahon, R. G., Ruiz-Lapuente, P., Walton, N., Schaefer, B., Boyle, B. J., Filippenko, A. V., Matheson, T., Fruchter, A. S., Panagia, N., Newberg, H. J. M., Couch, W. J., & The Supernova Cosmology Project. 1999, ApJ, 517, 565
- Power, C., Navarro, J. F., Jenkins, A., Frenk, C. S., White, S. D. M., Springel, V., Stadel, J., & Quinn, T. 2003, MNRAS, 338, 14
- Press, W. H., & Schechter, P. 1974, ApJ, 187, 425
- Quinn, T., Katz, N., Stadel, J., & Lake, G. 1997, ArXiv Astrophysics e-prints
- Rasia, E., Tormen, G., & Moscardini, L. 2004, MNRAS, 351, 237

- Riess, A. G., Strolger, L.-G., Tonry, J., Casertano, S., Ferguson, H. C., Mobasher, B., Challis, P., Filippenko, A. V., Jha, S., Li, W., Chornock, R., Kirshner, R. P., Leibundgut, B., Dickinson, M., Livio, M., Giavalisco, M., Steidel, C. C., Benítez, T., & Tsvetanov, Z. 2004, *ApJ*, 607, 665
- Rubin, V. C., Burstein, D., Ford, Jr., W. K., & Thonnard, N. 1985, *ApJ*, 289, 81
- Saha, P., & Tremaine, S. 1992, *AJ*, 104, 1633
- Salucci, P., & Burkert, A. 2000, *ApJ*, 537, L9
- Seljak, U., Makarov, A., McDonald, P., & Trac, H. 2006, *Physical Review Letters*, 97, 191303
- Seljak, U., & Zaldarriaga, M. 1996, *ApJ*, 469, 437
- Shaviv, N. J., & Dekel, A. 2003, *ArXiv Astrophysics e-prints*
- Sheth, R. K., Mo, H. J., & Tormen, G. 2001, *MNRAS*, 323, 1
- Sheth, R. K., & Tormen, G. 1999, *MNRAS*, 308, 119
- Sirko, E. 2005, *ApJ*, 634, 728
- Sommer-Larsen, J., & Dolgov, A. 2001, *ApJ*, 551, 608
- Spergel, D. N., Bean, R., Doré, O., Nolta, M. R., Bennett, C. L., Dunkley, J., Hinshaw, G., Jarosik, N., Komatsu, E., Page, L., Peiris, H. V., Verde, L., Halpern, M., Hill, R. S., Kogut, A., Limon, M., Meyer, S. S., Odegard, N., Tucker, G. S., Weiland, J. L., Wollack, E., & Wright, E. L. 2006, *ArXiv Astrophysics e-prints*
- Spergel, D. N., Verde, L., Peiris, H. V., Komatsu, E., Nolta, M. R., Bennett, C. L., Halpern, M., Hinshaw, G., Jarosik, N., Kogut, A., Limon, M., Meyer, S. S., Page, L., Tucker, G. S., Weiland, J. L., Wollack, E., & Wright, E. L. 2003, *ApJS*, 148, 175

- Springel, V. 2005, MNRAS, 364, 1105
- Springel, V., White, S. D. M., Jenkins, A., Frenk, C. S., Yoshida, N., Gao, L., Navarro, J., Thacker, R., Croton, D., Helly, J., Peacock, J. A., Cole, S., Thomas, P., Couchman, H., Evrard, A., Colberg, J., & Pearce, F. 2005, Nature, 435, 629
- Springel, V., White, S. D. M., Tormen, G., & Kauffmann, G. 2001a, MNRAS, 328, 726
- Springel, V., Yoshida, N., & White, S. D. M. 2001b, New Astronomy, 6, 79
- Taylor, J. E., & Navarro, J. F. 2001, ApJ, 563, 483
- Tegmark, M., Strauss, M. A., Blanton, M. R., Abazajian, K., Dodelson, S., Sandvik, H., Wang, X., Weinberg, D. H., Zehavi, I., Bahcall, N. A., Hoyle, F., Schlegel, D., Scoccimarro, R., Vogeley, M. S., Berlind, A., Budavari, T., Connolly, A., Eisenstein, D. J., Finkbeiner, D., Frieman, J. A., Gunn, J. E., Hui, L., Jain, B., Johnston, D., Kent, S., Lin, H., Nakajima, R., Nichol, R. C., Ostriker, J. P., Pope, A., Scranton, R., Seljak, U., Sheth, R. K., Stebbins, A., Szalay, A. S., Szapudi, I., Xu, Y., Annis, J., Brinkmann, J., Burles, S., Castander, F. J., Csabai, I., Loveday, J., Doi, M., Fukugita, M., Gillespie, B., Hennessy, G., Hogg, D. W., Ivezić, Ž., Knapp, G. R., Lamb, D. Q., Lee, B. C., Lupton, R. H., McKay, T. A., Kunszt, P., Munn, J. A., O'Connell, L., Peoples, J., Pier, J. R., Richmond, M., Rockosi, C., Schneider, D. P., Stoughton, C., Tucker, D. L., vanden Berk, D. E., Yanny, B., & York, D. G. 2004, Phys. Rev. D, 69, 103501
- Thompson, L. A., & Gregory, S. A. 1978, ApJ, 220, 809
- van den Bergh, S. 1999, A&A Rev., 9, 273
- van den Bosch, F. C., Yang, X., Mo, H. J., & Norberg, P. 2005, MNRAS, 356, 1233
- Van Waerbeke, L., Mellier, Y., & Hoekstra, H. 2005, A&A, 429, 75



- Wagoner, R. V., Fowler, W. A., & Hoyle, F. 1967, *ApJ*, 148, 3
- Wang, J., & White, S. D. M. 2007, *ArXiv Astrophysics e-prints*
- Wang, L., Caldwell, R. R., Ostriker, J. P., & Steinhardt, P. J. 2000, *ApJ*, 530, 17
- Wechsler, R. H., Bullock, J. S., Primack, J. R., Kravtsov, A. V., & Dekel, A. 2002, *ApJ*, 568, 52
- White, M. 2001, *A&A*, 367, 27
- White, M., & Croft, R. A. C. 2000, *ApJ*, 539, 497
- White, S. D. M., Frenk, C. S., & Davis, M. 1983, *ApJ*, 274, L1
- Zel'Dovich, Y. B. 1970, *A&A*, 5, 84
- Zwicky, F. 1937, *ApJ*, 86, 217